ABSTRACT

Title of Dissertation: MANUFACTURING TECHNIQUES FOR TITANIUM ALUMINIDE BASED ALLOYS AND METAL MATRIX COMPOSITES

Kunal Kothari, Doctor of Philosophy, 2010

Directed By: Professor Norman M. Wereley
Department of Aerospace Engineering

Dual phase titanium aluminides composed vastly of gamma phase (TiAl) with moderate amount of alpha2 phase (Ti_3Al) have been considered for several high temperature aerospace and automobile applications. High specific strength coupled with good high temperature performance in the areas of creep and oxidation resistance makes titanium aluminides "materials of choice" for next generation propulsion systems. Titanium alumnides are primarily being considered as potential replacements for Ni-based superalloys in gas turbine engine components with aim of developing more efficient and leaner engines exhibiting high thrust-to-weight ratio.

Thermo-mechanical treatments have shown to enhance the mechanical performance of titanium aluminides. Additionally, small additions of interstitial elements have shown further and significant improvement in the mechanical performance of titanium alumnide alloys. However, titanium aluminides lack considerably in room temperature ductility and as a result manufacturing processes of

these aluminides have greatly suffered. Traditional ingot metallurgy and investment casting based methods to produce titanium aluminide parts in addition to being expensive, have also been unsuccessful in producing titanium aluminides with the desired mechanical properties. Hence, the manufacturing costs associated with these methods have completely outweighed the benefits offered by titanium aluminides.

Over the last two decades, several powder metallurgy based manufacturing techniques have been studied to produce titanium aluminide parts. These techniques have been successful in producing titanium aluminide parts with a homogeneous and refined microstructure. These powder metallurgy techniques also hold the potential of significant cost reduction depending on the wide market acceptance of titanium aluminides.

In the present study, a powder metallurgy based rapid consolidation technique has been used to produce near-net shape parts of titanium aluminides. Micron-sized titanium aluminide powders were rapidly consolidated to form near-net shape titanium aluminide parts in form of small discs and tiles. The rapidly consolidated titanium aluminide parts were found to be fully dense. The microstructure morphology was found to vary with consolidation conditions. The mechanical properties were found to be significantly dependent on microstructure morphology and grain size. Due to rapid consolidation, grain growth during consolidation was limited, which in turn led to enhanced mechanical properties. The high temperature mechanical properties for the consolidated titanium aluminide samples were characterized and were found to retain good mechanical performance up to 700^{o}C.

Micron-sized titanium aluminide powders with slightly less Aluminum and small Nb, and Cr additions were rapidly consolidated into near-net shape parts. The consolidated parts were found to exhibit enhanced mechanical performance in terms of ductility and yield strength. The negative effect of Oxygen on the flexural strength at high temperatures was found to be reduced with the addition of Nb.

In an effort to further reduce the grain size of the consolidated titanium aluminide samples, the as-received titanium aluminide powders were milled in an attrition mill. The average powder particle size of the powders was reduced by 60% after milling. The milled powders were then rapidly consolidated. The grain size of the consolidated parts was found to be in the sub-micrometer range. The mechanical properties were found to be significantly enhanced due to reduction of grain size in the sub-micrometer range.

In order to develop a metal matrix composite based on titanium aluminide matrix reinforced with titanium boride, an experiment to study the effect of rapid consolidation on titanium diboride powders was conducted. Micron-sized titanium diboride powders were consolidated and were found to be 93% dense and exhibited minimal grain growth. The low density of the consolidated part was attributed to low consolidation temperature.

Titanium aluminide and titanium diboride powders were blended together in an attrition mill and rapidly consolidated. A metal matrix composite with titanium aluminide matrix reinforced with titanium monoboride plates was formed. The titanium diboride in the powder form was found to be transformed to titanium monoboroide plates during consolidation due to the thermodynamic equilibrium

between titanium and titanium monoboride. The metal matrix composite was found to be 90% dense. The low density was due to particle size mismatch between the matrix and reinforcement powders and low consolidation temperature. An increase in the volume of titanium monoboride plates in the metal matrix composite was accompanied by an increase in the elastic modulus of the metal matrix composite.

MANUFACTURING TECHNIQUES FOR TITANIUM ALUMINIDE BASED ALLOYS AND METAL MATRIX COMPOSITES.

By

Kunal B. Kothari

Dissertation submitted to the Faculty of the Graduate School of the
University of Maryland, College Park, in partial fulfillment
of the requirements for the degree of
Doctor of Philosophy
2010

Advisory Committee:
Professor Norman M. Wereley, Chair
Dr. Ramachandran Radhakrishnan, (Adjunct Faculty)
Professor Darryll Pines
Professor Alison Flatau
Professor Sung Lee
Professor Lourdes Salamanca-Riba

Dedication

for my wife Anupama

Acknowledgements

I would like to acknowledge the support of Space Vehicle Technology Institute under grant NCC3-989 jointly funded by NASA and DOD within the NASA Constellation University Institutes Project for funding a good portion of my dissertation work.

I would also like to thank all the graduate students from the composites research lab for their valuable inputs in setting-up my experiments. The support from machinists in physics shop and Mike Perna was phenomeonal. I would have never gotten any samples machined without their help. The constant support by Microscopy and Microanalysis center, especially that of Tim Zhang in sample microanalysis was amazing.

I would like to thank my advisors Dr. Wereley and Dr. Radhakrishnan. Dr. Wereley for providing all the resources available to conduct this research and his constant support and patience throughout this period. Dr. Radhakrishnan for his invaluable technical inputs on my research plan, research papers and finally my dissertation.

Finally, this dissertation would have been impossible without the support of my wife. Her guidance and motivation is what finally made me see the light at the end of the tunnel. And of course my daughter for being there all the time.

Table of Contents

List of Figures

List of Tables

Chapter 1: Introduction

1.1 Titanium Aluminides: An Overview

Titanium Aluminides have attracted significant attention in the last twenty years for their attractive properties conducive for high temperature automobile and aerospace applications [1; 2; 3; 4; 5; 6]. One of the foremost applications that titanium aluminides have been considered for is its use in high performance gas turbine engines [7]. Due to its low density and high strength, titanium aluminides have become front-runners in replacing Nickel-based superalloys in gas turbine engines. Replacement of Ni-based superalloys parts with titanium aluminides is expected to reduce the structural weight of high performance gas turbine engines by 20% to 30% [8]. Hence, a significant increase in engine performance is expected with use of titanium aluminides in gas turbine engines. Titanium aluminides fall in the class of materials known as intermetallics.

1.1.1 What are Intermetallics?

Intermetallics are compounds formed between two metals. Their crystal structure and properties are completely different from their parent metals [9]. Usually after the formation of an intermetallic alloy, a long range ordering is developed in the material. This long range ordering places restriction on the deformation modes. These restrictions usually are manifested as increased strength, at least at elevated temperatures, reduced

ductility and fracture toughness [10]. Apart from titanium aluminides, examples of other intermetallics include NiAl, and FeAl.

1.1.2 Importance of Titanium Aluminides

Titanium aluminides display attractive properties such as low density, high strength, high stiffness and good corrosion, creep, and oxidation resistance. As discussed earlier, due to the long order nature of intermetallics, titanium aluminides lack room temperature ductility and fracture toughness. Fatigue crack growth rates are also an area of concern [11; 12]. For a long time, the attractive properties of titanium aluminides were outweighed by their difficulty in processing and machining at room temperature. But advances in manufacturing technologies, deeper understanding of titanium aluminides' microstructure, deformation mechanisms, and advances in micro-alloying has led to the first commercial use of titanium aluminides in high performace turbocharges for Formula One and sports cars [13]. Exhaust valves made of titanium aluminides have been used to replace the existing Ti-6242, Ti-1100, and IMI 834 alloys. Turbocharger wheels made out of titanium aluminides have been prototyped and tested to replace Ni-based superalloys. Till date, there are about thousand titanium aluminide turbocharger wheels and exhaust valves in service [14].

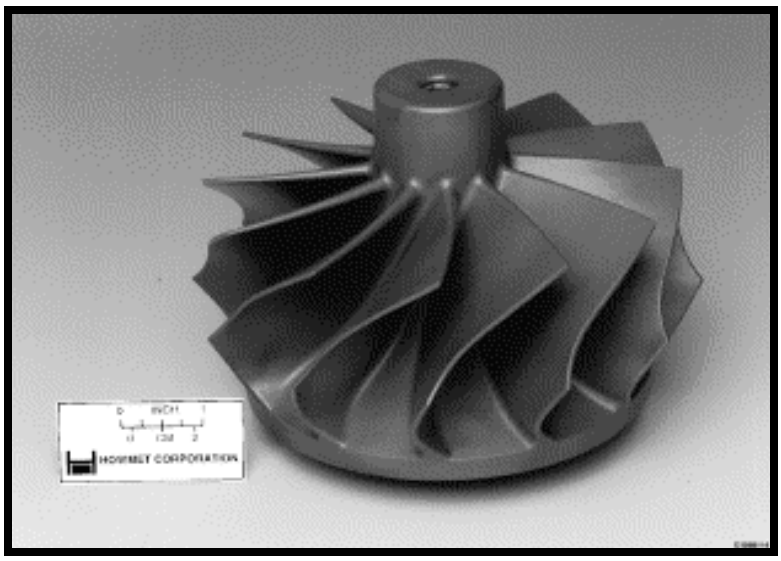

Figure 1: TiAl turbocharger wheels made by Howmet Corporation [15]

Gamma titanium aluminides have also been slated for use in General Electric's GEnex gas turbine engine designed for Boeing's 787 Dreamliner [16]. Titanium aluminides are being used in the low pressure turbine (LPT) blades. In addition, titanium aluminides were also investigated for use in High Speed Civil Transport (HSCT) [7].

The HSCT aircrafts was being designed to fly at Mach 2.4, while they take-off and land at conventional airports and meet EPA's environmental goals of reduced exhaust and noise pollutions [17]. To meet these stringent requirements, a titanium aluminide based divergent flap was proposed for noise attenuation and exhaust reduction.

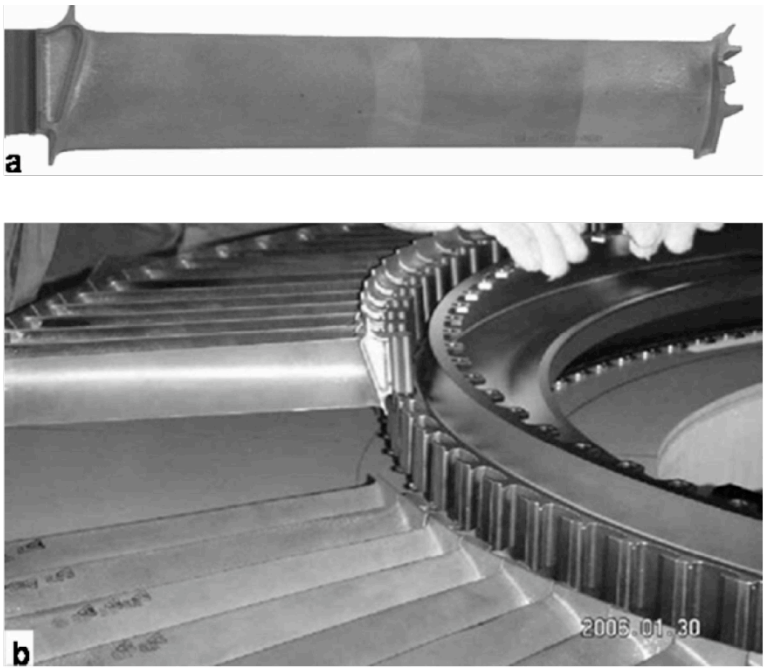

Figure 2: Photos of LPT hardware scheduled for production, Ti-48%Al-2%Cr-2%Nb (at%): (a) LPT blade casting (b) Portion of disk and some blades ready for assembly [10]

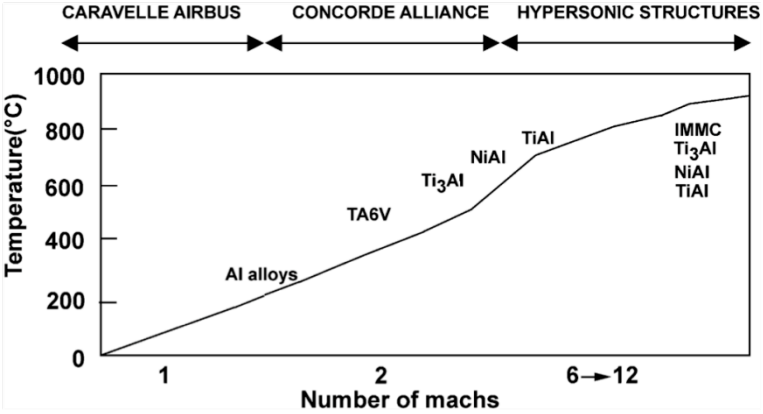

Figure 3: Structural materials developed with temperature and speed for aircraft as a function of the expected performances [3]

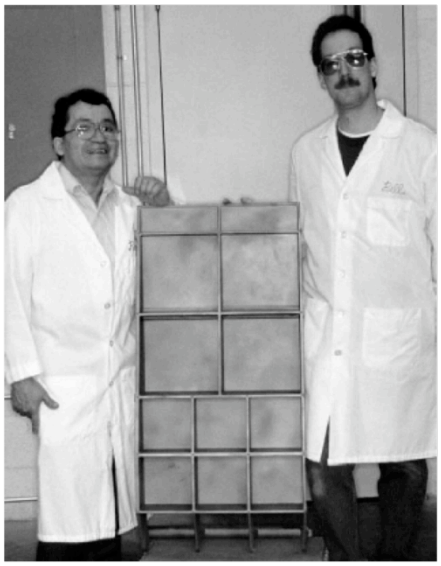

Figure 4: Proposed divergent flap prototype fabricated from cast TiAl (Ti-48Al-2Cr-2Nb) [7]

1.1.3 Challenges with Titanium Aluminides

Titanium Aluminides have found limited, but very challenging commercial applications in the automobile and aerospace industry. A broader requirement for titanium aluminides is to match Ni-based superalloys in performace as well as cost. The density of titanium aluminides is half that of superalloys, and hence replacement of Ni-based superalloys with titanium aluminides is expected to produce more leaner and efficient structural systems. Till date, titanium aluminides lag behind Ni-based superalloys in mechanical performance and significantly in production costs. This is mainly due to its low room temperature ductility and as a result its development is further dented by a lack of engineering design practices for low ductility materials. Even then, there have been significant advances made by the NASA Glenn Research Center, Plansee (Austria), and

GKSS Research Center (Germany) in developing titanium aluminide sheet manufacturing techniques. As a result, the cost of titanium aluminide sheets is expected to come as low as $150/lb depending on its wide acceptance in several commercial applications [18]. Table 1 is a list of potential applications for titanium aluminides in the aerospace industry.

Table 1: Potential applications for titanium aluminides [18]

Vehicle	Component	Number of Vehicles	Projected Usage
Global first strike/ Tomahawk missiles	Hot structures, compressor, nozzle	2,000+	30,000 lbs +
Comanche helicopter	Nozzles, IR suppression system	500+	10,000 lbs +
F-22, JSF	Nozzles, exhaust structures, engine components	700+	100,000 lbs +
Military Space Plane	Thermal Protection System (TPS), wingbox and vertical tail hot structures	2+	5,000 lbs +
Re-usable Launch Vehicles (RLVs)	TPS, wingbox and vertical tail hot structures	2-8	20,000 lbs - 80,000 lbs

1.1.4 Titanium Aluminides v. Superalloys

As mentioned earlier, the density of titanium aluminides is half of Ni-based superalloys. Titanium aluminides also display good high temperature oxidation and creep resistance, as well as excellent high temperature strength and modulus retention. But, titanium

aluminides lack in RT ductility and fracture toughness. Table II compares the mechanical properties of titanium aluminides with Ni-based superalloys at RT and high temperatures.

Table 2: Comparison of titanium aluminides to superalloys [19; 20]

Property	**TiAl-Base Alloys**	**Superalloys**
Density (gm/cm^3)	3.7 - 3.9	8.3
RT Modulus (GPa)	160-176	206
Yield Strength (MPa)	400 – 630	1000
Tensile Strength (MPa)	450 – 700	1200
Ductility at RT (%)	1 – 3	15
Creep Limit (^oC)	1000	1090
Oxidation (^oC)	900 – 1000	1090
Cost ($/lb)	1300*	20

**Cost is for Gamma Met PX Titanium Aluminide Alloy fabricated by Plansee, Austria*

As shown in Table 2, Titanium aluminides lack considerably in fabrication costs to Ni-based superalloys. Along with this, the mechanical properties such as RT ductility, and yield strength are also low when compared to Ni-based superalloys. Over the past fifteen years, considerable research has been done to refine the microstructure of titanium

aluminides, which has resulted in enhancement of their ductility as well as strength. Below is a general overview of titanium aluminides and its phases.

1.1.5 Phases of Titanium Aluminides

Titanium aluminides have been found to exist in three different phases, namely Ti_3Al (α_2), TiAl (γ), and $TiAl_3$. Of these phases, only the Ti_3Al (α_2), and TiAl (γ) phases have been found to be of any engineering significance. The phase diagrams in Figure 5 and Figure 6 show the aforementioned phases. As shown, the Ti_3Al (α_2) phase has an aluminum content exists between 22% to 39% (at%)[1], while the TiAl (γ) phase contains 48.5% to 66% (at%) Aluminum. A dual phase of titanium aluminides with a mixture of α_2 and γ phase exists between 37% to 49% aluminum content [21].

The α_2 phase has been found to exhibit good high temperature strength, but has very low ductility. Along with this, it also has a high rate of oxygen and hydrogen absorption, which in turn leads to further embrittlement at higher temperatures [22; 23]. On the other hand, the γ phase exhibits excellent oxidation resistance and has very low hydrogen absorption, but its RT ductility is close to none. Research has been conducted in refining the microstructure of these phases as well as their micro-alloying [24]. But none of the problems associated with these phases have been completely solved. Hence, these two phases by themselves do not have much of engineering significance. But a mixture of these two phases which exists between 40 to 48 weight % of Aluminum has been found to be very viable for several structural applications [25; 26].

[1] All the elemental concentrations mentioned henceforth will be in at%, unless specified otherwise.

This dual $\alpha_2+\gamma$ phase has been found to be very sensitive to its microstructure, grain size, and small volumes of micro-alloying constituents [27]. There have been several techniques, which have been established to refine the microstructure along with small micro-alloying additions by which the dual phase has exhibited ductility as high as 6% [28]. Additionally, the dual phase alloys have also exhibited RT and high temperature strengths equivalent to that of superalloys [29]. The creep and oxidation resistance have also be shown to be acceptable for temperatures up to 850^{o}C [2; 30].

1.1.6 Alloy Composition and Microstructure

The dual phase of titanium aluminides have exhibited a wide range of microstructures depending on the heat-treatment. These microstructures have been broadly classified into four categories, namely 1) Near-Gamma, 2) Duplex, 3)Nearly-Lamellar, and 4) Fully Lamellar [27]. Of these microstructures, the duplex and fully lamellar microstructure have exhibited mechanical properties conducive for a range of commercial applications [31].

As shown in Figure 6, the fully lamellar microstructure is obtained by heat-treatment at temperature (T1 in Figure 6) in the pure α phase field. Upon cooling to RT, the α-Ti phase precipitates into alternate plates of α_2 and γ plates forming a fully lamellar morphology. This microstructure is usually characterized with coarse grains in the range of 200μm to 1000μm.

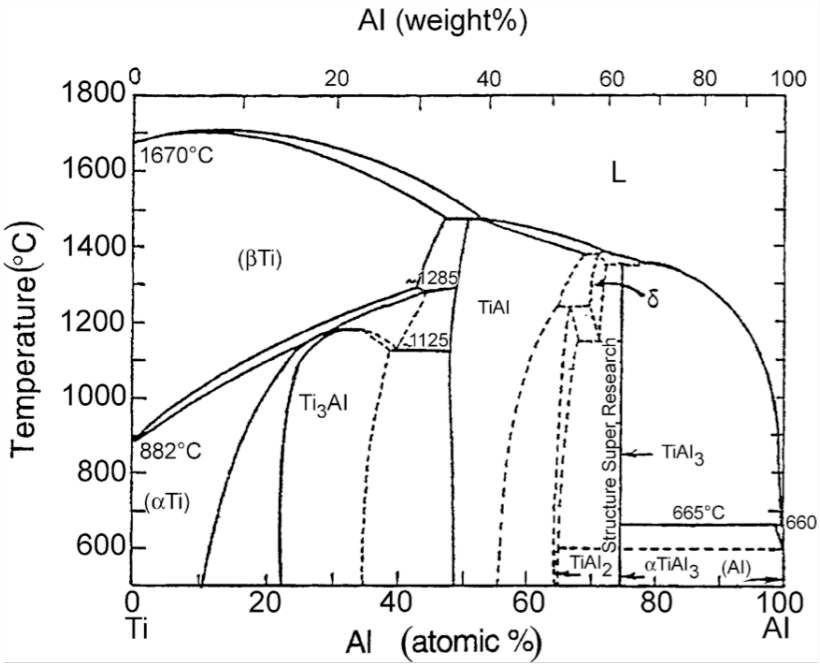

Figure 5: Ti-Al phase diagram [9]

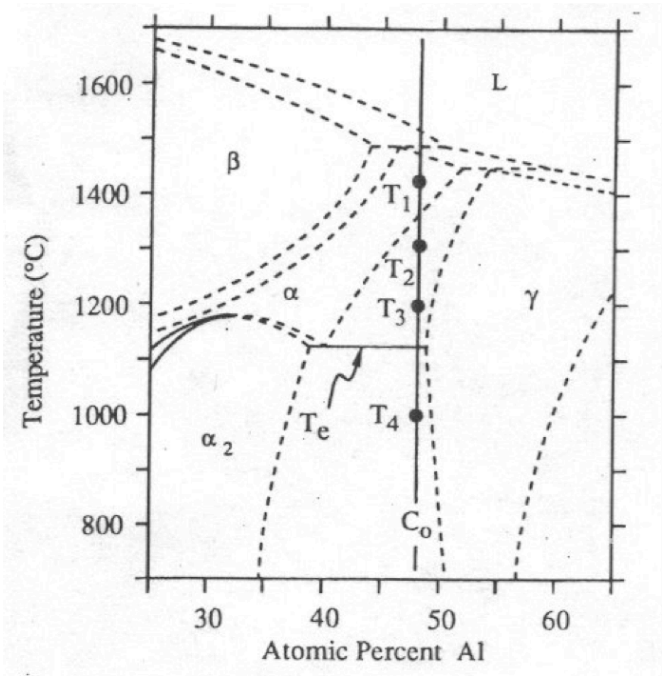

Figure 6: Central portion of the Ti-Al phase diagram [27]

The duplex microstructure is obtained by heat-treatment in the $\alpha+\gamma$ phase field at a temperature (T3 in Figure 6) where the α/γ phase volume ratio is equal to 1. The duplex microstructure consists of fine fully lamellar colonies along with equiaxed gamma grains. The mixture of these two grain morphologies forms a very fine microstructure with an average grain size in the range of 10μm.

The nearly-lamellar microstructure forms at an intermediate temperature (T2 in Figure 6) between that of fully lamellar and duplex in the $\alpha+\gamma$ phase field, where the α/γ phase volume ratio is greater than 1. It is characterized by a majority of lamellar colonies with some equiaxed gamma grains forming an average grain size in the range of 150μm to 200μm.

Finally, the Near-gamma microstructure is formed by heat-treatment at much lower temperatures (T4 in Figure 6) in the $\alpha_2+\gamma$ phase field. This microstructure is characterized by equiaxed gamma grains with α_2 precipitates forming at the grain boundaries. The average grain size for this microstructure usually ranges between 30μm to 50μm.

Due to its very fine grain size, the duplex microstructure exhibits the best ductility and strength at RT, but at higher temperatures creep and fatigue resistance is very low. The fully lamellar microstructure on the other hand is crippled with low ductility and strength due to its coarse grain size, but has excellent creep and fatigue resistance properties. Hence, over the past decades, the development of gamma titanium aluminides have been geared towards development of microstructures with the best of duplex and fully-lamellar microstructure properties [32; 33; 34].

As shown in the phase diagram, at >50% Al, titanium aluminides exist in the pure gamma phase. The microstructure for this alloy composition is characterized by equiaxed gamma grains exhibiting no ductility. Even after microstructural refinement and small alloy additions this alloy composition shows very little improvement in ductility. Therefore, this alloy composition has been considered of no engineering significance [35].

The alloy composition with Aluminum concentration <40% results in the formation of α_2 (Ti_3Al) phase. This phase exhibits better RT ductility than alloy composition with Al concentration >50% (pure γ phase). Yet the ductility is unacceptable from an engineering standpoint. The α_2 (Ti_3Al) phase, when alloyed with high Nb content (>10 wt%), is known to respond to thermo-mechanical treatment to produce a range of microstructures similar to the dual phase ($\alpha_2 + \gamma$) alloys. These microstructures as shown in Figure 8, are Fully lamellar, bi-modal and equiaxed.

Similar to the dual phase ($\alpha_2 + \gamma$) alloys, the range of microstructures in α_2 alloy exhibit a host of desirable properties. The bi-modal microstructure exhibits good ductility, but the creep resistance over 600^{o}C is an issue. Fully lamellar microstructure exhibits excellent creep properties, but its RT ductility is very low. By varying the Nb concentration in the α_2 phase, the RT ductility for α_2 phase was increased to as high as 4-5%. The ternary α_2 alloys, that have been widely researched widely include Ti-24%Al-11%Nb and Ti-25%Al-10%Nb-3%V-1%Mo (at%). Due to large additions of Nb, the density corrected strength for these alloys and similar terenary alloys was equivalent to that of conventional titanium alloys and Ni-based superalloys [20]. Hence, further development of these alloys has not received much attention.

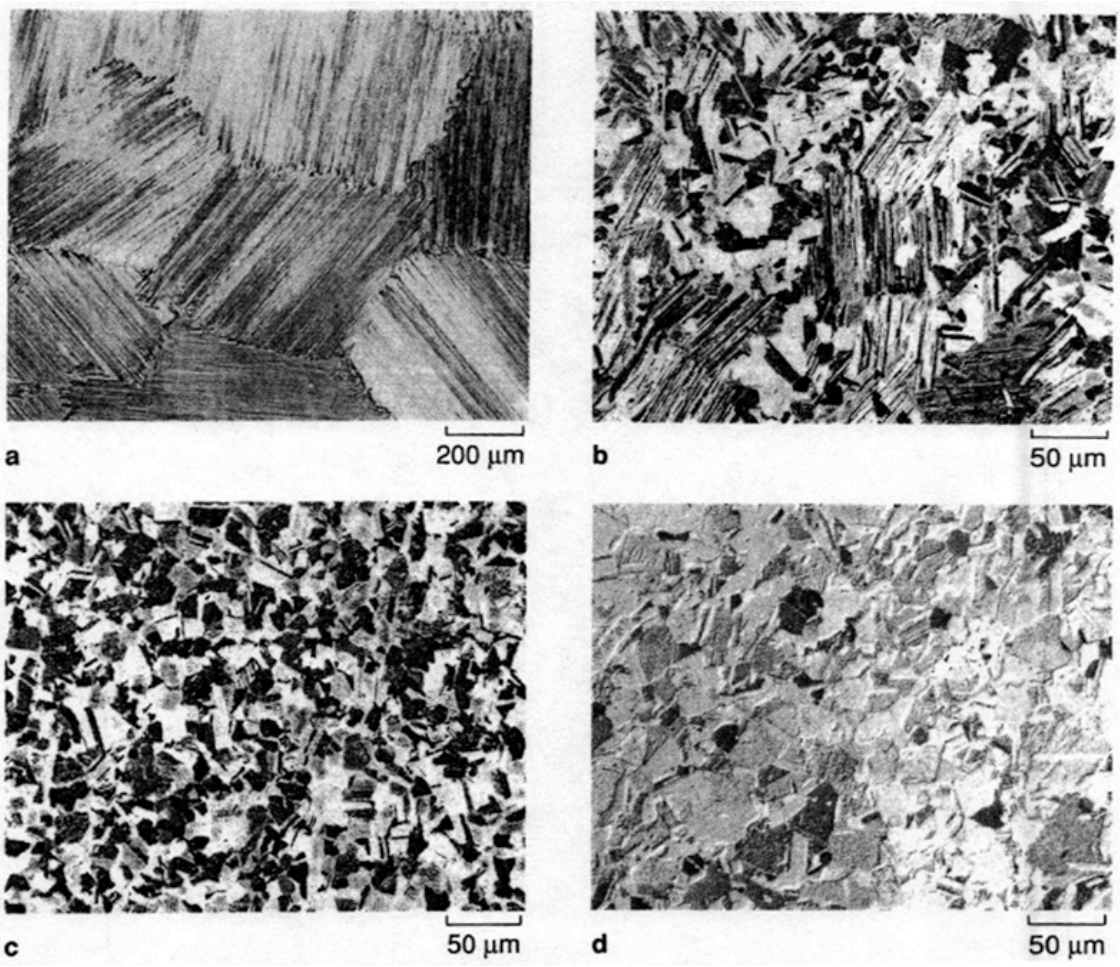

Figure 7: Microstructure types in dual phase titanium aluminides a) Fully Lamellar, b) Nearly Lamellar, c) Duplex, and d) Near-gamma [35]

The alloy composition with Al concentration between 40% to 48.5% produces the dual ($\alpha_2 + \gamma$) phase alloys. As discussed earlier, these alloys exhibit a range of microstructural morphologies depending on the thermo-mechanical processing. Several researchers have shown that ductility of these dual phase alloys increases with the increase in Al concentration up to 48% and then decreases with increase in Al

concentration beyond 50% [19; 35; 36]. As shown in Figure 9, Ti-48Al exhibits the maximum ductility in a Ti-Al intermetallic binary alloy. The specific ductility of the alloy further depends on the microstructure type and grain size, which in turn is governed by thermo-mechanical processing. Hence, the actual ductility of the alloys is not listed in Figure 9.

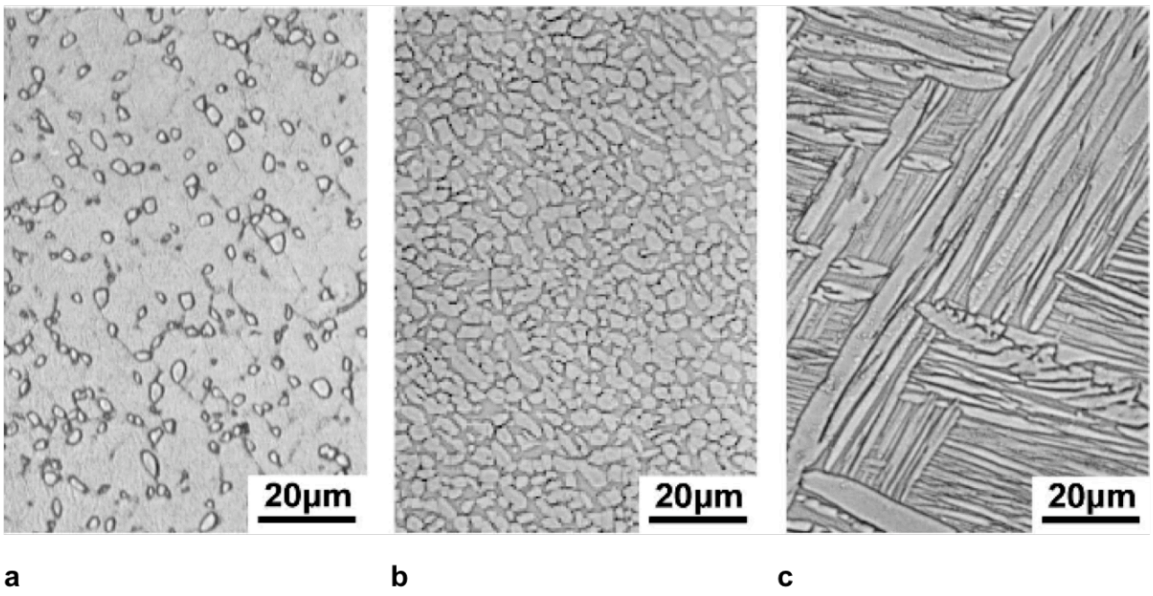

Figure 8: Microstructures of α_2 created by different thermo-mechanical treatments, (a) Bi-modal (b) Equiaxed, and (c) Lamellar [10]

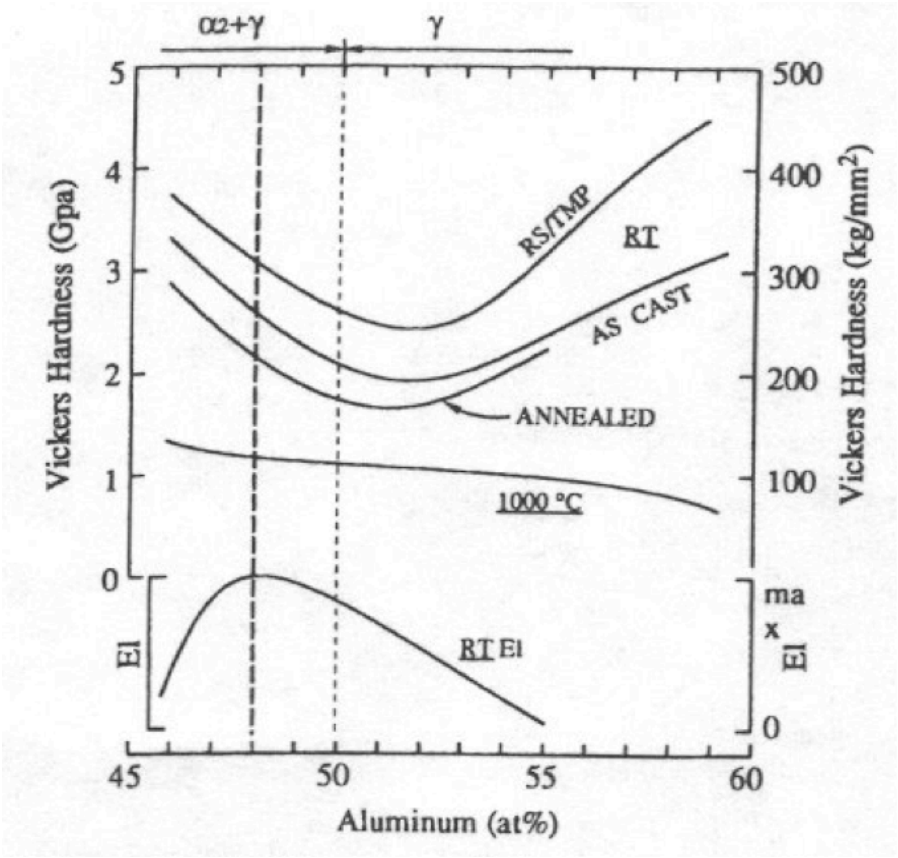

Figure 9: Elongation and Vickers Hardness of Ti-Al binary alloys measured over a range of Al concentrations (at%). The Vickers hardness is shown for as-cast, thermo-mechanically processed, and annealed material at RT as well as at 1000°C [19]

1.2 Factors Affecting Mechanical Properties

1.2.1 Ductility

The duplex microstructure formed with fine lamellar colonies and equiaxed gamma grains exhibit the best ductility in dual phase alloy. The presence of the lamellar structure aids the deformation mechanisms of the gamma phase [37]. The presence of

lamellar structure is usually characterized by a ratio of lamellar grains to that of the gamma grains (L/γ). In general, the ductility in the dual phase alloys is dictated by four main factors, 1) Grain size, 2) L/γ ratio, 3) Changes in lattice dimensions, and 4) Impurity level [28; 35]. As discussed earlier, decrease in grain size leads to increase in ductility. This is due to the fact that as the grain size decreases, the volume of defects such as grain boundaries increase, which in turn aids in the deformation mechanisms. The L/γ ratio of 0.3 to 0.4 produces the maximum ductility in the dual phase alloy. The L/γ ratio is further dependent on the α_2/γ ratio. The α_2/γ phase ratio of 3% to 15% exhibits maximum ductility. Above this range the grain growth becomes pronounced, when heat-treated in the $\alpha + \gamma$ phase field and below it the brittle α_2 eliminates the beneficial effect of refined microstructure. All these values are mainly governed by the Al concentration and are in the optimum range, when the Al concentration is 48%. Therefore, Ti-48Al alloy exhibits the best ductility.

The lattice dimension as controlled by the tetragonality ratio (c/a) and unit cell volume has a significant impact on ductility. The γ phase crystallizes into the $L1_0$ type face centered cubic structure and has a small tetragonality ratio. This ratio decreases as the Al concentration is decreased. A decrease in the c/a ratio or an increase in the symmetry of the crystal structure increases ductility in the γ phase. Also, decreasing the unit cell volume of the lattice increases ductility. This can be achieved by adding small ternary or quaternary alloying constituents. An in-depth discussion of ternary and quaternary alloying additions is presented in a later section. Finally, by reducing of impurities such as Oxygen and Nitrogen, the ductility has been observed to increase

significantly. For example, reduction of Oxygen from 800ppm to 370ppm increased the ductility from 2% to 2.7%.

1.2.2 Creep Resistance

The creep resistance in dual phase titanium aluminides is mainly controlled by the microstructural morphology and Aluminum content. An increase in Al content usually increases creep resistance. Fully lamellar structures with coarse grain size show better creep resistance over fine grained duplex microstructures. The increased creep resistance for a lamellar structure is attributed to the α_2 laths acting as reinforcements [35]. The creep-rupture strength is higher for duplex microstructures at temperatures up to 650^{o}C, above which the lamellar structure shows higher rupture strength. In general, the fully lamellar microstructure has been found to be more conducive to creep resistance. But the problem associated with fully lamellar structure is its low RT ductility due to its large coarse grains. Therefore, a lot of research effort is being directed towards decreasing the grain size of the fully lamellar microstrucutre [35; 37].

1.2.3 Fatigue Life

The factors affecting fatigue are similar to that creep. The duplex microstructure shows high fatigue crack growth rates, while the crack growth in fully lamellar microstructure is a slow process [38]. Upto 800^{o}C, fine grained duplex microstructure increases fatigue life, but at higher temperatures, the fully lamellar microstucture exhibits longer fatigue lives [10].

1.2.4 Fracture Toughness

The fracture toughness for the fine grained duplex microstructure is found to be in the range of 10 MPa√m to 16 MPa√m. These values are much higher for fully lamellar microstructures and are found to be as high as 30 MPa√m. It has been observed that the duplex microstructure exhibits little plastic strain near the onset of crack extension and no resistance to crack propagation, whereas the lamellar structure yields large plastic strains near the crack tip and increased resistance to crack propagation with crack length [36].

1.2.5 Tensile Strength

The tensile strength of dual phase titanium aluminides is inversely proportional to the grain size as expected from the Hall-Petch relationship [39]. Due to the coarse grain size in fully lamellar microstructures, the tensile strength is low compared to that of fine grained duplex microstructure. The tensile strength shows an anomalous behavior at high temperatures, where it shows an increase in strength with increase in temperature up to a certain point and then shows a decrease in strength with the increasing temperature. This behavior has been found to be characteristic of intermetallics due to their long range ordering. The increase in yield strength with temperature in TiAl can be explained by the anomalous hardening caused due to cross-slip of dislocations on to octahedral planes. This will be discussed in detail in the section describing the deformation mechanims in TiAl.

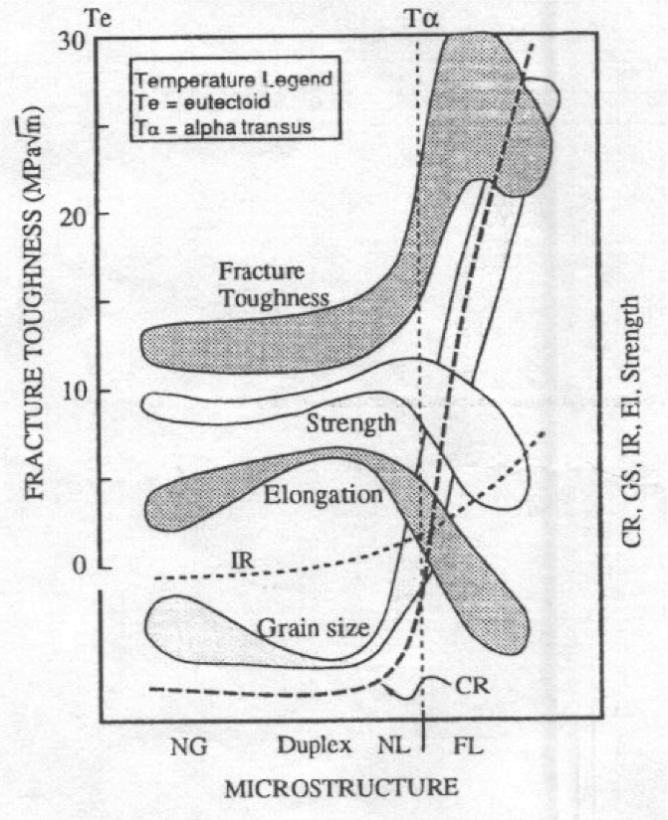

Figure 10: Dependence of mechanical properties such as fracture toughness, strength, elongation, impact resistance (IR), creep resistance (CR), and grain size on the microstructure type, where NG is Near-Gamma, NL is nearly lamellar and FL is Fully Lamellar [35].

1.2.6 General Remarks

As discussed above, the mechanical properties of dual phase titanium aluminides are very sensitive to microstructural morphology. The duplex microstructure exhibits good RT ductility and strength, but for high temperature properties such as creep and fatigue resistance, a fully lamellar microstructure is desirable. The low RT ductility and strength of fully lamellar microstructure is due to its coarse grains. By decreasing the grain size in

fully lamellar structure, the RT ductility and strength are expected to increase. There have been several thermo-mechanical processing routes suggested to obtain a fine grained fully lamellar structure. To further understand the evolution of microstructures after thermo-mechanical processing, the knowledge of phase transformations in the dual phase titanium aluminides is important. The next section discusses various phase transformation mechanisms in dual phase titanium aluminides.

1.3 Microstructural Evolution and Phase Transformations

As discussed earlier, the microstructure of the dual phase titanium aluminides can be broadly classified into four types, 1) Near-Gamma, 2) Duplex, 3) Nearly Lamellar, and 4) Fully Lamellar. In the following paragraphs, the evolution of these microstructures is discussed.

1.3.1 Near Gamma Microstructure

The Near-Gamma microstructure is formed when the material is heat-treated in the $\alpha_2+\gamma$ phase field. Heat-treatment in this phase field results in the coarsening of the existing γ grains. The microstructure as shown in Figure 7d, is characterized by coarse gamma grain regions with fine gamma grain stringer regions with dispersed alpha-2 particles.

1.3.2 Duplex Microstructure

The duplex microstructure is produced by heat treatment in the $\alpha+\gamma$ phase field. The temperature in the $\alpha+\gamma$ phase field is such that the α/γ volume ratio is close to 1. In this case, the heat-treatment results in the dissociation of the existing α_2 particles. Additional α precipitates are nucleated to grow into α plates in the {111} habit planes at the expense of gamma phase. The initially predominant gamma phase is gradually reduced in volume until the equilibrium volume fraction is reached and grain growth occurs. The growth of gamma grains is limited by the dispersed alpha phase, which also experiences growth. These competitive processes result in the formation of a fine grained structure as shown in Figure 7c.

1.3.3 Nearly-Lamellar Microstructure

At temperatures greater or lower than where the duplex microstructure forms (i.e where the α/γ volume ratio is close to 1) coarsening of the predominant phase occurs. Hence heat-treatment at temperatures below the duplex microstructure temperature leads to coarsening of gamma grains and formation of Near-Gamma microstructure, while heat-treatment above the duplex microstructure temperature results in the coarsening of alpha grains and formation of Nearly-Lamellar microstructure. The Nearly-Lamellar microstructure is characterized by coarse lamellar structure with fine gamma grains.

1.3.4 Fully Lamellar Microstructure

Finally, heat-treatment in the alpha phase field above the alpha-transus line (T_α) results in the formation of large grained fully lamellar microstructure. The lamellar structure forms in three different ways and hence is classified in to three different types: type I, II, and II [27; 28].

Type I lamellar structure is formed by heat-treatment above the T_α line followed by air cooling. It is formed via the following reaction.

$$\alpha \rightarrow \alpha + \gamma_p \rightarrow L(\alpha/\gamma) \rightarrow L(\alpha_2/\gamma)$$

In this reaction, plate like gamma precipitates (γ_p) begin to precipitate out of alpha matrix at the $\alpha/\alpha+\gamma$ line and grow radially to result in the high temperature lamellar structure, $L(\alpha/\gamma)$. This structure transforms at low temperatures to $L(\alpha_2/\gamma)$ structure simply by $\alpha \rightarrow \alpha_2$ ordering reaction. This occurs below the $\alpha/\alpha+\alpha_2$ line.

Type II lamellar structure is observed in the duplex microstructure. In this structure, the alpha-2 plates contain anti-phase boundaries (APB) which are continuous across the thin gamma plates. For this type of lamellar structure, the nucleation of gamma precipitates (γ_{pt}) and their growth into plates (γ_p) is preceded by the $\alpha \rightarrow \alpha_2$ ordering reaction. The whole process can be expressed as

$$\alpha \rightarrow \alpha_2 \rightarrow \alpha_2 + \gamma_{pt} \rightarrow \alpha_2 + \gamma_p \rightarrow L(\alpha_2/\gamma)$$

Type III lamellar structure is formed when the heat-treatment is done well below the duplex microstructure temperature. Here the predominant phase is γ with minor α_2 particles (α_2^p). Upon heating, the α_2^p in the gamma matrix (γ_m) disorders to α^p and grow into alpha plates (α_p) to yield a lamellar structure $L(\gamma/\alpha)$, which upon cooling transforms

to lamellar structure L(γ/α_2) by simple $\alpha \rightarrow \alpha_2$ reaction. The entire reaction can be expressed as follows:

$$\gamma_m + \alpha_2^p \xrightarrow{heating} \gamma_m + \alpha_p \rightarrow L(\gamma / \alpha) \xrightarrow{cooling} L(\gamma / \alpha_2)$$

1.4 Crystal Structure and Deformation Mechanisms

A review of crystal structure and deformation mechanisms of titanium aluminides gives a deeper insight into the effect of microstructural morphology on its mechanical properties.

1.4.1 Crystal Structure

The γ-TiAl phase has (ordered face centered tetragonal) $L1_0$ type structure as shown in Figure 11a. The tetragonality is due to different atomic radii of Ti and Al. For the stoichiometric compound, the tetragonality ratio is 1.02. This tetragonality ratio increases to 1.03, with increasing aluminum concentration and decreases to 1.01 with decreasing aluminum concentration [19]. The α_2-Ti_3Al phase has a DO_{19} (hexagonal closed packed) type structure as shown in Figure 11b.

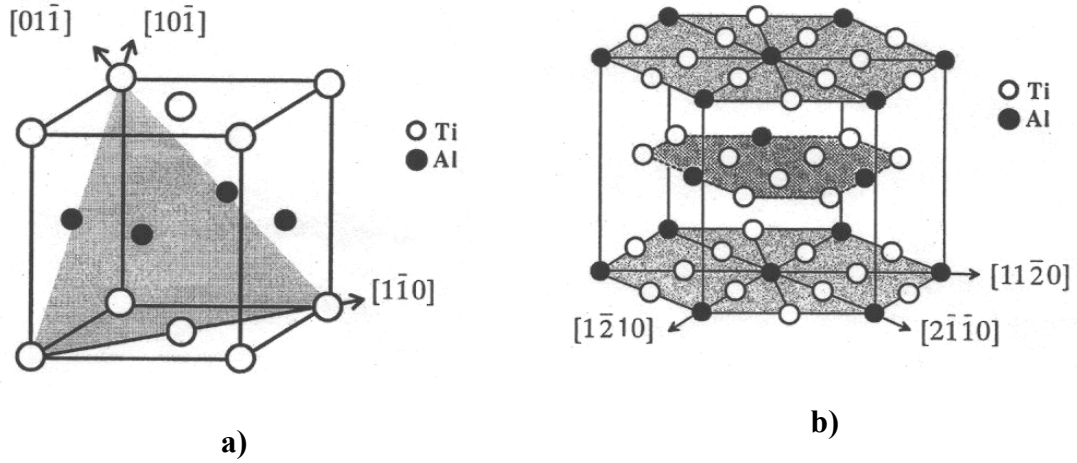

Figure 11: Crystal structure for, a) γ-TiAl, and b) α_2-Ti_3Al

1.4.2 Deformation Mechanisms

It has been established that the main deformation modes in γ-TiAl are slip and twinning, both operating on the close-packed {111} planes [40]. Due to the face-centered cubic type structure of the γ-TiAl phase, slip occurs on the close-packed {111} planes. The layered arrangement of atoms on the successive (002) planes and the tetragonality ratio of 1.02 results in two types of dislocations with ½<110> type Burgers vectors on {111} planes.

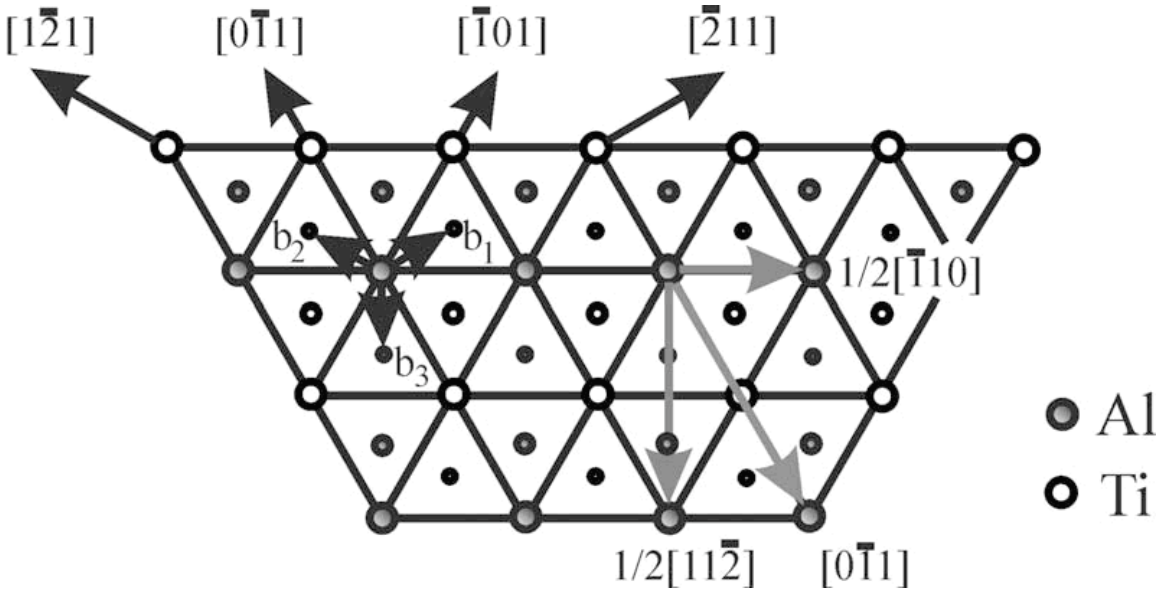

Figure 12: Potential slip and twinning sytems in the γ-TiAl {111} planes (Circles of varying sizes indicate atoms on different parallel {111} planes) **[41]**

More specifically these are ordinary dislocations with Burgers vector ½<110], and superdislocations with Burgers vectors <101] [42; 43]. (For γ-TiAl, the miller indices convention was introduced by Hug et al, 1988, where in the notation <hkl] or {hkl] only h and k are mutually permutable, while l is fixed and can be positive or negative) [44]. In the single phase γ-TiAl <101] superdislocations dominate at low temperatures while at high temperatures (above about 800°C) slip by ½<110] ordinary dislocations, and also twinning, become controlling deformation modes. In contrast, in the dual phase TiAl with lamellar structure, twinning and glide of ½<110] ordinary dislocations prevail at low temperatures and glide of superdislocations becomes significant only at high temperatures. The ½<112] type superdislocations have also been reported in TiAl [19].

Figure 12 shows the ordinary ½<011] dislocations as well as the <011] and ½ <112] type superdislocations.

The $L1_0$ structure can be twinned by the {111}<112] variants of the normal fcc twinning mode. As shown in Figure 12, the Burgers vector $b_3 = 1/6[11\bar{2}]$ preserves the order of γ-TiAl and this twinning mode is therefore called true twinning. Partial dislocations by Burgers vectors $b_1 = 1/6[\bar{2}11]$ and $b_2 = 1/6[\bar{1}\bar{2}1]$ change the order of γ-TiAl and are called pseudo-twinning.

At RT, the <011] type superdislocations have very limited mobility due to the covalent nature of Ti-Ti, and Ti-Al bonds. Their mobility is further inhibited due to the formation of extrinsically faulted dipoles. Segments of the trailing superpartials, 1/6[112] type, form faulted dipoles, which must be extended as deformation proceeds [45]. This explains the low RT ductility in single phase γ-TiAl, where <011] superdislocations are the dominant deformation modes at RT. <011] type superdislocations can be dissociated into two ½<011] dislocations separated by an antiphase boundary (APB). The <011] type superdislocation can be further dissociated by

$$[10\bar{1}] = \frac{1}{6}[11\bar{2}] + \frac{1}{2}[10\bar{1}] + \frac{1}{6}[2\bar{1}\bar{1}]$$

with superlattice intrinsic stacking fault (SISF) between $1/6[11\bar{2}]$ and $1/2[10\bar{1}]$ partials, and the complex stacking fault (CSF) between $1/2[10\bar{1}]$ and $1/6[2\bar{1}\bar{1}]$ partials [46].

In dual phase TiAl, the presence of α_2-Ti_3Al as secondary phase results in ½<110] ordinary dislocations and twinning to become the dominant deformation modes. Twinning is mainly caused by the presence of lamellar structure in dual phase TiAl [47;

48]. As discussed earlier, the lamellar structure is formed by heat-treatment in the α or α+γ phase field. The formation of γ plates from α is described above. The nucleation from the α phase proceeds from the stacking fault by the movement of $1/3<1010>$ Shockley partials [20; 28]. The resulting lamellar structure has the crystallographic orientation relationships $[011]_\gamma //[11\bar{2}0]_{\alpha_2} | (1\bar{1}1)_\gamma //(0001)_{\alpha_2}$ between the alpha-2 plates and gamma plates, with gamma plates being twin related. The [101], and [110] directions are not equivalent to [011] direction on {111} plane due to the tetragonality in the $L1_0$ structure of γ phase. Directions of $<1\bar{1}20>$ on the basal plane in the α phase (hexagonal closed packed) and α_2 phase (hexagonal $D0_{19}$) are all equivalent as shown in Figure 12. Hence, six interfaces arise from the combination of the three possible directions of the c-axis of the γ phase and the ordered nature of the two phases [37].

The mechanical properties of the lamellar microstructures in TiAl depend on the lamellar orientation with respect to the loading axis and lamellar microstructure variables such as grain size, thickness, and spacing of γ and α_2 lamellae and γ domain size. However, the lamellar orientation has far more influence than lamellar microsturctural variables. In order to fully understand the effect of lamellar orientation on its properties, TiAl crystals where the entire crystal consists of only a single lamellar grain were produced and characterized. Since numerous thin twin related lamellae are contained in the major constituent γ phase, these crystals are named polysynthetically twinned (PST) crystals from analogy with the phenomenon “polysynthetic twinning”, observed in mineral crystals.

1.4.3 Polysynthetically Twinned (PST) Crystals

As mentioned above, the PST crystals have a single lamellar grain. The mechanical properties of the PST crystals depend strongly on the lamellar orientation relative to the loading axis. PST crystals also display anisotropic macroscopic flow behavior. When the orientation of the lamellae is perpendicular to that of the loading axis, the PST crystal exhibits excellent strength and poor ductility. In the parallel orientation of the lamellae with respect to the loading axis, some ductility and strength was observed. The strength in this case is not as high as the perpendicular orientation case. These deformation modes in parallel and perpendicular directions are referred to as hard modes.

At the intermediate orientations, such that the lamellae form an angle of 30^{o}~60^{o} with respect to the loading axis (soft mode), the yield stress is much lower but the elongation is significantly higher than the hard modes. The orientation dependence of the yield stress and ductility of PST crystals is due to the fact that shear occurs parallel to the lamellar boundaries when the lamellar orientation is such that it forms an angle of 30^{o}~60^{o} with the loading axis (deformation in soft mode) but it occurs mostly on {111} planes intersecting the lamellar boundaries when the lamellae is either parallel or perpendicular (hard mode) to the loading axis.

1.4.4 Effect of lamellar structure on deformation modes

In dual phase TiAl with duplex and fully lamellar microstructure morphologies, the presence of α_2-Ti_3Al phase is usually in form of lamellar structure. In a lamellar structure, the orientation of the lamellae with respect to loading axis plays a significant role in the control of deformation mechanisms. As discussed above, with more lamellae

oriented in the soft mode the ductility increases. Hence, it is desirable to have maximum lamellae oriented in the soft mode. In different grains lamellae will be oriented at different angles relative to stress-axis, and when grain size is large, it is likely that fewer grains are oriented favorably for slip. Hence, fully lamellar structures with coarse grains suffer from low ductility.

On the other hand, duplex microstructure with fine grains exhibit good ductility. Due to presence of more grains per unit volume the probability of grains with lamellae oriented in the soft mode will increase. As a result, the ductility in duplex microstructure is higher than that in fully lamellar microstructure. A decrease in grain size has been correlated to increase in ductility by several researchers [36]. The duplex microstructure does not perform well in terms of creep, and fatigue resistance at high temperatures compared to that of fully lamellar microstructure. Hence, it has been suggested by several researchers that refining the grain size in fully lamellar microstructures could potentially solve the problem of low ductility.

As discussed earlier, fully lamellar microstructures are formed by heat-treatment in the α phase field. The diffusion process in the α phase field is very rapid due to thermal activation and the absence of second phase barriers. Therefore the grain growth is also rapid. In order to circumvent this, several thermo-mechanical treatments along with small alloy additions have been proposed. These will be discussed in the next sections.

1.4.5 Effect of α_2-Ti_3Al on deformation modes

As mentioned earlier, in single phase γ-TiAl the deformation modes are dominated by <101] type dislocations. Ordinary dislocations of ½<110], and twinning are hardly observed. But in two phase (α_2+γ) TiAl, where the dominant phase is γ-TiAl the deformation modes are dominated by ordinary dislocations ½<110] and twinning. This phenomenon has been explained in terms of α_2-Ti_3Al acting as a gettering agent to improve the purity of γ-TiAl phase [45].

In other independent studies it has been concluded that by reducing interstitials and impurities in nominally pure γ-TiAl phase, the directionality of the bonds between the Ti atoms reduces. This in turn leads to increased mobility of dislocations with ½<110], and 1/6<112] Burgers vectors. The 1/6<112] Burgers vectors are order twinning defects. It has been proposed that in dual phase (α_2+γ) TiAl, where the dominant phase is γ-TiAl, the α_2-Ti_3Al laths getter the interstitial impurities from their adjacent γ-TiAl laths. Hence, an increase in the mobility of dislocations with ½<110], and 1/6<112] Burgers vectors is observed in dual phase (α_2+γ) TiAl. The solubility of interstitial impurities in α_2-Ti_3Al is greater than that in γ-TiAl.

1.4.6 Anomalous Yield Strength Behavior

In single phase γ-TiAl, anomalous increase in flow stress is observed with increase in temperature upto a certain point. This increase in strength usually begins to occur around 200^{o}C and peaks between 600^{o}C to 700^{o}C depending on the alloy composition. As discussed earlier, in single phase γ-TiAl room temperature deformation is controlled by <011] superdislocations, which have limited mobility. As the temperature increases,

ordinary dislocations ½<110] and twinning become active and are relatively mobile, but the <011] dislocations become increasingly blocked as they adopt a thermally activated non-planar configuration and thereby give rise to the flow anomaly [49]. These <011] superdislocations dissociate into a primary plane with stacking faults and APBs as discussed earlier. With the increase in temperature, segments of the <011] cross-slip onto the adjoining octahedral planes [50]. Since these cross-slipped superdislocations are highly immobile, an increase in flow stress with increase in temperature occurs. But as temperature increases further, the <011] superdislocations dissociate into unit ½<110] and ½<112] superdislocations, which are sufficiently mobile such that the strength decreases following the flow stress peak.

In the dual phase TiAl, similar behavior is observed except that the temperature range of anomalous yield strength behavior is a bit contracted and flow stress peaks appear at a bit lower temperatures. The deformation mechanism in dual phase TiAl responsible for such behavior is the interaction of ½<110] screw dislocations on adjoining {111} planes. These interactions become frequent at higher temperatures and as a result an increase in strain is followed by formation of jogs, dislocation dipoles and debris defects [51]. The ½<110] dislocations are pinned by these defects and the number of pinned dislocations increases with the temperature. At higher temperatures due to thermal activation, the jog-dislocation climbing occurs, which results in decreased strength with temperature [52].

1.4.7 General Remarks

The deformation mechanisms in TiAl have been investigated over years and have been helpful in explaining the effect of microstructural morphology especially that of lamellar structure on the mechanical properties of TiAl. From the discussions above, several conclusions can be made regarding approaches to enhance mechanical properties in TiAl.

i. The brittle nature of single phase γ-TiAl is due to dominant nature of the <101] type dislocations, which are primarily sessile due to extrinsically faulted dipoles.

ii. The glissile slip systems of twinning and ordinary dislocations, 1/6<112] and ½<110], respectively become active due to the presence of α_2-Ti_3Al. The secondary α_2-Ti_3Al phase acts as a gettering agent to improve the purity of γ-TiAl phase and hence makes slip via ordinary dislocations and twinning dominant.

iii. The deformation modes in lamellar structures are dependent on its orientation (soft mode or hard mode) with respect to the loading axis. Fully lamellar microstructures with good RT ductility and high strength can be developed by refining its grain size.

The discussion so far has been limited to the binary TiAl alloys. Significant accomplishment has been made in enhancing the mechanical properties of TiAl by small alloy additions. The next section will look in to various alloy additions explored in TiAl so far and its effect on mechanical properties. Along with this, three state-of-the art alloys developed by several commercial vendors are presented at the end.

1.5 Alloy Development

The dual phase ($\alpha_2+\gamma$) TiAl have shown good response to small alloying additions. In general, the alloying additions for TiAl can be broadly divided into three different categories [41] with the following compositions (in at%):

Ti_{45-52}-Al_{45-48}-X_{1-3}-Y_{2-5}-$Z_{<1}$

Where X, Y and Z represent the three categories of alloying additions. These alloying elements more or less affect the position of the phase boundaries in the Ti-Al binary phase diagram [19; 27; 53].

The X additions are usually elements which increase the ductility of TiAl. They lower the stacking fault energy and thereby increase the propensity of twinning. Usually elements such as Cr, Mn, and V fall in this category.

The Y additions such as Nb, Ta, W, and Mo increase the oxidation and creep resistance at high temperatures in TiAl. The effect of Nb in varying levels is discussed in more depth in the next section.

Finally, the Z alloying elements are usually B or C. Boron is primarily used as a grain refiner to produce fully lamellar microstructures with fine microstructures. Since, B is not soluble in TiAl, it acts as an impediment to grain growth in the α phase field to form fully lamellar structures. Carbon additions further increase the strength of TiAl due to its Ti_3AlC perovskite precipitates. C also increases the creep resistance of TiAl. The Ti_3AlC perovskites act as glide obstacles with long-range stress fields, which cannot be overcome with the aid of thermal activation [30]. Table 3 lists the mechanical properties enhanced by the various alloy additions.

Table 3: Effect of selected alloying elements on mechanical properties of TiAl.

Element	Effect
Nb	Increases oxidation and creep resistance in small amounts, also increases high temperature strength if added between 5%-10%
Ta	Increases oxidation and creep resistance and tendency for hot cracking
V	Increases ductility
W	Oxidation and creep resistance
B	Grain refiner
C	Increases creep and oxidation resistance
Cr	Increases ductility if added in small amounts; increases oxidation resistance if added in the range of 8%
Mn	Increases ductility
Mo	Increases strength, and creep and oxidation resistance.

1.5.1 Effect of Nb

Nb is especially used to increase oxidation and creep resistance. Over the years, alloys with Nb additions have been developed and can be classified into four different types [30; 54; 55].

i. Ti–48Al–2Nb

ii. Ti–(46–47)Al–(2–3)Nb

iii. Ti–45Al–(5–10)Nb

iv. Ti–45Al–(5–7)Nb–RM (refractory metals)

Alloys with high Nb content with type III and IV are also known to increase the high temperature strength by solid solution strengthening. Recently large amounts of Nb in the order of 5% to 10% have been used in TiAl alloys to form a new class of TiAl alloys known as TNB alloys [8; 56; 57; 58; 59; 60]. In these types of alloys, Nb plays a critical role in increasing high temperature strength along with creep and oxidation resistance. The Nb atoms occupy Ti atomic sites and reduce the Al content in the gamma phase. This shifts the α phase boundary to the left and thereby lowers the processing temperatures to produce fully lamellar structures. With low processing temperatures, grain growth can be controlled, which leads to the refinement of the microstructure and increase in strength.

Nb has also been reported to increase the tetragonality ratio of TiAl, which enhances its structural anisotropy and hence its strength [59]. Recently, Nb has also been reported to increase the intrinsic strength of the gamma phase in Ti-45Al alloys [61]. Twinning in TiAl has been found to be enhanced by Nb, which in turn suppresses pre-mature failure due to the inherent brittleness of TiAl [62]. Along with strengthening effects, Nb is also known to increase the diffusion activation energy in TiAl. This leads to control of high creep rates in TiAl at temperatures above 700^{o}C.

Initially, Nb was used primarily to increase the oxidation resistance of TiAl alloys [63]. This was achieved in type I and II alloys listed above by small Nb additions. The α_2 phase has a greater solubility for Oxygen than the γ phase. At high temperatures, absorption of Oxygen by α_2 results in further embrittlement of TiAl. More recently it has been reported that Nb decreases the α_2 phase in TiAl alloy and hence decreases its

Oxygen solubility [61]. Also, Nb promotes the formation of Al_2O_3 which in turn increases the oxidation resistance of TiAl.

1.5.2 State of the Art TiAl Alloys

The alloy development in TiAl over the last twenty years has resulted in four state-of-the-art alloys with exceptional high temperature mechanical properties. These four alloys are listed in Table 4 with their compositions and strengths.

Table 4: TiAl state-of-the-art alloys

Alloy Name	**Composition (at%)**	**Alloy Strengths**
General Electric, USA: *48-2-2* [10; 26]	Ti-48Al-2Cr-2Nb	Ductility, fracture toughness, and oxidation resistance
Plansee, Austria: *γ-MET* [29; 64]	Ti-45Al-(5-10)Nb-	High temperature strength, creep, fatigue, and oxidation resistance
GKSS Research Center, Germany: *TNB Alloy* [25; 65]	Ti-(45-47)Al-10Nb	High temperature strength, creep, and oxidation resistance
Martin Marietta Laboratories, USA: *XD^{TM} TiAl* [66; 67]	Ti-45Al-2Mn-2Nb-0.8B	Ductility, high temperature strength, stiffness, creep, and oxidation resistance

1.6 Manufacturing Techniques

Investment casting, ingot metallurgy (IM), and powder metallurgy (PM) are some of the popular techniques which have been used to produce TiAl parts. More recently advanced techniques such as direct rolling [18], laser forming , and mechanical alloying have been investigated with good success. Several rapid sintering/consolidation techniques such as spark plasma sintering, pulse discharge sintering and explosive consolidation have also been successful in forming TiAl with desired mechanical properties [68; 69; 70; 71; 72; 73].

One of the biggest drawbacks of TiAl compared to that of Ni-based superalloys is its production cost. This is largely due to the fact that processing techniques for materials with fairly low ductility do not exist. Further, due to the long-range ordering of TiAl up to its melting point, their processing temperatures are fairly high. This requires capital investment in processing equipment with good high temperature characteristics. Investment casting, ingot metallurgy and powder metallurgy techniques have been successful at producing TiAl parts with desirable mechanical properties only after a series of post processing steps, like hot-isostatic pressing, ageing, annealing, and hot working. This further adds to the production costs of TiAl.

Advanced techniques such as direct rolling, laser forming, and spark plasma sintering have been aimed at reducing the post-processing steps for TiAl. These processes usually require less time compared to the traditional techniques and can form complicated shapes without much post-processing. But the problems associated with these techniques involve porosity and scalability.

1.6.1 Ingot Metallurgy and Casting

Ingot metallurgy and casting routes involve producing TiAl ingots by skull melting [60]. The resulting microstructure of the ingots is characterized by large columnar grains consisting of chemical inhomogeneities, and segregation as shown in Figure 14 [19]. The ingot is then subjected to hot-isostatic pressing (HIP) to improve its homogeneity and refine the microstructure. The microstructure is further refined by ageing treatments [27]. Along with skull melting several other processes such as vacuum arc remelting, and cold-hearth plasma arc melting have also been employed. In vacuum arc remelting [74], large rods consisting of given amount of Ti, Al and master alloys are cold welded to each other in an inert atmosphere. The cold welded electrode is then melted in a vacuum arc furnace. The electrode is melted to a primary ingot, which is then remelted twice to improve chemical homogeneity and reduce segregation.

Finally, in the cold-hearth plasma arc melting process the metal alloy is melted and poured into a water-cooled copper hearth forming a solid skull. This acts like a secondary hearth of the same composition as the parent alloy. Without the solid skull, harmful refractories could be picked up and cause melt-related inclusions. This also allows enough time for inclusions to sink into the skull or dissolve into the melt before the alloy is poured into a water-cooled copper crucible for solidification. For this reason, this process is referred to as a “clean melting” process. Cold-hearth melting is an alternative method to other melting techniques, such as VAR, where alloy cleanness is of great significance. Electron beams and plasma-arc heating are both effective heat sources that are suitable for this type of clean melting.

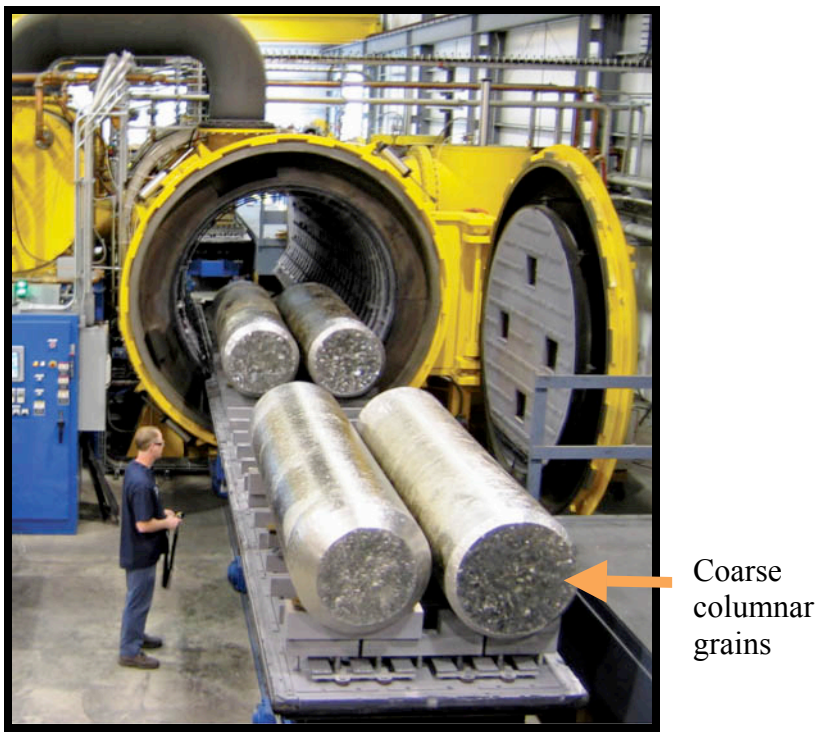

Figure 13: TiAl ingots with coarse columnar grains ready for homogenization process

As mentioned above, most of the ingot metallurgy techniques result in the formation of coarse columnar grains consisting of chemical inhomogeneity and segregation. This is solved by further post processing steps such as HIP and ageing. After this, the ingots have to be further machined or forged to desired shapes with further heat treatments to relieve any residual stresses. Figure 14 illustrates the post-processing steps required for forming a TiAl compressor blade.

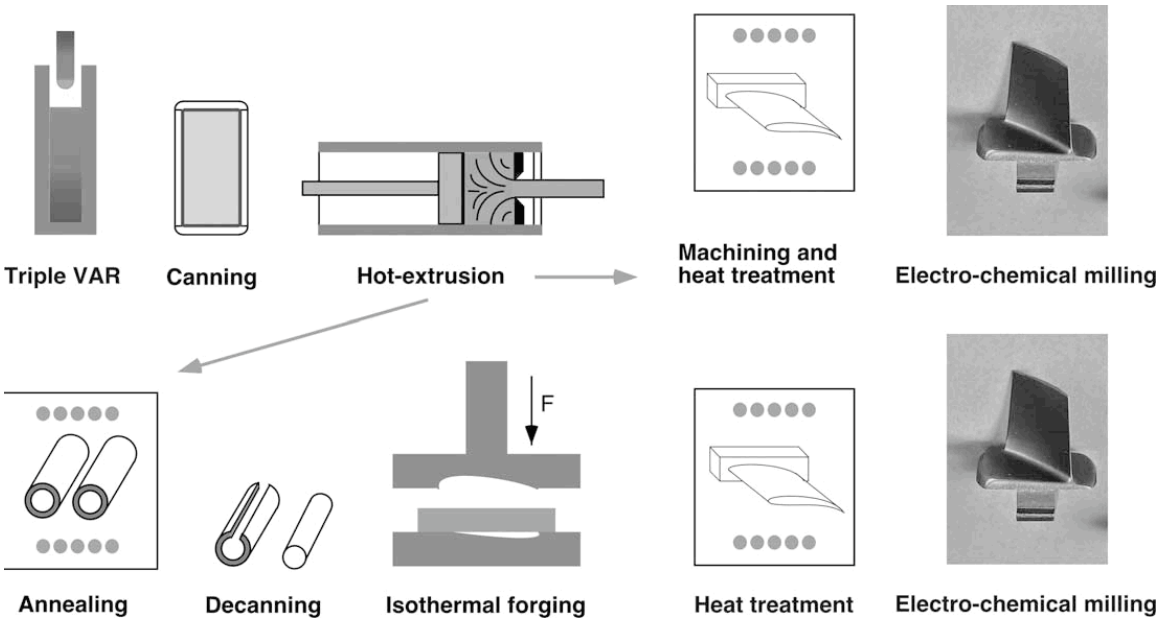

Figure 14: Processing routes required for the production of high-pressure aero-engine compressor blades from a TiAl ingot [30].

1.6.2 Powder metallurgy

Powder metallurgy (PM) offers the potential for minimizing many of the problems associated with large ingot production and reducing overall cost of the final TiAl component. Many of the problems associated with ingot metallurgy (IM), such as centerline porosity, chemical inhomogeniety, regions of varying density and microstructure can be solved by PM. Further, PM enables the development of new alloys that cannot be made by conventional IM [75].

Gas atomization of pre-alloyed powder followed by HIP or consolidation by extrusion to full density has been the general route taken in PM. Mechanical alloying (MA)of the elemental powders to form the alloy powders of TiAl has also been

investigated [76; 77; 78] with success in obtaining metastable to stable TiAl phases. One of the biggest problems associated with MA is contamination of the powders from the milling media and the container.

Hot isostatic pressing (HIP) of powder compact is a very popular PM method to produce TiAl billets [55; 79; 80; 81]. In this process, gas atomized powder of high purity is canned. The can is usually made of commercially pure Ti. The can is then degassed at ~500°C under high vacuum after which the can is sealed gas tight. The canned powder compact is subjected to isostatic pressure in the range of 100MPa to 150MPa at a temperature range of 1200^{o}C to 1400^{o}C depending on the desired microstructure. This is done for about 2 to 6 hours. The consolidated powder compact is de-canned to produce billets. Some of the post processing steps after HIP involve hot extrusion, isothermal forging and hot rolling to sheets. In HIP, the porosity in the final part is limited and the microstructure is homogeneous with little segregation. The only drawback of HIP is that it requires exposure to high temperatures for several hours which lead to grain growth. Hence, there is limited flexibility in HIP to control the grain size of the final part.

Most of the current PM processes have been successful in producing TiAl parts, which will require further hot-working or machining to produce the final component. Metal injection moulding (MIM) and spray forming are two PM methods which strive to produce near-net shape parts with minimal post processing [82]. The basic steps in MIM are the kneading of a feedstock by mixing the powders with a binder, usually consisting of wax and polymers; the moulding of the part; the extraction of most of the binder components and final sintering in order to obtain highly dense parts. Porosity and contamination are some of the challenges in using MIM for producing TiAl parts.

In spray forming, a melt stream is atomized using low pressure argon gas. The droplets and partly solidified droplets are gathered on a substrate which is positioned at a certain distance below the gas nozzle. In this way, high density deposits with high chemical and microstructural homogeneity as well as low purity levels can be obtained. There has been very limited work done on spary forming of titanium aluminides and hence the data on the spray formed components is very limited to determine it success [83].

1.6.3 State-of-the-Art in TiAl Sheet Manufacturing

Plansee, Austria has been the forerunner in producing TiAl sheet material using PM techniques. Gas atomized powders are consolidated by HIP and subsequently rolled on a conventional hot-rolling mill using Plansee's patented Advanced Sheet Rolling Process [84]. The microstructural homogeneity and mechanical properties of these sheets have been found to be consistent and superior to most TiAl based alloys. The cost for these sheets is currently at $1300/lb, but is expected to go as low as $150/lb over the years.

Although not a PM based process, a second approach has been used to produce thin γ-TiAl sheets at a lower cost [2]. In this approach, cast γ-TiAl is directly rolled into thin sheets, thereby eliminating costly and wasteful intermediate steps. Direct rolling of cast plates into thin sheets has been demonstrated for a number of γ-TiAl alloys. This process has been developed by NASA Glenn research center in Cleveland, Ohio [18]. Limited microstructural and mechanical property evaluations on these sheets have produced encouraging results. It has been estimated that the direct rolling may lead to a cost reduction of ~35% over the conventional PM and IM routes.

1.6.4 Manufacturing Challenges and Opportunities

The manufacturing techniques for TiAl via both IM and PM have been advanced enough to produce TiAl parts with desirable mechanical properties. As a result, these processes have found use in producing TiAl parts for several high temperature applications in aerospace and automobile industry. But the cost associated with TiAl, especially due to its post processing steps after ingot production or powder consolidation, has outweighed its benefits of weight savings. Hence, advanced near-net shaping manufacturing methods with minimal post-processing methods are being investigated for TiAl.

Also, methods to refine fully lamellar microstructures are being actively investigated. As discussed earlier, fully lamellar microstructures with fine grain sizes and lamellar spacing may possess mechanical properties with acceptable RT ductility and toughness and excellent high temperature characteristics such as creep and fatigue resistance. Several thermo-mechanical treatments have been employed to achieve this. These thermo-mechanical treatments are quite involved due to the complex thermodynamic Ti-Al system. Achieving thermo-dynamic equilibrium in fine spaced lamellae with small grain sizes requires carefully designed heat-treatments. Fine grained microstructures in TiAl have a tendency to deteriorate into Widmanstätten structures [65] even before reaching service temperature of the TiAl part. Therefore, a lot work has concentrated on reducing the grain size of the material by PM techniques. Here the starting powder particle size is reduced to a considerable extent so that the grain size in the consolidated sample is also small. With this technique the grain size can be lowered into the nanometer range [85]. A decrease in the grain size up to the nanometer range has the potential of increasing the strength and ductility of the material significantly [20].

High energy ball milling and attrition milling have been used to reduce powder particle size of the TiAl powders [85; 86; 87]. Pre-alloyed TiAl powders have been ball-milled for up to 50 hours to form amorphous TiAl powders with particle size in the sub-micrometer to nanometer range. One of the advantages of milling is that it disorders the lattice to improve the dislocation motion. This is especially important in TiAl, where due to its long range ordering its ductility is limited by immobility of the superdislocations as discussed above [88].

Mechanical alloying (MA) route has also been used to reduce powder particle size [89; 90; 91]. For MA, pure Ti and Al powders are ball-milled for several hours to form a Ti-Al solution, which is partly disordered and its particle size is reduced considerably from the starting elemental powder particle size.

Several studies have been conducted to consolidate the milled powders to produce TiAl with ultra-fine grains in the sub-micron to nanometer range [92; 93]. The consolidation processes used for these were typical sintering or HIP. Due to the small particle size, diffusion in the milled powders is very rapid and hence grain growth is very rapid too. The grain growth can be controlled by rapid consolidation of the powders. This approach will be discussed in the next section.

Finally, metal matrix composites (MMCs) based on TiAl have also been considered as potential solution to enhance its high temperature service range. TiAl MMCs with TiC, TiB_2, TiB, Al_2O_3 and TiN [90; 94; 95; 96; 97; 98] have been considered. TiAl MMCs reinforced with Titanium borides have been very popular due to the grain refining characteristic of Boron. XD^{TM} TiAl alloy with needle-shaped TiB_2 particulates have been produced via casting process and have displayed excellent RT

ductility and high temperature characteristics. But several studies have focused on using more economical approaches such as MA. The reinforcement and TiAl powders are mechanically alloyed and consolidated to produce the desired TiAl MMC.

1.7 Present Study

Several PM based novel manufacturing opportunities exist to produce near-net shape parts of TiAl with enhanced mechanical properties. Along with this, several new challenges emerge in terms of characterization of a whole new set of TiAl based alloys produced by these novel PM techniques. Also, challenges lay ahead in the implementation of these techniques for the industrial production of near-net shape TiAl parts.

One such novel PM technique was used to produce near-net shape TiAl parts in the present study. The research objective and the technical approach for development of this technique to produce TiAl alloys are detailed below.

1.7.1 Objective

The objective of the present study included the development of a novel manufacturing technique, using rapid powder consolidation to produce near-net shape parts of TiAl with enhanced mechanical properties. The mechanical properties of TiAl alloys can be enhanced by

i. Control of its microstructural morphology

ii. Small alloying additions, such as Nb, Cr, and B

iii. Reducing its grain size to sub-micrometer to nanometer range

iv. Reinforcement with discontinuous particulates or fibers

The above four routes to enhance mechanical properties of TiAl were investigated in conjunction with a rapid consolidation technique.

1.7.2 Technical Approach

In the present study a novel consolidation process called plasma pressure compaction (P2C) was used to consolidate TiAl powders [99; 100]. The TiAl powders were consolidated with the aim of attaining the four objectives mentioned above.
In order to control the microstructure morphology of the TiAl alloys, the powders were rapidly consolidated by P2C at different phase field temperatures to produce three characteristic microstructures. The mechanical properties of these microstructures were then characterized.

Small alloy additions were made to TiAl by consolidating gas atomized TiAl powders with small Nb and Cr additions. The effect of the alloy additions on the microstructure and the mechanical properties of TiAl was characterized. To reduce the grain size of TiAl in the sub-micrometer to nanometer range, TiAl powders were milled to reduce its particle size. The milled powders were then consolidated by P2C to produce TiAl samples with grain size in the sub-micrometer range. The effect of grain size in the sub-micrometer range on the microstructure and the mechanical properties of TiAl were characterized.

Finally, a TiAl based metal matrix composite with Titanium Boride reinforcement was developed. This was done by consolidation of blended TiAl and TiB_2 powders by P2C. The effect of the reinforcement on the microstructure and mechanical properties of TiAl was characterized.

1.7.3 Original Contributions

The major contribution of the present study is a novel manufacturing technique which rapidly consolidates titanium aluminide powders in to near-net shape parts with enhanced mechanical performance by control over microstructure morphology, phase composition, grain size, and the ability to add a discontinuous particulate reinforcement.

The manufacturing technique in the present study utilizes rapid consolidation by which the near-net shapes are formed in less than 20 minutes. In comparison to the current state-of-art processes, the rapid consolidation technique utilized in this study requires minimal pre-processing and post machining steps as shown in Figure 15. Hence, this technique further contributes to reduction of cost in manufacturing near-net shape parts of titanium aluminides.

The manufacturing technique developed in the present study can be divided in to two design steps namely: 1) powder design, and 2) consolidation conditions.

Powder Design

The powder design process involves three main control variables namely: 1) Alloy composition, 2) powder particle size, and 3) reinforcement. The alloy composition of

the powder can be selected based on the mechanical performance desired in the material. As discussed in the literature, a range of titanium aluminide alloys exist which exhibit a range of mechanical properties for the desired applications. In the present study, two alloy compositions namely Ti-50%Al, and Ti-48%Al-2%Nb-2%Cr were selected as discussed in chapters II, and III respectively.

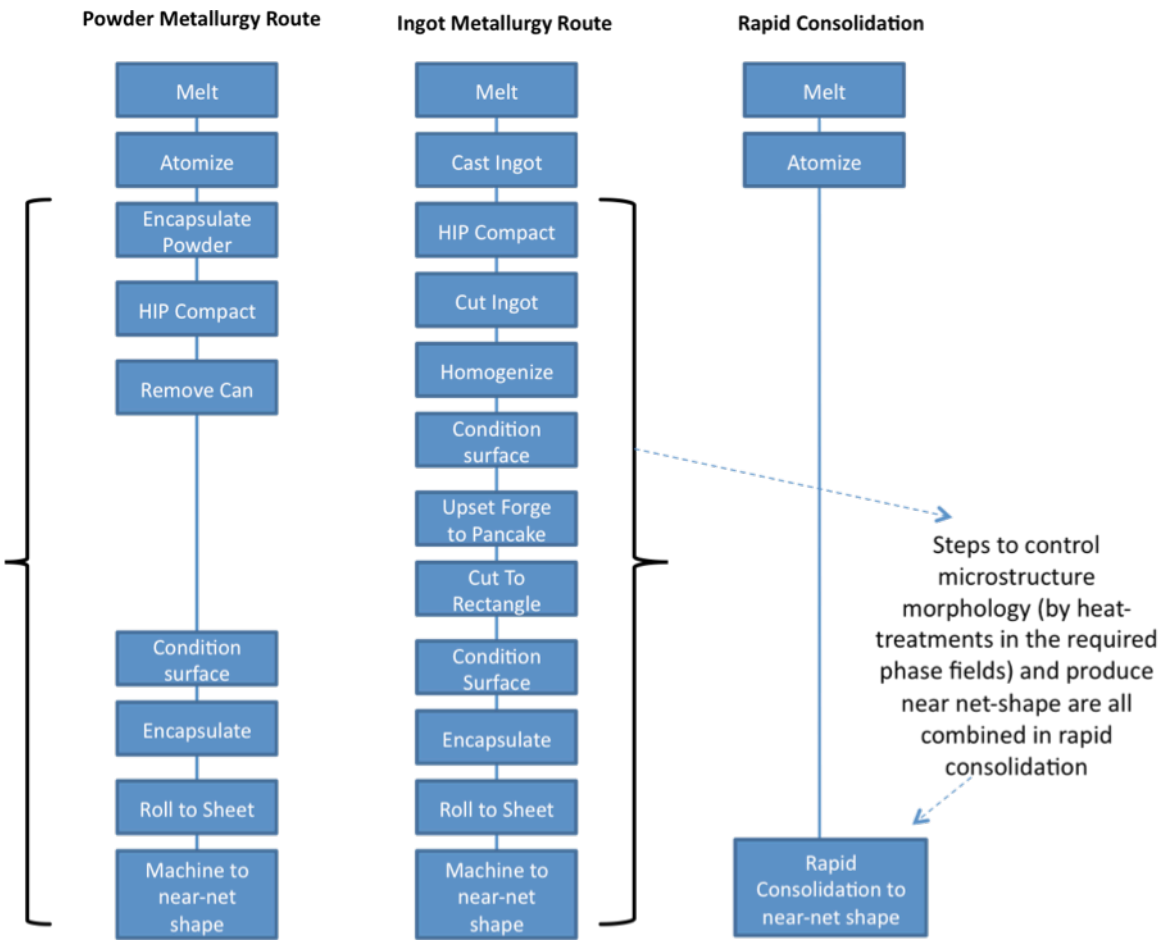

Figure 15: Rapid consolidation v. State-of-the-art in TiAl near-net shape manufacturing

The average powder particle size of the powder can be selected to be in the micrometer range or sub-micrometer range. The micrometer range powders are readily

available from commercial vendors, while the sub-micrometer range powders can be synthesized by ball-milling the micrometer range powders as discussed in chapter IV.

In the present study a particulate reinforcement for titanium aluminide was selected in TiB. The reinforcement was added in the TiAl matrix by blending together the powders of the matrix and composite. Once, a homogeneous blend was achieved, the blend was rapidly consolidated to produce a reinforced TiAl matrix as discussed in chapter V.

Consolidation Conditions

The consolidation conditions can be selected with the following three main control variables: 1) Phase field (Temperature), 2) cooling rate, and 3) pulsing. The phase field selection in general is based on alloy composition and temperature. Since, the alloy composition is selected during the powder design process, the temperature is the main control variable here. The selection of phase field governs the microstructure morphology in the consolidated part, which in turn governs the mechanical performance as discussed in chapters II, and III.

The cooling rate employed after the consolidation governs the phase composition of the consolidated part. An accelerated cooling rate aids in controlling the amount of Ti_3Al phase as discussed in chapter II. Finally, the pulsing process employed before reaching the consolidation temperature in the P2C process aids in enhancing diffusion during the consolidation process as discussed in chapter II.

The illustration below in Figure 16 is a TiAl design road-map, which was developed in the present study. More choices in control variables such as alloy composition can be added based on the availability of such powder compositions.

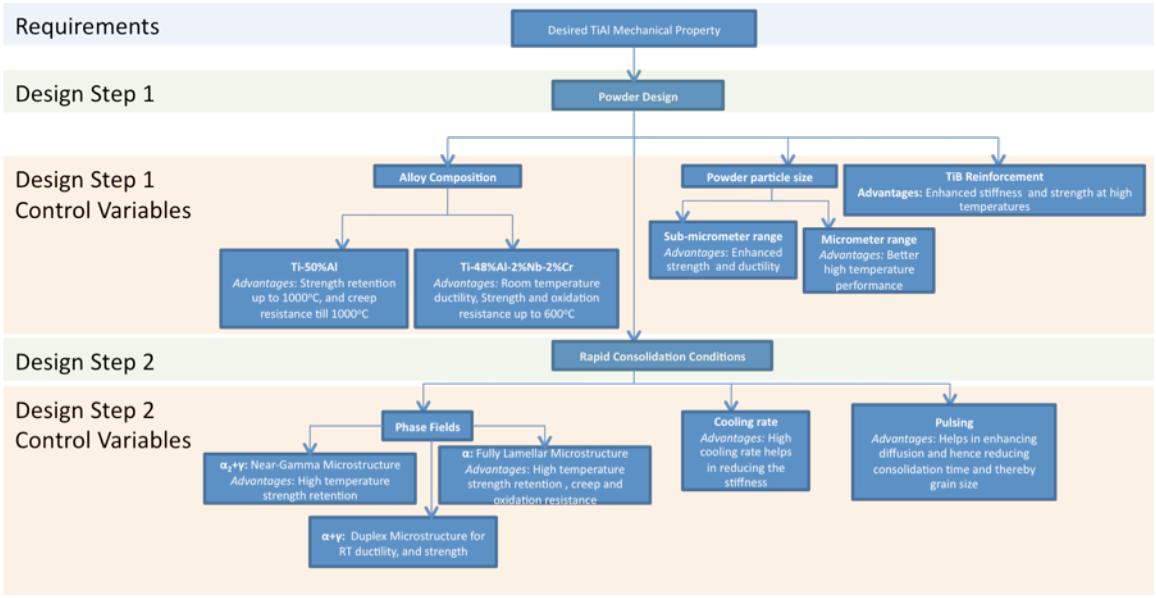

Figure 16: Road-map of TiAl design process developed in present study

The design process developed in present study (Figure 16) was based on the experimental results of the samples consolidated in Table 5 as shown below. The mapping of the design process in Figure 16 to all the consolidated samples is shown in Table 5.

Table 5: TiAl sample consolidation in present study

Sample ID	Alloy Composition (at%)	Average Powder Particle Size (μm)	TiB Reinforce-ment	Consolidation Phase Field	Cooling rate (K/min)	Expected Microstructure	Expected Mechanical Performance Highlights
S1	Ti-50Al	10	No	α+γ	60	Near-Gamma/Duplex	High temperature strength retention
S2	Ti-50Al	10	No	α_2+γ	60	Near-Gamma	High temperature strength retention
S3*	Ti-50Al	10	No	α_2+γ	60	Near-Gamma	High temperature strength retention
S4	Ti-50Al	10	No	α+γ	60	Near-Gamma/Duplex	High temperature strength retention
S5*	Ti-50Al	10	No	α+γ	60	Near-Gamma/Duplex	High temperature strength retention
S6	Ti-50Al	10	No	α	60	Fully Lamellar	High temperature strength retention, oxidation and creep resistance
S7	Ti-50Al	1.48	No	α_2+γ	60	Near-Gamma	High strength
S8	Ti-48Al-2Nb-2Cr	-	No	α	60	Fully Lamellar	High strength
T1	Ti-50Al	10	No	α_2+γ	200	Near-Gamma	High temperature strength retention
T2	Ti-50Al	10	No	α_2+γ	60	Near-Gamma	High temperature strength retention
T3	Ti-48Al-2Nb-2Cr	10	No	α+γ	60	Duplex	High strength, ductility, and oxidation resistance
T4	Ti-48Al-2Nb-2Cr	10	No	α+γ	60	Fully Lamellar	High strength, ductility, creep, and oxidation resistance
M1	Ti-48Al-2Nb-2Cr	10	Yes	α+γ	60	Duplex	High modulus, high temperature strength and, modulus retention, creep, and oxidation resistance
M2	Ti-48Al-2Nb-2Cr	10	Yes	α+γ	60	Duplex	High modulus, high temperature strength and, modulus retention, creep, and oxidation resistance

** Indicates No Pulsing*

Apart from the novel manufacturing technique described above, the original contributions resulting from the present study are as follows:

1. Micron-sized Ti-50%Al (at%) powders were consolidated by P2C to produce fully dense near-net shape parts in the form of ¼" thick, 1" diameter discs and 3" x 2.5" tiles. The microstructure of the consolidated Ti-50%Al parts revealed minimal grain growth and thereby exhibited enhanced mechanical performance. Parameters to consolidate Ti-50%Al by P2C were chosen using the Ti-Al binary phase diagram. The three characteristic microstructures in Ti-50%Al produced include Near-Gamma microstructures, Duplex microstructures and Fully Lamellar microstructures. A correlation between the consolidation parameters and microstructural morphology was established. The mechanical properties of Ti-50%Al samples were characterized and a relationship between the microstructural morphology and mechanical properties was established.

2. The presence of impurities in powders usually creates a diffusion barrier during consolidation process. Hence, a pulsed DC voltage was applied to the powder compact during the consolidation of Ti-50%Al. The pulsing of the voltage through the powder compact charges the powder particles relative to each other and leads to generation of sparks or plasma. The formation of plasma removes the diffusion barrier that comprises of oxides and other contaminants. This was evident for samples consolidated at 1000^{o}C. For samples consolidated at higher temperatures (>1200^{o}C), the effect of pulsing was not apparent.

3. The effect of cooling rate (during the cooling cycle of the consolidation process) on the mechanical properties of Ti-50%Al was examined. Rapid cooling from the consolidation temperature freezes the high temperature phase (α_2 phase) in the consolidated sample. This in turn increases the α_2 volume fraction. The increase in the α_2 volume fraction decreases the stiffness of the material.

4. The mechanical behavior of the consolidated Ti-50%Al parts was characterized at temperatures up to 1000^{o}C. Ti-50%Al samples exhibited increase in flexure strength up to 400^{o}C due to microstructure refinement. The bending modulus was found to increase with increase in temperature up to 600^{o}C due to phase transformation of the $\alpha_2+\gamma$ metastable phase in to pure γ phase. Exposure to air at high temperatures resulted in deterioration of the flexure strength of Ti-50%Al samples by 10%.

5. Small additions of Nb and Cr (in the order of 2at%) along with a small decrease in Aluminum concentration (from 50at% to 48at%) resulted in a significant change in the mechanical behavior of the consolidated titanium aluminide parts. Consolidation of titanium aluminide powders with a composition of Ti-48%Al-2%Nb-2%Cr resulted in formation of titanium aluminide parts with better room temperature ductility, strength and oxidation resistance.

6. Attrition milling of Ti-50%Al powders resulted in the reduction of powder particle size by 60%. Consolidation of the milled Ti-50%Al powders resulted in Ti-50%Al parts with grain size in the sub-micrometer range. The decrease in grain size from micrometer range to sub-micrometer range resulted in a marked improvement in terms of flexure stress and elongation.

7. A metal matrix composite with a matrix composed of Ti-48%Al-2%Nb-2%Cr (at%) reinforced with TiB was developed. The composite was synthesized by blending TiB_2 and Ti-48%Al-2%Nb-2%Cr powders in an attrition mill. The powder mixture was then rapidly consolidated by P2C to form a Ti-48%Al-2%Nb-2%Cr matrix composite reinforced with elongated TiB plates. The thermodynamic equilibrium between Ti and TiB led to the transformation of TiB_2 powders into TiB during consolidation.

Chapter 2: Characterization of Rapidly Consolidated Ti-50% Al

2.1 Introduction

Dual phase gamma titanium aluminides with α_2 (Ti_3Al) and γ (TiAl) phases have attracted substantial attention in the last two decades for their potential application in high temperature thermal protection and propulsion systems [1; 9; 101]. Gamma titanium aluminides containing around 50% (at%) Aluminum have been found to exist with two types of phases [17; 19; 29; 102-105]. First is the pure gamma phase, which exists in gamma titanium aluminides with an aluminum content of more than 50% (at%). The second is the dual phase, which exists for titanium aluminides with an aluminum concentration less than 50% (at%). The dual phase is composed of the α_2 (Ti_3Al) and γ (TiAl) phases.

The pure gamma phase has been found to exhibit good oxidation resistance and good strength and modulus retention at high temperatures. But it has been found to display no ductility [19; 102; 103]. As shown in the Ti-Al binary phase diagram [20] in Figure 17, the pure gamma phase for gamma titanium aluminides (>50%Al concentration) exists even at high temperatures. This leaves no room for thermo-mechanical treatments, which in turn can augment the phase and microstructural characteristics of the material, and therefore may impact its mechanical properties in a favorable manner.

However, the dual phase gamma titanium aluminide has been found to respond favorably to thermo-mechanical treatments [31; 36; 37; 106; 107]. Thermo-mechanical treatments have produced four characteristic microstructures namely 1) Near gamma, 2) Duplex, 3) Nearly-Lamellar, and 4) Fully Lamellar in dual phase gamma titanium aluminides [37; 106].

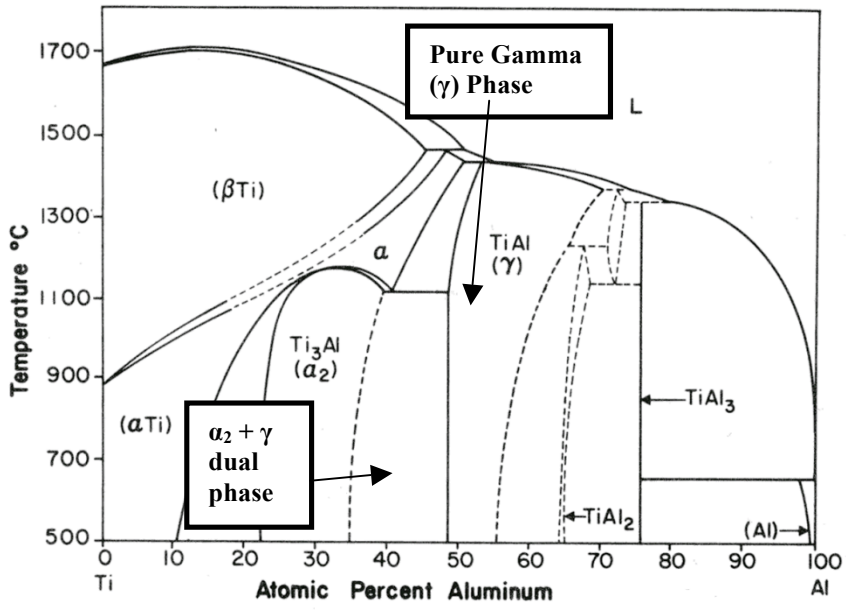

Figure 17: Ti-Al binary phase diagram [20].

Confirming the Hall-Petch relationship, grain size has been found to be inversely proportional to the strength of gamma titanium aluminides [12]. Controlling grain growth in the manufacturing process of gamma titanium aluminides (γ-TiAl) could lead to high strength γ-TiAl alloys.

In the present study, gamma titanium aluminides with 50% Al (at%) were consolidated by a rapid consolidation process, Plasma Pressure Compaction (P2C) to control grain growth during consolidation and characterized for their microstructure and mechanical properties. The P2C rapid consolidation was conducted at a range of

temperatures as shown in a section of the phase diagram of the Ti-Al system in Figure 18. These consolidation temperatures correspond to the $\alpha_2 + \gamma$, $\alpha + \gamma$, and pure α phase fields. The consolidation temperatures were chosen to control the microstructure in order to obtain the best mechanical properties. The aim was to consolidate Ti-50%Al to produce the characteristic microstructures of dual phase gamma titanium aluminides with minimal grain growth. The mechanical properties of the consolidated samples were characterized and correlated to the microstructures.

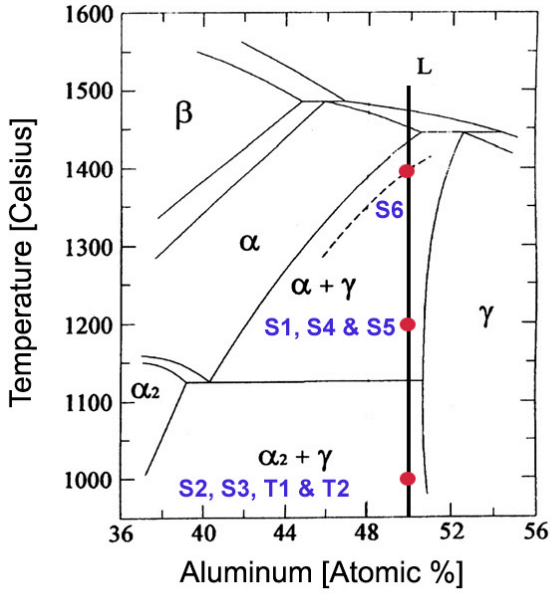

Figure 18: Partial Ti-Al binary phase diagram near the stoichiometric γ-TiAl composition [108].

2.2 Experimental Procedure

-325 mesh (<45 μm) Ti-50%Al powders were procured from CERAC, Milwaukee, WI and ESPI, Inc., Ashland, OR. The as-received powders were characterized by X-ray

diffraction and scanning electron microscopy (SEM) for their composition and microstructure, respectively. The powders were then consolidated by the P2C technique.

2.2.1 Plasma Pressure Compaction

For consolidation, γ-TiAl powders were contained in a graphite die with plungers inserted on both sides. This assembly was then placed between water-cooled electrodes and the chamber containing this assembly was evacuated. The lower electrode was raised using a hydraulic cylinder to hold the entire assembly together in compression and provide a path for current flow. When sufficient inter-particle contact was established by applying uniaxial pressure, pulsed DC voltage was applied through the powder compact using a full-wave-rectified power supply.

Pulsed electrical power was applied with high current at an adequate voltage. This leads to charge build up at inter-particle gaps. This causes one particle to be charged negatively with respect to another particle that is in contact with it. As the charge accumulates, the voltage difference becomes sufficiently large to generate sparks that trigger an ionization process. The ions move towards the negatively charged particles while the electrons move toward the positively charged particles. The ionization process occurs in the form of sparks or plasma generation depending on the energy level at the inter-particle gap. The formation of plasma removes oxides and other contaminants, which form a diffusion barrier in the consolidation process. As a result, particle re-arrangement and diffusion is enhanced. After pulsing, direct current was applied through the powder compact resulting in Joule heating as shown in Figure 19a.

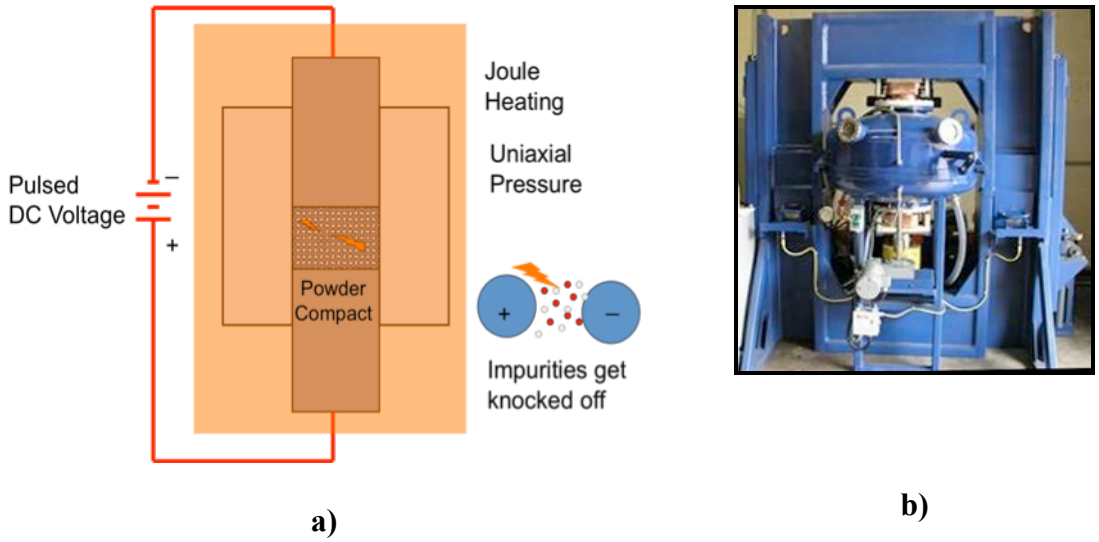

Figure 19: Plasma pressure compaction process (a) and set-up (b)

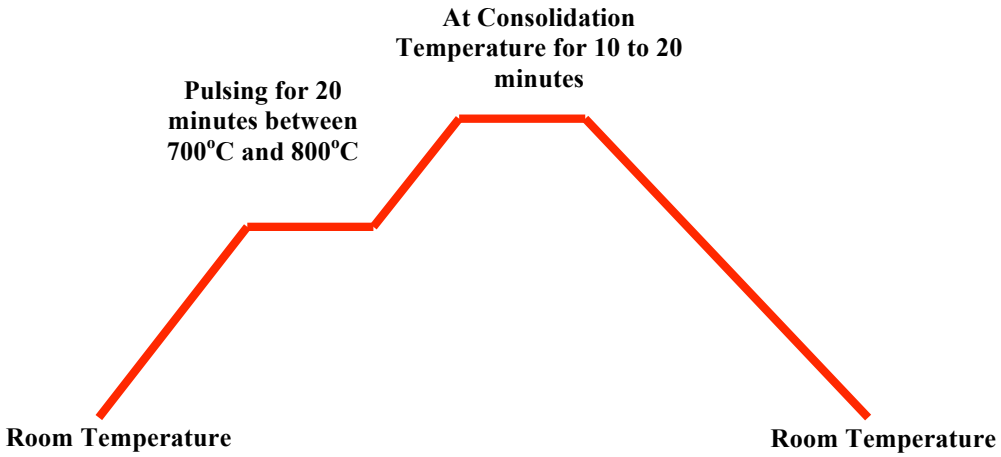

Figure 20: Consolidation profile for plasma pressure compaction

Figure 20 shows the consolidation profile for the P2C process. Pulsing was performed between 700°C and 800°C for about 20 minutes.

2.2.2 Microscopy

The consolidated samples were sectioned and metallographically polished to 1 μm diamond finish. They were subsequently etched using Kroll's reagent. Their microstructure was characterized via optical microscopy, Scanning Electron Microscopy (SEM) and Energy Dispersive Spectroscopy (EDS). The SEM and optical micrographs were taken in an orientation perpendicular to the direction of compaction.

2.2.3 Mechanical Tests

The mechanical properties of the consolidated specimens were characterized using four-point bending tests. A self-aligning silicon carbide four-point bending fixture was designed according to ASTM standard C1161 [109] with an outer-span of 20 mm and an inner-span of 10 mm. Consolidated samples were machined with chamfered edges to a dimension of 25 mm x 1.5 mm x 2.0 mm. Samples with dimension of 3 mm x 4 mm x 25 mm with a 60 degree chevron notch were also tested according to ASTM standard C1421 in the four-point bending set-up to measure fracture toughness. All tests were conducted at a strain rate of 0.75×10^{-4} in a Material Testing Systems (MTS) model 810 machine. The four-point bend tests were conducted at temperatures up to $950^{o}C$. The high temperature tests were conducted in air and vacuum (10^{-5} Pa). Test samples were loaded in the four-point bend test fixture such that the resultant tensile and compressive stresses were in the direction perpendicular to that of the direction of the compaction. Micro-hardness of the consolidated samples was obtained on polished specimens using a diamond Vickers indent under a load of 1000 grams with a dwell time of 15 seconds.

For four-point bend tests performed at room temperature, bend bars were mounted with strain gages on the side under pure tension (Figure 21). The strain data along with load and displacement data was used to calculate the elastic modulus of the material, as well as the elongation and flexural strength. The stress (σ) along the span and the thickness of the bend bar was calculated using the flexure formula [110].

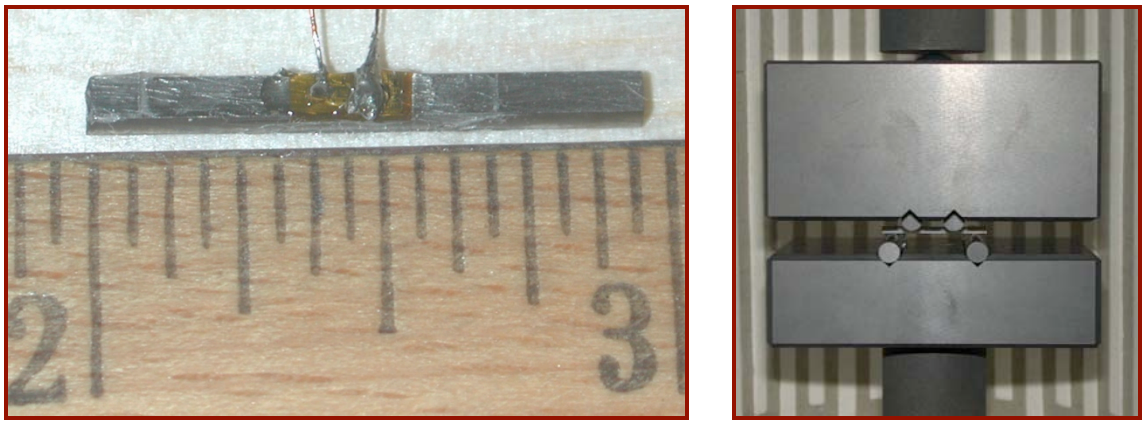

a) **b)**

Figure 21: Bend bar mounted with strain gage (a) and loaded in a four-point bending test fixture (b)

$$\sigma = \frac{Mc}{I} \qquad (1)$$

Where, M is the moment along the span of the bend bar and stays constant along the inner-span of the four-point bending fixture. I is the moment of inertia along the width of the bend bar and c is the distance along the thickness from the neutral axis. Assuming that the material is isotropic, homogeneous and linearly elastic with identical moduli in tension and compression, the neutral axis was placed at the vertical center of the bend bar [109; 110].

To ensure the accuracy of the four-point bending test data, "control" samples prepared from AD998 Alumina obtained from CoorsTek, Golden, CO., were also tested. Figure 22 shows the four-point bending test data for twelve Alumina "control" samples. The average elastic modulus and flexure strength calculated from the data in Figure 22 was found to be 326.23 GPa and 350.45 MPa, respectively. These values are in close agreement to the properties listed by CoorsTek, Golden, CO [111] and validated the four-point bending test procedure used in this study.

For high temperature four-point bend tests, strain gages could not be mounted on the bend bars due to temperature limits on the strain gages themselves. In this case, instead of elastic modulus in tension the elastic modulus in bending was calculated using the load and displacement data collected from the built-in MTS 810 frame load cell and displacement sensor. The derivation of the equation used to calculate the elastic modulus in bending is shown in Appendix A.

The high temperature four-point bending tests were performed in both air and vacuum. Figure 23 shows the four-point bending test set-up for high temperature tests in air. For high temperature tests in vacuum, the four-point bending test set-up was enclosed in a retort with a bellows assembly. The bellows assembly was used on the top and bottom of the retort to seal the loading rods as shown in Figure 24. A diffusion vacuum pump was used to obtain vacuum in the range of 10^{-5} Pa.

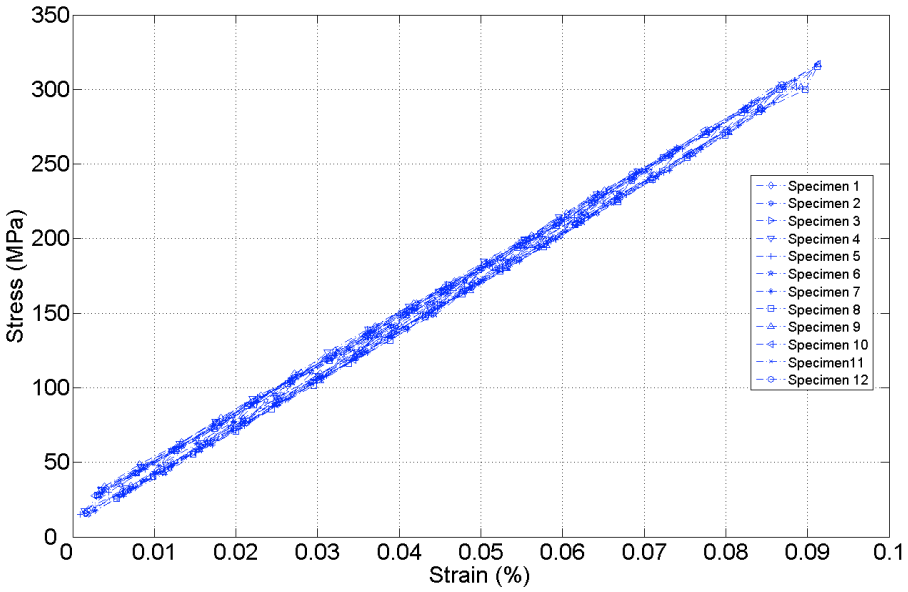

Figure 22: Four-point bending test data for Alumina "control" samples from CoorsTek, Golden, CO.

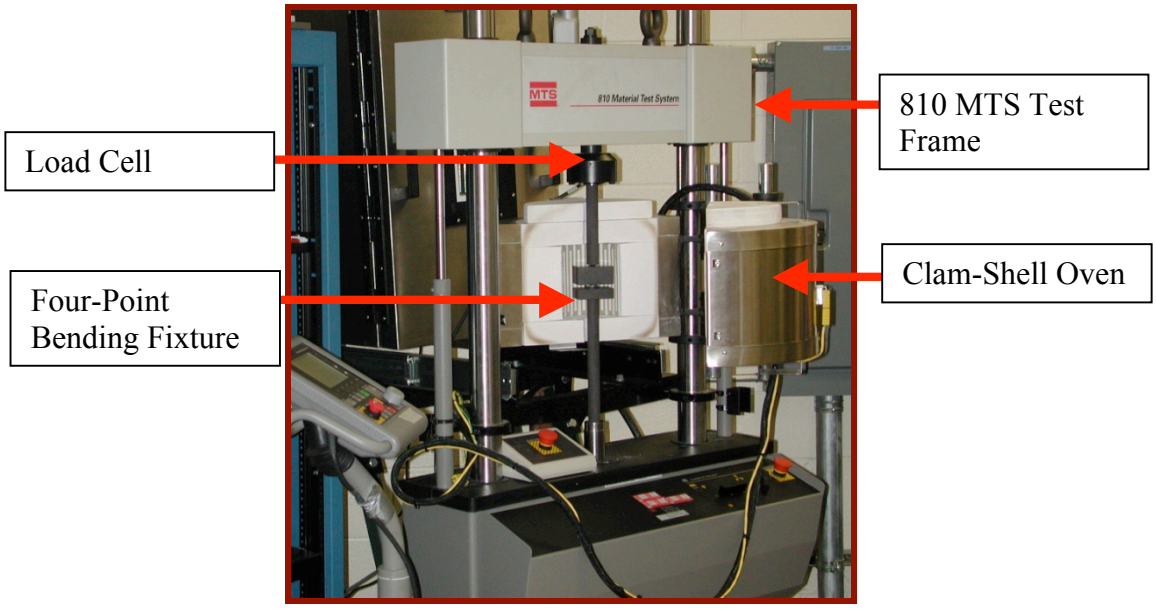

Figure 23: Four-point bending set-up in a high temperature clam-shell oven

The four-point bending test set-up was also used to calculate the fracture toughness of the material. This was done by using a bend bar with a chevron notch in the center. The load and the displacement data collected during the test was used to calculate the fracture toughness. Alumina AD-998 "control" samples from CoorsTek, Golden, CO., were again used to verify this test. The average fracture toughness for ten alumina "control" samples was found to be 3.45 MPa $m^{1/2}$, which was in close agreement to the values listed by CoorsTek.

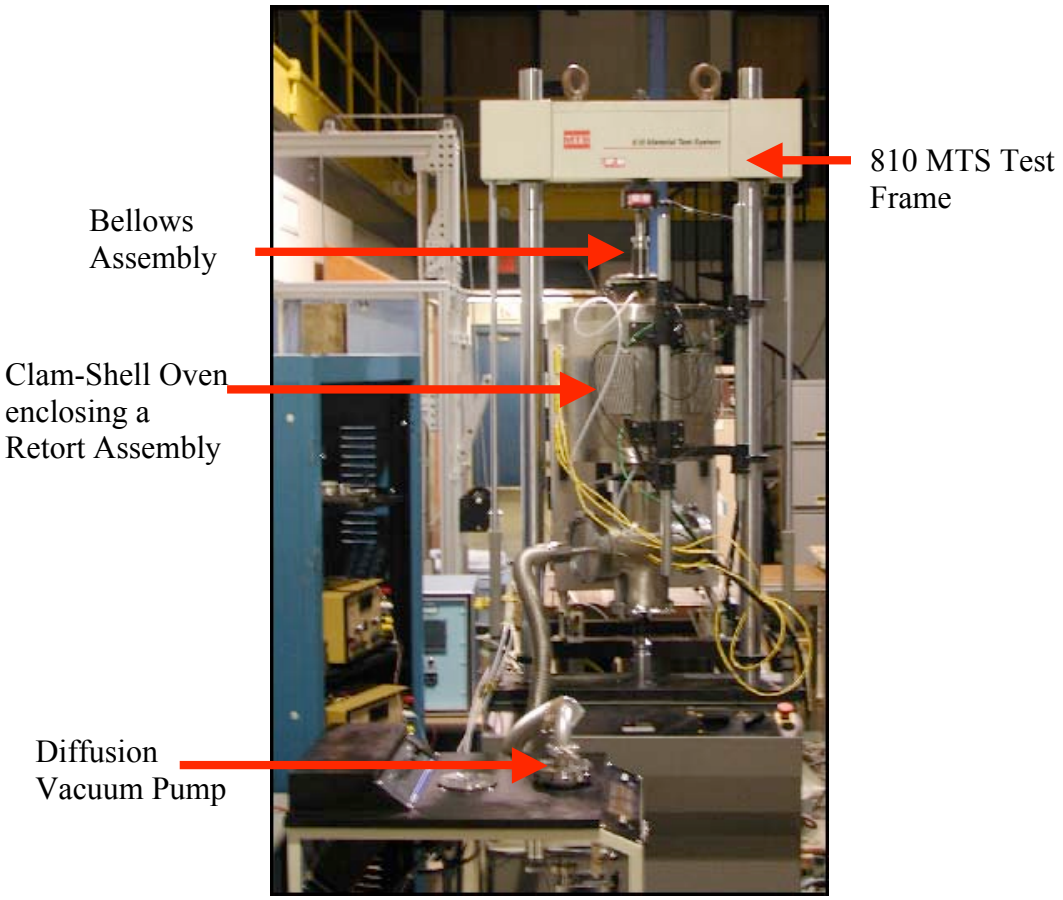

High temperature four-point bending test set-up in vacuum

2.3 Characterization of As-Received Powders

-325 mesh (<45 μm) powders procured from CERAC, Milwaukee, WI., were characterized via SEM, and X-ray diffraction.

2.3.1 X-Ray Diffraction

Figure 23 shows the X-ray diffraction (XRD) pattern for the as-received powders from CERAC, Milwaukee, WI. The standard diffraction peak positions of the γ-TiAl and α_2-Ti_3Al with relative intensity represented by the height of the vertical lines are also plotted in Figure 25. The XRD results indicated the presence of γ-TiAl and α_2-Ti_3Al phases and confirmed that the powder was dual phase Titanium Aluminide.

2.3.2 Scanning Electron Microscopy

Figure 26 shows the SEM micrographs of as-received powders from CERAC, Milwaukee, WI. The micrographs suggest powder particle size under 45 μm. Further, Energy Dispersive Spectroscopy (EDS) revealed the composition of the as-received powders to be in the two-phase (α_2+γ) field based on the Ti-Al binary phase diagram.

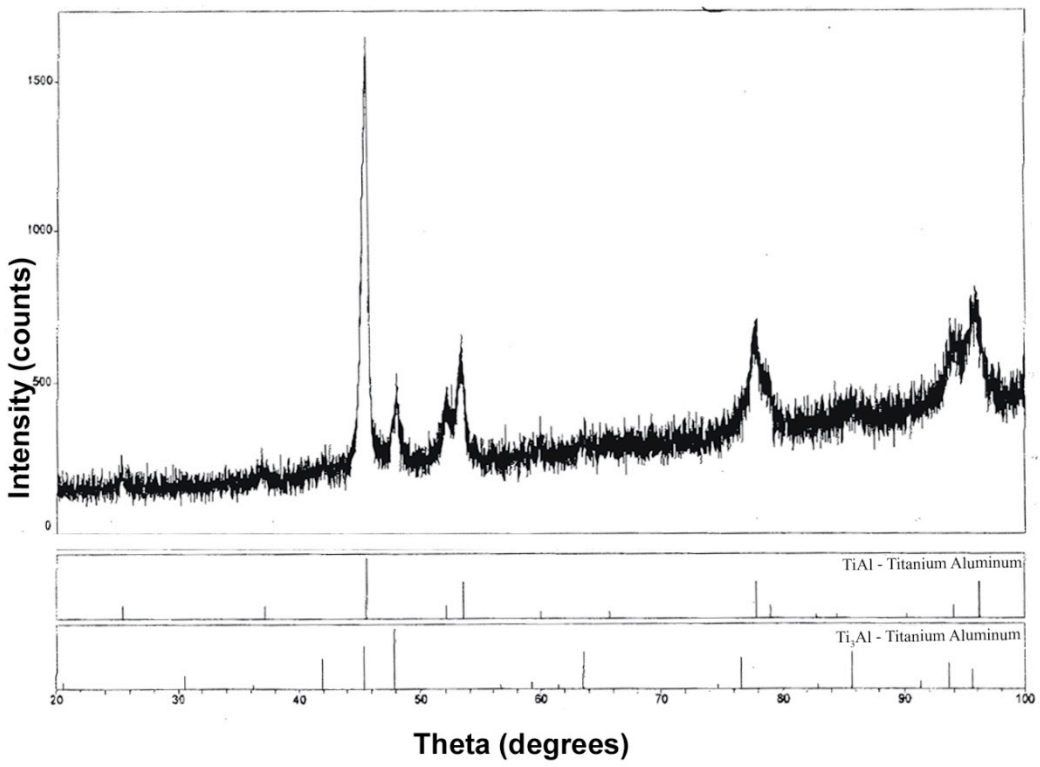

Figure 25: X-ray diffraction results of as-received Ti-50%Al powders from CERAC, Milwaukee, WI.

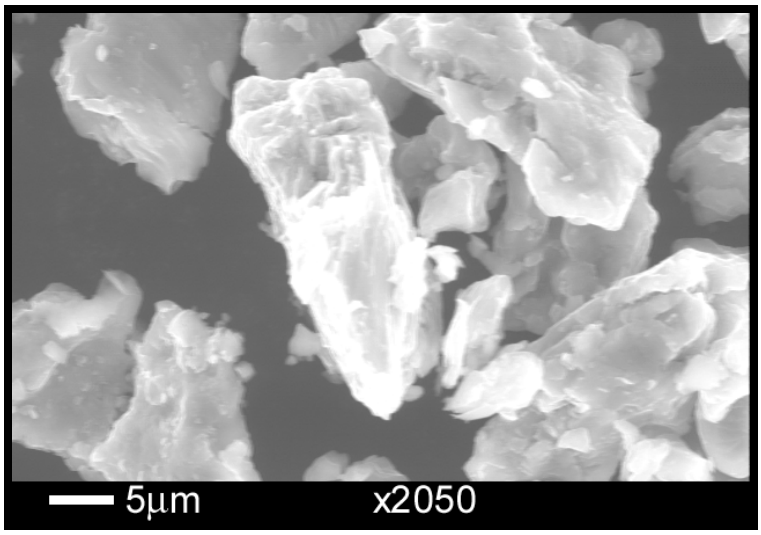

Figure 26: SEM of as-received Ti-50%Al powders from CERAC, Milwaukee, WI.

2.4 Consolidation of Ti-50% Al

2.4.1 Consolidation of Ti-50% Al Discs

-325 mesh (<45 μm) Ti-50%Al powders procured form CERAC, Milwauke, WI and ESPI, Inc., Ashland, OR were consolidated in to 1-inch diameter discs as shown in Figure 27. Both the discs and tiles were ¼" thick. The discs were consolidated at temperatures in the $\alpha_2 + \gamma$, $\alpha + \gamma$ and close to pure α phase fields. The consolidation pressure was set to be in the range of 54 MPa to 130 MPa. The consolidation conditions of the disc samples are listed in Table 6. For comparison purposes, two of the discs were consolidated without the pulsing process. All the phase field temperatures were determined from the binary phase diagram in Figure 18. The $\alpha_2 + \gamma$ phase field boundary was determined to be close to 1200°C, while the $\alpha + \gamma$ phase field boundary or the α-transus temperature (T_α) of the Ti-50Al alloy was determined to be close to 1435°C. Consolidation was conducted in vacuum at temperatures ranging from 1000 °C (T_α - 435°C) to 1400 °C (T_α - 35°C) as marked in Figure 18.

2.4.2 Consolidation of Ti-50% Al Tiles

Tiles measuring 2.3" x 3" x 0.25" were consolidated from powders procured from ESPI, Inc., Ashland, OR as shown in Figure 28. These tiles were consolidated for comparison to one-inch diameter discs. The tiles were consolidated in the $\alpha_2 + \gamma$ phase field under consolidation pressure of 30 MPa. During the P2C process, different cooling rates were used to cool the tiles from consolidation temperature to room temperature. This was achieved by controlling the DC voltage applied to the sample. The cooling rate used for

P2C consolidation of titanium aluminide samples (including disc samples) was set to 60K/min. But in the consolidation of the first tile, the cooling rate was accelerated to 200K/min. The consolidation conditions for both the tiles are listed in Table 7.

Table 6: Matrix of P2C consolidated Ti-50%Al one-inch diameter disc samples

Sample ID	Powder Type	Consolidation Time (Minutes)	Consolidaton Pressure (MPa)	Temperature (Celsius)	P2C Pulsing
S1	CERAC	20	100	T_α - 235 (1200)	Yes
S2	ESPI	10	54	T_α - 435 (1000)	Yes
S3	ESPI	10	54	T_α - 435 (1000)	No
S4	ESPI	10	54	T_α - 235 (1200)	Yes
S5	ESPI	10	54	T_α - 235 (1200)	No
S6	ESPI	20	130	T_α - 35 (1400)	Yes

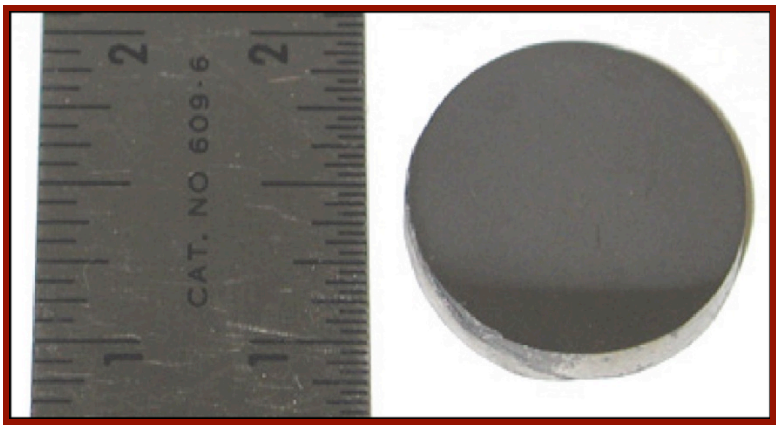

Figure 27: P2C consolidated Ti-50%Al disc

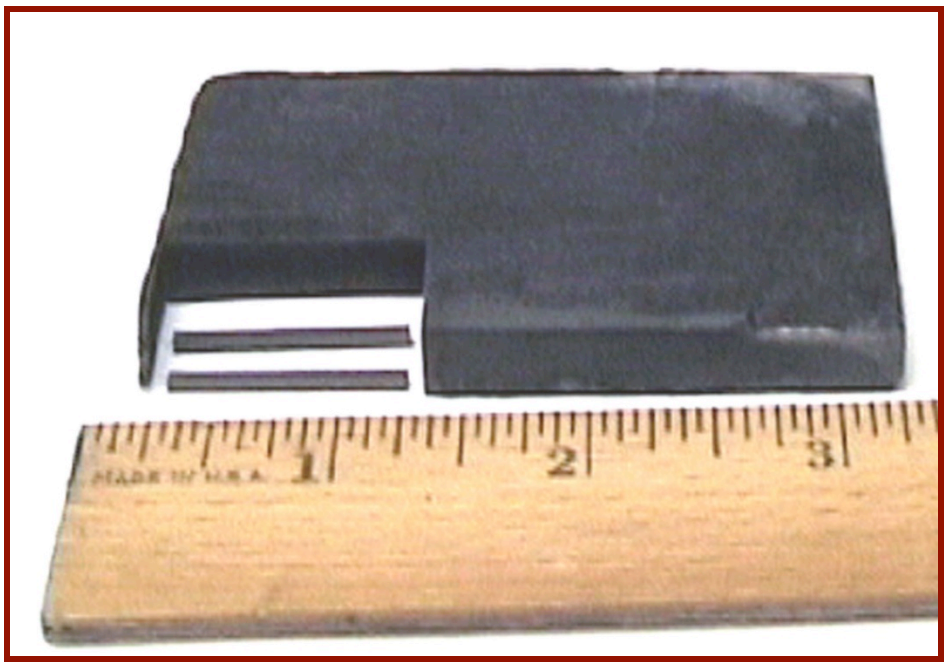

Figure 28: P2C consolidated Ti-50%Al tile

Table 7: P2C consolidation conditions for Ti-50%Al tiles

Sample ID	Powder Type	Consolidation Time (Minutes)	Consolidation Pressure (MPa)	Temperature (Celsius)	P2C Pulsing	Cooling rate (K/min)
T1	ESPI	15	30	T_α - 435 (1000)	Yes	200
T2	ESPI	20	30	T_α - 435 (1000)	Yes	60

2.5 Characterization of Consolidated Samples

2.5.1 Density

The density of the consolidated samples was determined by Archimede's technique. The density of the consolidated disc specimens was found to be in the range of 3.8 – 4gm/cm^3

as shown in Figure 29. The density of γ-TiAl phase is 3.76 gm/cm^3, while that of α_2-Ti_3Al phase is 4.1 gm/cm^3. The density values of the disc specimens are between the theoretical values of γ-TiAl and α_2-Ti_3Al.

The density of the tile specimens was found to be lower than the density of both γ (TiAl) and α_2 (Ti_3Al) phases. This indicates that the tile specimens may not have been fully densified. This was further confirmed by microscopy.

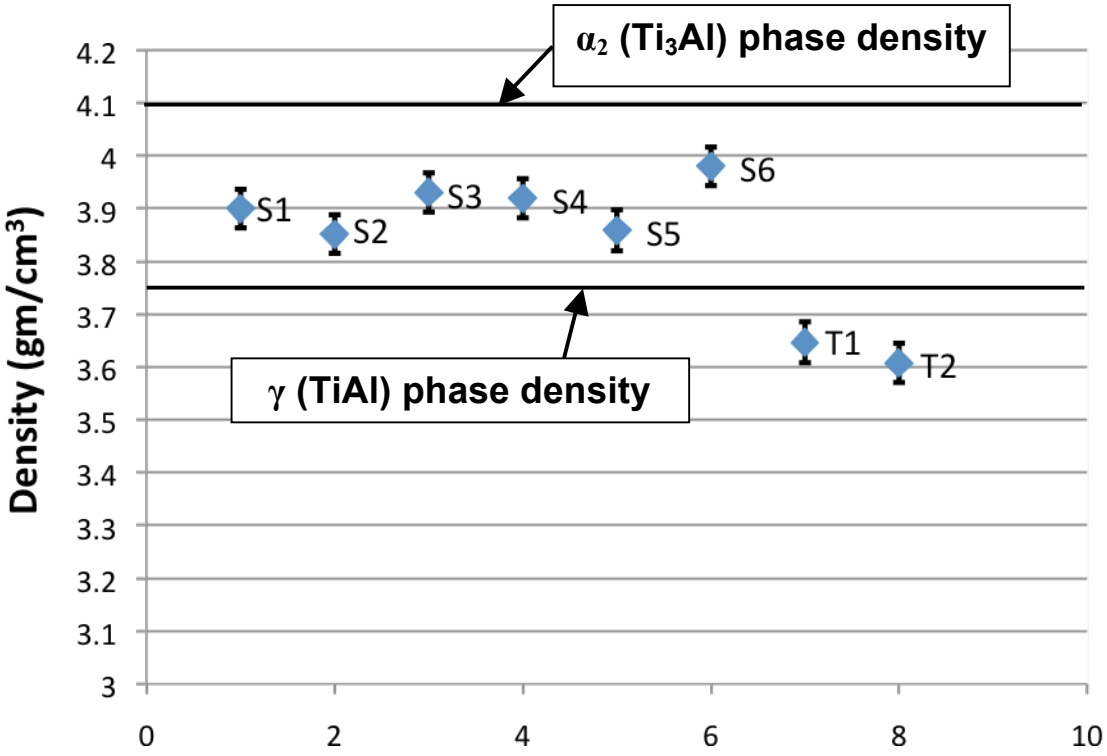

Figure 29: Density of P2C consolidated Ti-50%Al samples

2.5.2 X-Ray Diffraction

X-ray diffraction (XRD) analysis was performed on sample S1. This sample was consolidated from powders procured from CERAC, Milwaukee, WI. The consolidated

sample S1 showed peaks similar to that of the as-received powders indicating the presence of both γ (TiAl) and α_2 (Ti_3Al) phases. The low noise in Figure 30 indicates more crystallinity as compared to as-received powders. The XRD analysis of the consolidated sample confirms that the P2C process did not impart any phase changes during the consolidation process.

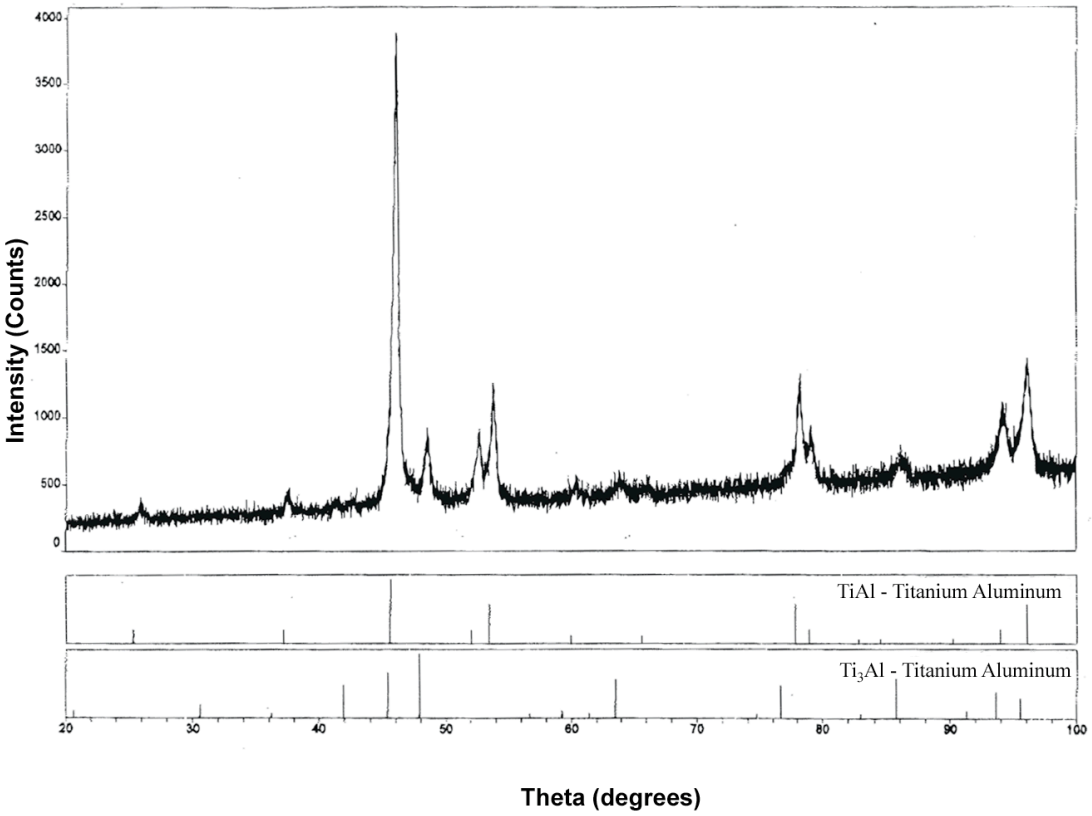

Figure 30: X-ray diffraction of consolidated P2C sample S1

2.5.3 Microscopy

The microstructure of the P2C consolidated samples was characterized by optical microscopy, Scanning Electron Microscopy (SEM) and Electron Dispersive Spectroscopy (EDS).

The optical micrographs of sample S1 is shown in Figure 31. The grain size of sample S1 was determined by the line-intercept method. The average grain size was found to be 20 μm. The microstructure of sample S1 consisted of a mix of large and small grains with different characteristics for each. The characteristics of these grains were further analyzed by scanning electron microscopy and energy dispersive spectroscopy.

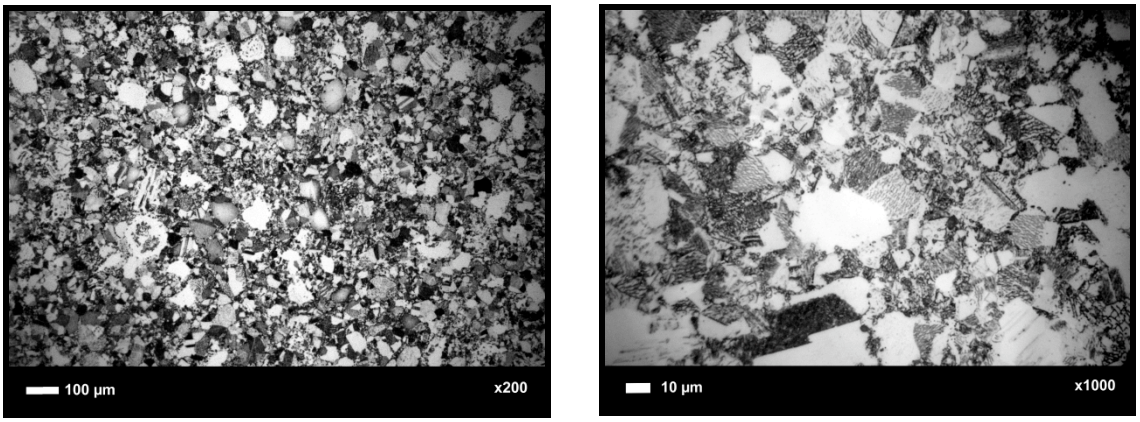

a) b)

Figure 31: Optical micrograph of P2C consolidated sample - S1

In order to view the microstructure of the P2C consolidated samples in more detail, SEM was performed on all the P2C consolidated samples listed in Table 1. With the help of energy dispersive spectroscopy further details about the composition were obtained.

Sample S1

Sample S1 was consolidated into 1-inch diameter discs using the powders procured from CERAC, Milwaukee, WI. The sample was consolidated at 1200^{o}C at a pressure of 100 MPa. The consolidation temperature was 235^{o}C below the α-transus

temperature (T_α) and 70^{o}C above the α+γ phase boundary temperature as shown in Figure 18. The SEM micrograph of sample S1 in Figure 32 and Figure 33 shows the presence of two different phases as seen by the color contrast.

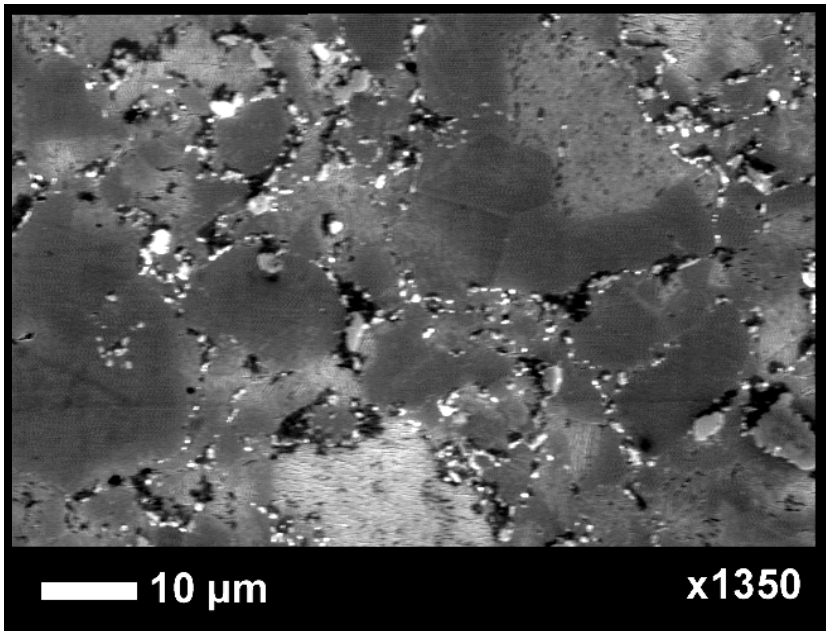

Figure 32. Scanning electron micrograph of consolidated P2C sample S1

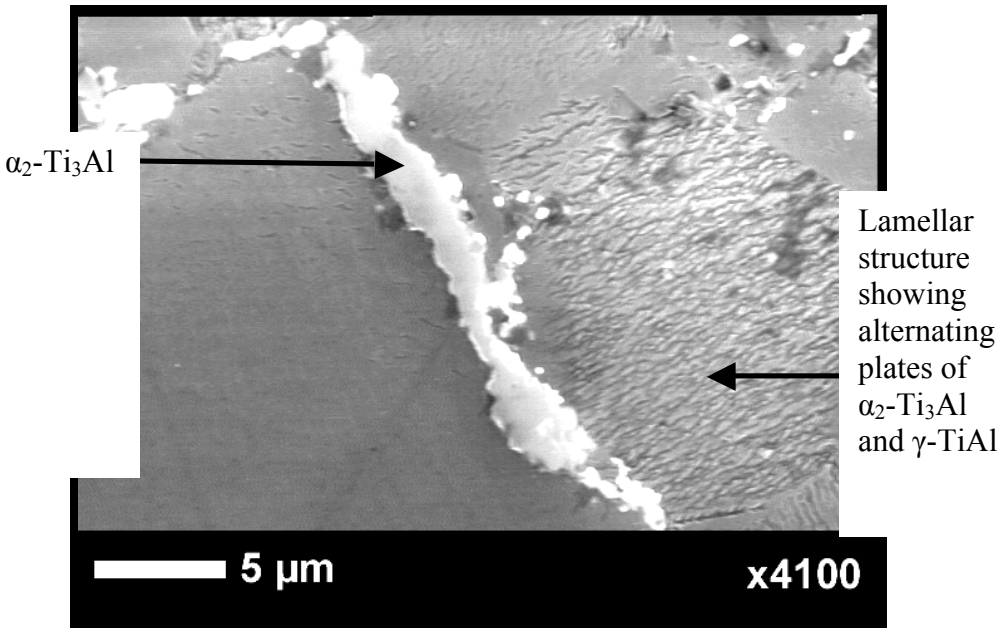

Figure 33: SEM micrograph of consolidated P2C sample S1 showing lamellar colonies

To determine the chemical composition of the different phases present in sample S1, energy dispersive spectroscopy (EDS) was performed. EDS revealed presence of γ (TiAl) phase as the dark phase and α_2 (Ti_3Al) phase as the lighter phase as shown in Figure 34. The α_2 (Ti_3Al) phase was further found to be segregated at the grain boundaries. The fine alternating dark and light structures in the grains in Figure 33 were determined by EDS to be alternating plates of α_2 (Ti_3Al) and γ (TiAl) phase. Hence, from literature [19; 31; 36; 103; 106] and the above observations, the microstructure was determined to be near gamma/Duplex. The microstructure consisted of large gamma grains, small equiaxed gamma grains and lamellar colonies. The EDS performed on Sample S1 also revealed pockets of high concentration of oxygen as indicated by the dark black areas in Figure 34.

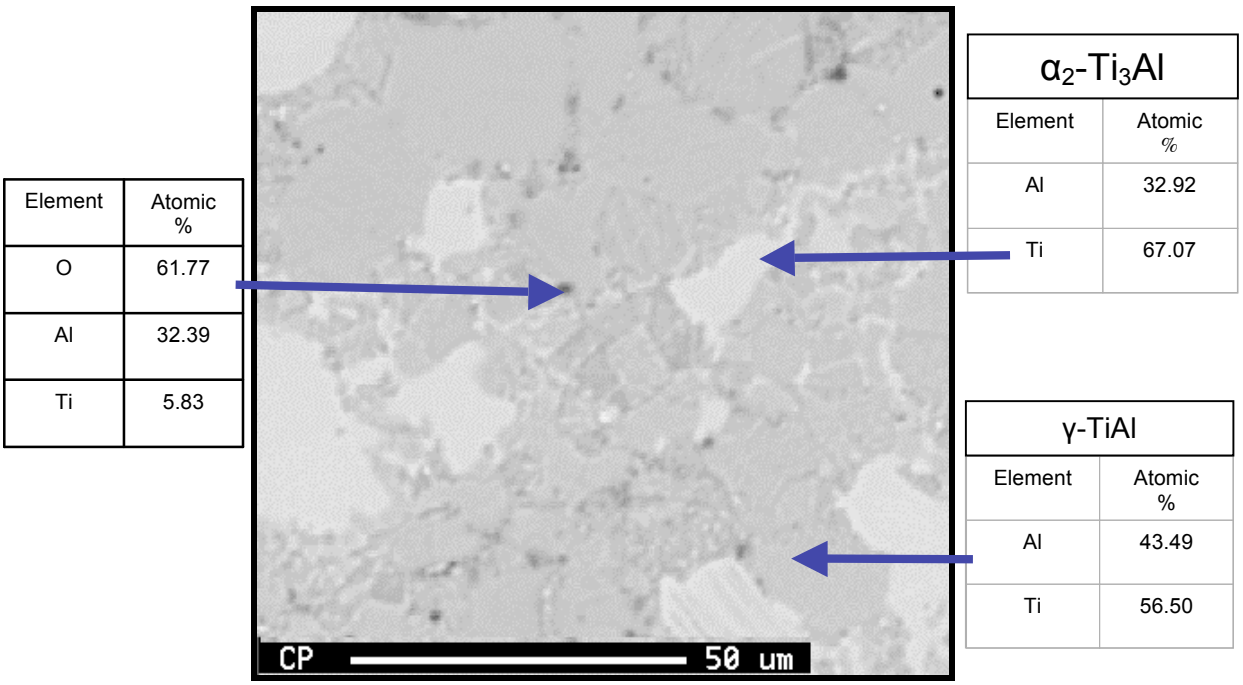

Figure 34: Energy dispersive spectroscopy of P2C consolidated sample S1

Five 1-inch diameter discs were consolidated from the powders procured from ESPI, Inc., Asland, Oregon. The consolidation parameters for these discs are listed in Table 6 and marked with Sample ID - S2, S3, S4, S5 and S6. All these samples were subsequently consolidated for their microstructure.

Samples S2 and S3

Samples S2 and S3 were consolidated from powders procured from ESPI, Inc., Ashland, Oregon. The powders were consolidated in to 1-inch diameter discs. The samples were consolidated at 1000^{o}C, 435^{o}C below the α-transus temperature and 130^{o}C below the α+γ phase boundary temperature. Before reaching the consolidation temperature, the powder

compact of sample S2 was subjected to a pulsed DC voltage for 20 minutes. SEM micrographs of sample S2 are shown in Figure 35 and 36.

Correlating the microstructure of S2 with its EDS analysis, it was found to consist of large and small gamma grains. The α_2 (Ti_3Al) phase was segregated at the grain boundaries. This is characteristic of a near gamma microstructure. The average grains size as determined from the line-intercept method was 10 μm. The dark black areas in the SEM micrographs of sample S2 was found to contain oxygen and carbon impurities.

Sample S3 was consolidated at same conditions as sample S2 except that the pulsing process was not applied during consolidation. The SEM micrographs of sample S3 (Figure 37 and Figure 38) exhibited similar characteristics to that of sample S2- except that EDS analysis of S3 indicated that it had a higher presence of carbon and oxygen content than sample S2. The average grain size of sample S3 was determined to be 10 μm, similar to sample S2.

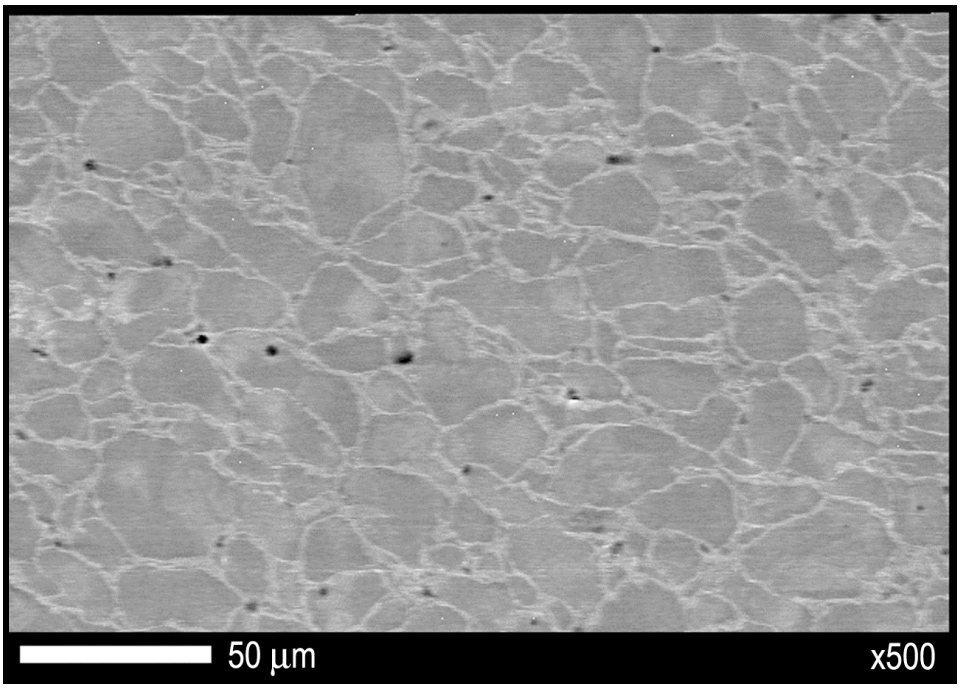

Figure 35: SEM of P2C consolidated sample S2

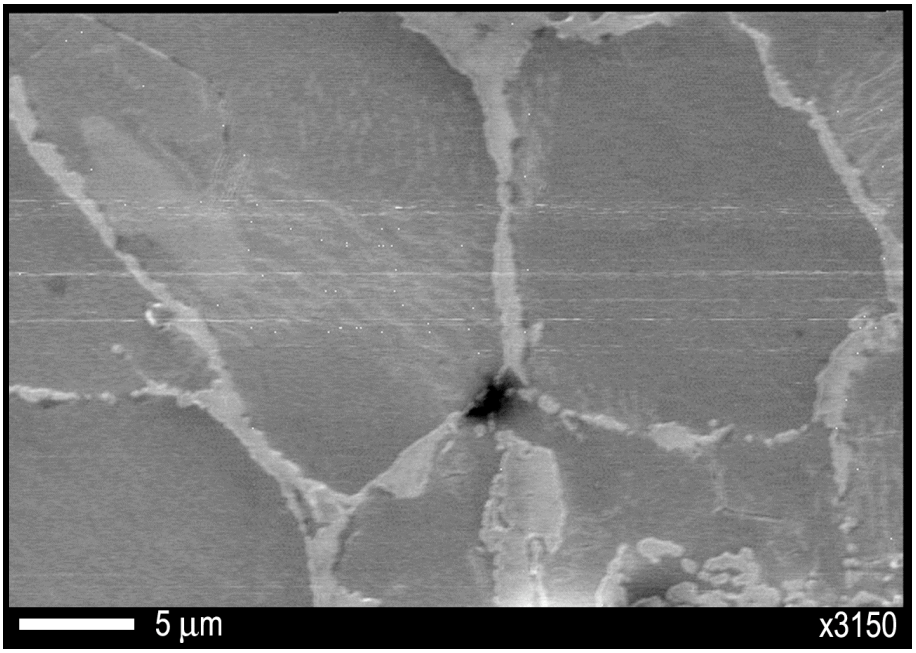

Figure 36: SEM of P2C consolidated sample S2 showing α_2 (Ti_3Al) phase segregated at the grain boundaries

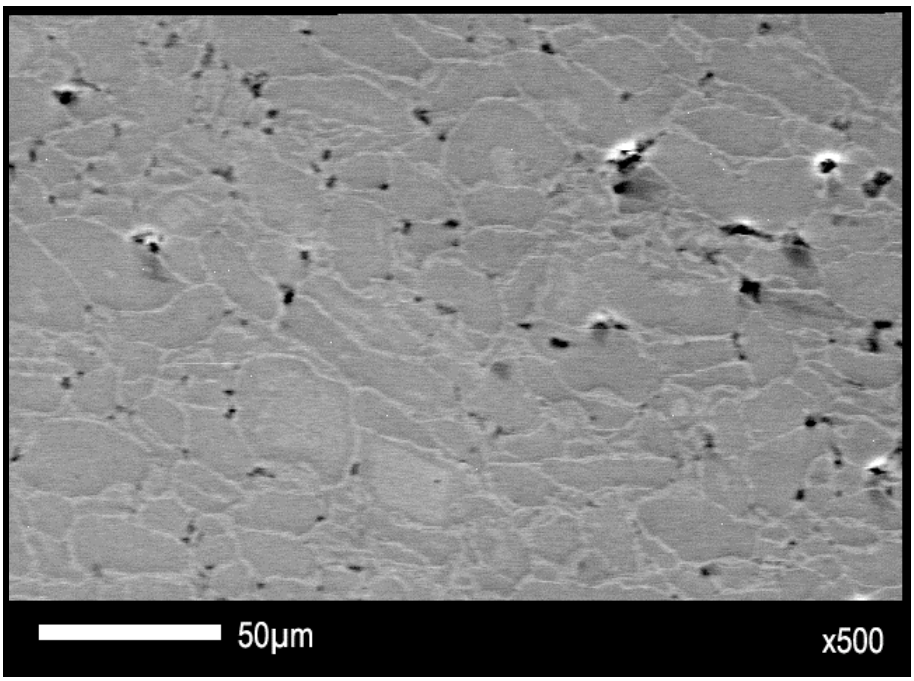

Figure 37: SEM of P2C consolidated sample S3

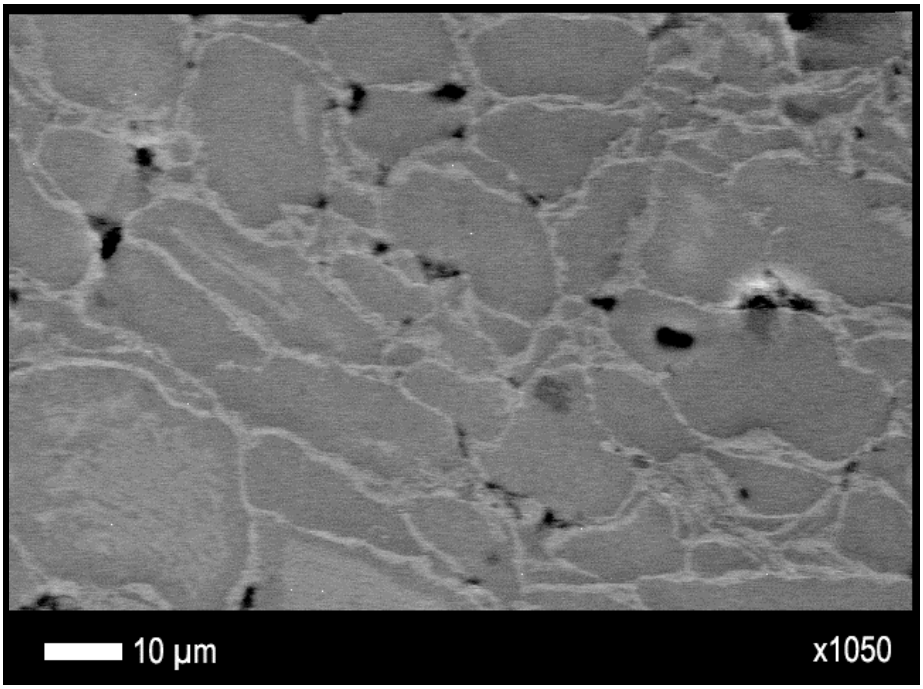

Figure 38: SEM of P2C consolidated sample S3

Samples S4 and S5

Samples S4 and S5 were also consolidated into 1-inch diameter discs from powders procured from ESPI, Inc., Ashland, Oregon. The samples were consolidated at 1200^{o}C, 235^{o}C below the α-transus temperature and 70^{o}C above the α+γ phase boundary temperature. Before reaching the consolidation temperature, the powder compact of sample S4 was applied with a pulsed DC voltage for 20 minutes. SEM micrographs of samples S4 revealed microstructure consisting of large and equiaxed gamma grains and pockets of lamellar colonies. Few precipitates of α_2 (Ti_3Al) phase were found to be segregated at the grain boundaries. This was found to be characteristic of the near gamma and duplex microstructure. The average grain size as determined from the line-intercept method was found to be 13 μm. The dark black areas in the SEM micrographs of sample S4 were analyzed by EDS and found to contain oxygen and carbon.

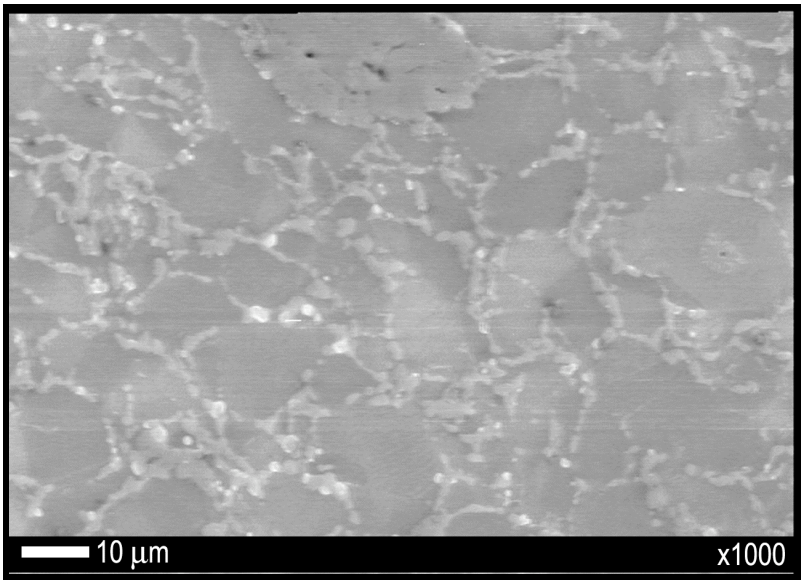

Figure 39: SEM of P2C consolidated sample S4

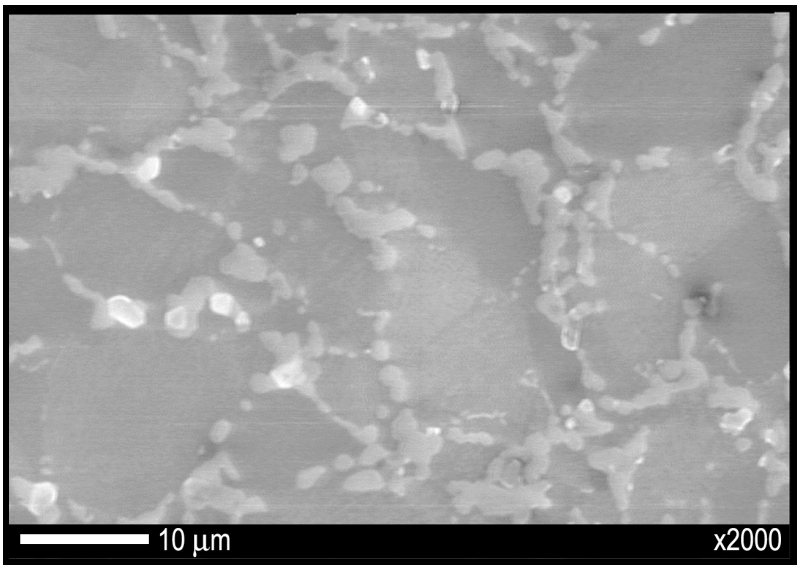

Figure 40: SEM of P2C consolidated sample S4 showing α_2 (Ti_3Al) precipitates at the grain boundaries

Sample S5 was consolidated at same conditions as sample S4, except that the pulsing process was not applied to it. The SEM micrographs of sample S5 in Figure 41 and Figure 42 showed similar characteristics to that of sample S4. The average grain size of sample S5 was determined to be 13 µm.

Sample S6

Sample S6 was also consolidated into 1-inch diameter disc from powders procured from ESPI, Inc., Ashland, Oregon. Sample S6 was consolidated at 1400^{o}C, 35^{o}C below the α-transus temperature. Before reaching the consolidation temperature, the powder compact of sample S6 was subjected to a pulsed DC voltage for 20 minutes. The SEM micrographs of sample S6 shown in Figure 43 and Figure 44 reveal the presence of lamellar colonies made up of alternating α_2 and γ plates. The average size of the lamellar

colonies was found to be in the range of 75 micrometers. The microstructure was characterized as fully lamellar. The average thickness of lamellae was found to be 1µm.

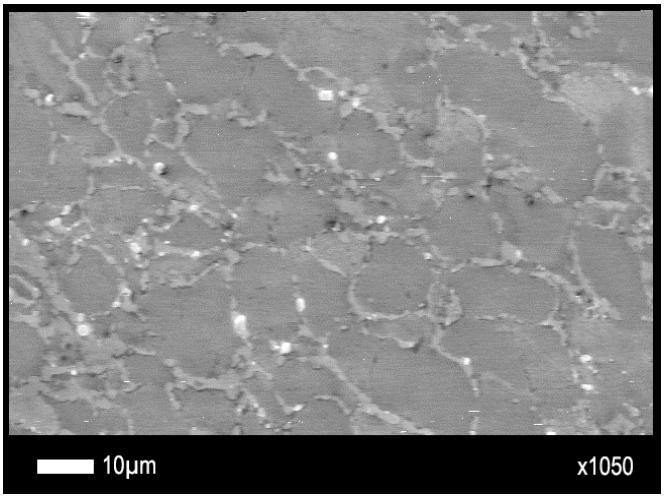

Figure 41: SEM of P2C consolidated sample S5

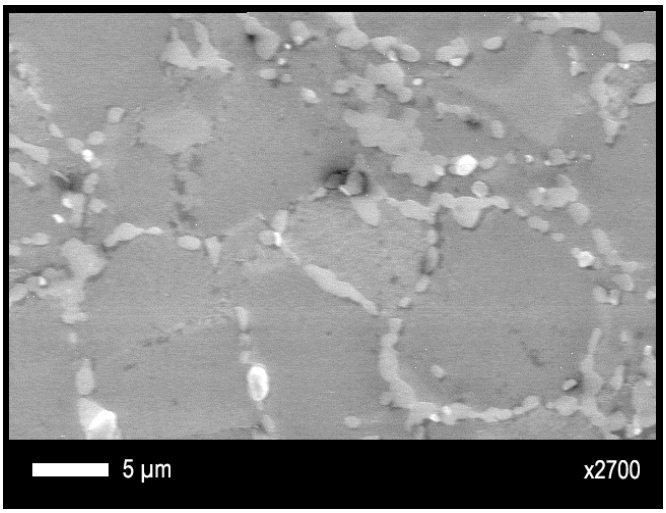

Figure 42: SEM of P2C consolidated sample S5 showing increased presence of Carbon and Oxygen Impurities in the dark black areas

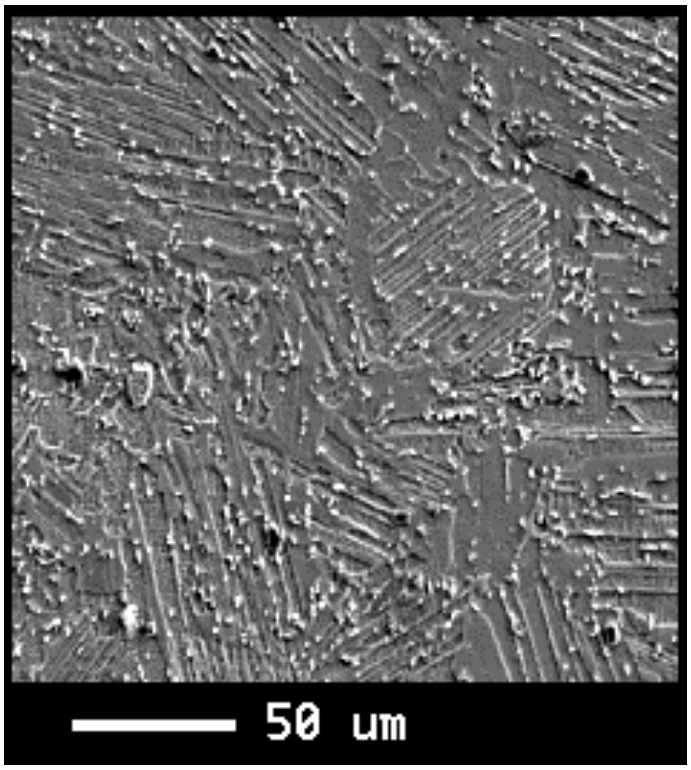

Figure 43: SEM of P2C consolidated sample S6 showing lamellar colonies

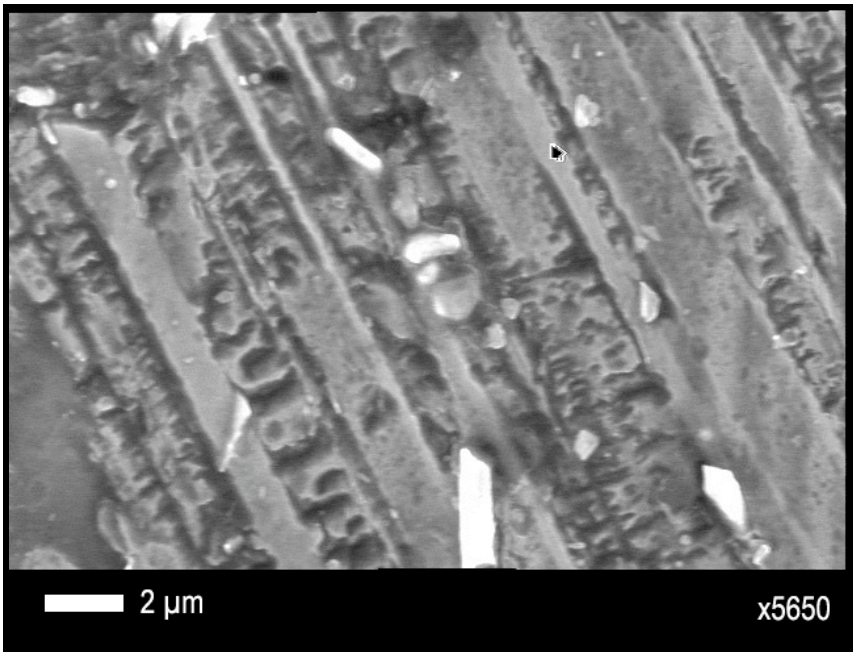

Figure 44: SEM of P2C consolidated sample S6 showing a closer view of the lamellar colonies

Samples T1 and T2 (Tile Samples)

Two tiles of the dimension 3" x 2.3" x 0.25" were consolidated by P2C from powders procured from ESPI, Inc., Ashland, Oregon. Both the tiles were consolidated at 1000^{o}C, 435^{o}C below the α-transus temperature and 130^{o}C below the α+γ phase boundary temperature. Before reaching the consolidation temperature, the powder compact of sample S2 was subject to a pulsed DC voltage for 20 minutes. Tile 1 (T1) was cooled from consolidation temperature to room temperature at an accelerated cooling rate of 200 K/min, while Tile 2 (T2) was cooled at the usual cooling rate of 60 K/min. All of the samples mentioned above are also cooled at 60 K/min. The consolidation conditions of the tiles are listed in Table 7 with a sample ID of T1 and T2 for Tile 1 and Tile 2, respectively.

The SEM micrograph of T1 is shown in Figure 45. The microstructure of T2 in Figure 46 looks similar to that of T1 with a mix of large and small gamma grains The dark areas were identified to be γ (TiAl) phase, while the light areas were identified as α_2 (Ti_3Al) phase by EDS.

Both the microstructures were indentified with dark black areas at the grain boundaries, which were found to be pores or concentration of oxygen and carbon impurities. The presence of significant amount of pores is confirmed by density measurements. The density of both the tile samples was much lower than that of α_2 (Ti_3Al) and γ (TiAl) phases. The average grain size of T1 and T2 as determined by the line-intercept method and was 10 μm.

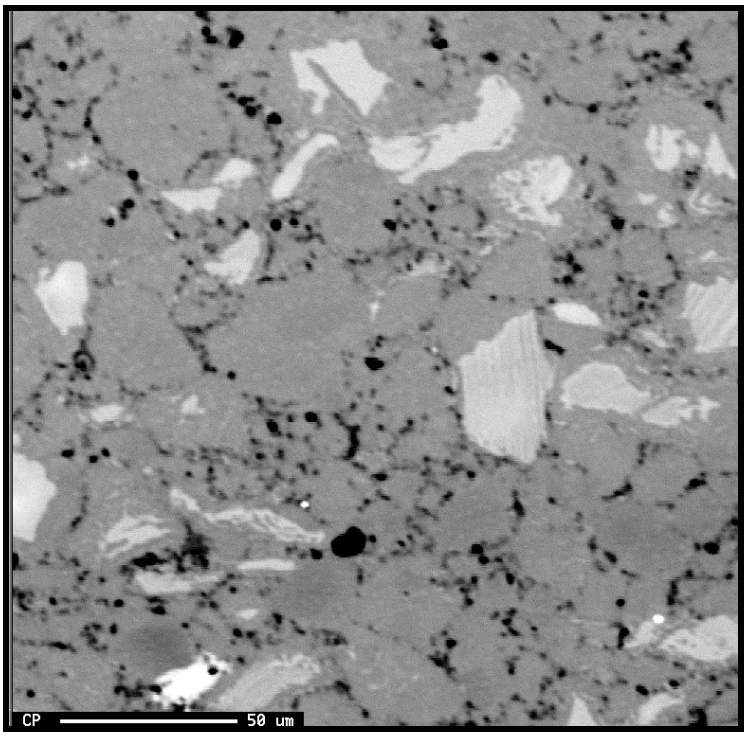

Figure 45: SEM of P2C consolidated tile 1 (T1)

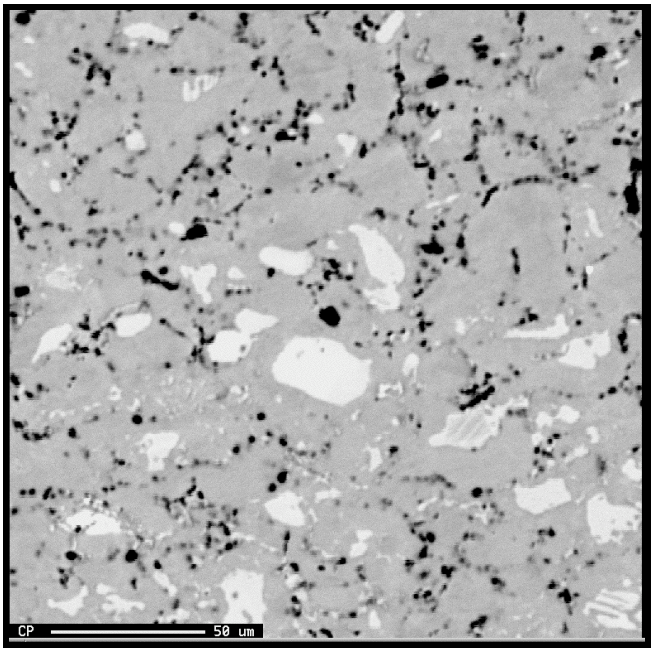

Figure 46: SEM of P2C consolidated tile 2 (T2)

2.6 Mechanical Tests

The mechanical properties of all the consolidated samples were characterized by four-point bend tests. The four-point bend tests were performed to determine elastic modulus and flexure strength of bend bars machined from the consolidated samples. The four-point bending tests were also performed on chevron notch bars to yield fracture toughness. Additionally, the four-point bend tests were performed at temperatures up to 950^{o}C. Finally, the micro-hardness of all the consolidated samples were measured by a diamond Vickers indent test.

2.6.1 Room Temperature Mechanical Properties Characterization of Ti-50%Al Discs

The room temperature four-point bending tests were performed on 3 to 5 bend bar samples machined from each consolidated sample. The mechanical property values reported below are an average of the bend bars tested per sample. On some of the four-point bending tests, a strain gage was attached on the bottom side of the bend bar to measure elastic modulus in tension. In some tests, the strain gage data was not available. Hence, the elastic modulus in bending calculated from equations in Appendix A (with load versus displacement data from four-point bending tests) was used for comparison of elastic modulus of all samples.

Sample S1

Figure 47 shows the load versus displacement plot for sample S1 bend bars, where the average flexure strength was found to be 560.90 MPa. The slope of the force versus

displacement plot in Figure 47 yielded an average elastic modulus in bending of 130.86 GPa.

Samples S2 and S3

The four-point bending results for samples S2 and S3 are shown in Figure 48 and Figure 49 in the form of load versus displacement plots and stress versus strain plots, respectively. Both the samples exhibited similar stiffness except that the flexure strength for sample S3 was lower than that of S2. Both the samples had similar consolidation conditions, except that the powder compact for sample S2 was subjected to a pulsing current for 20 minutes before the actual consolidation.

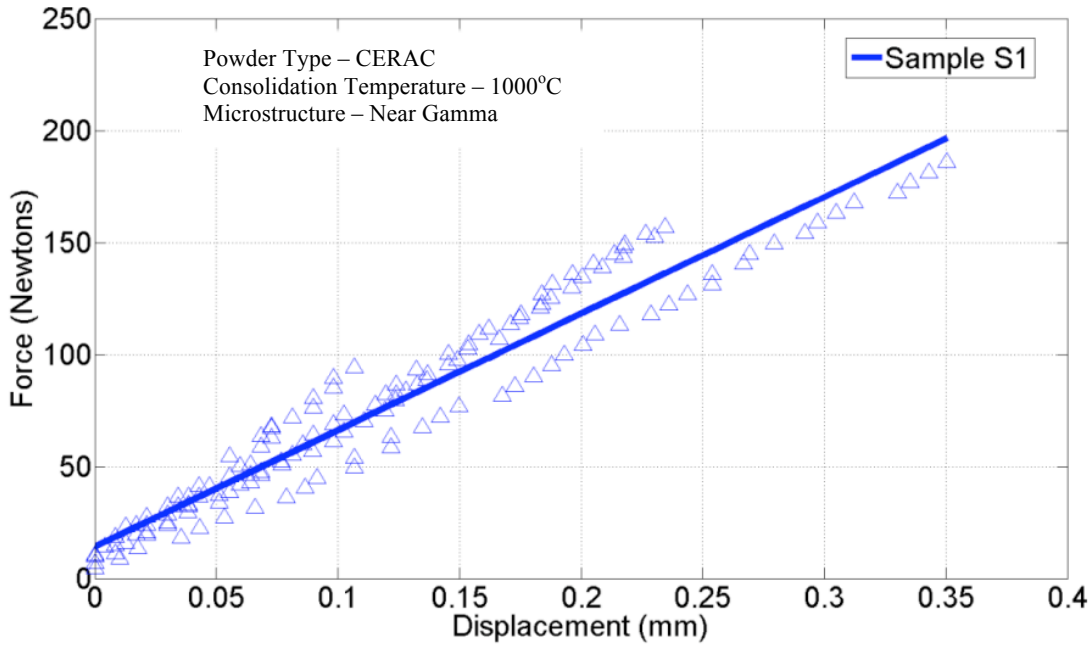

Figure 47: Sample S1 bend bar under four-point bending test

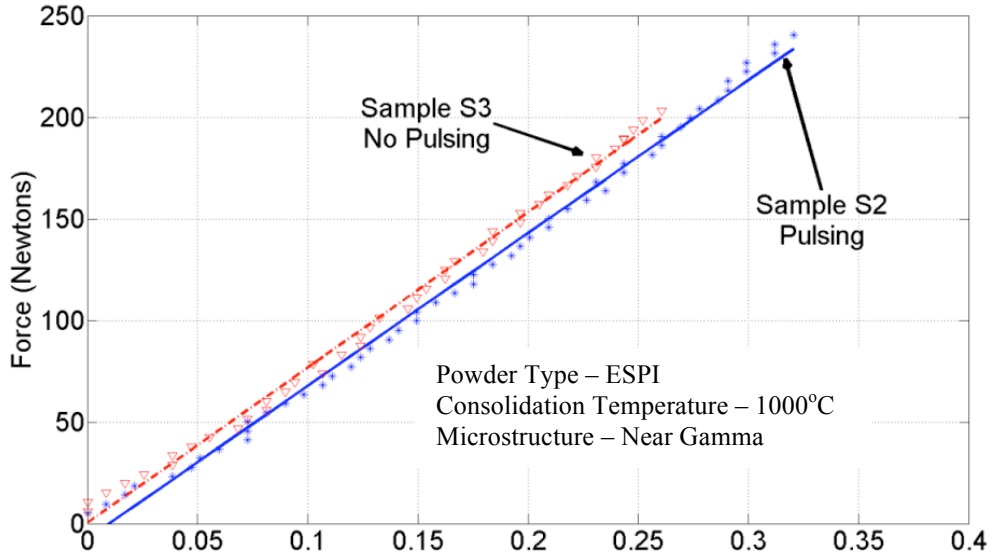

Figure 48: Load v. displacement plot for samples S2 and S3 in four-point bending

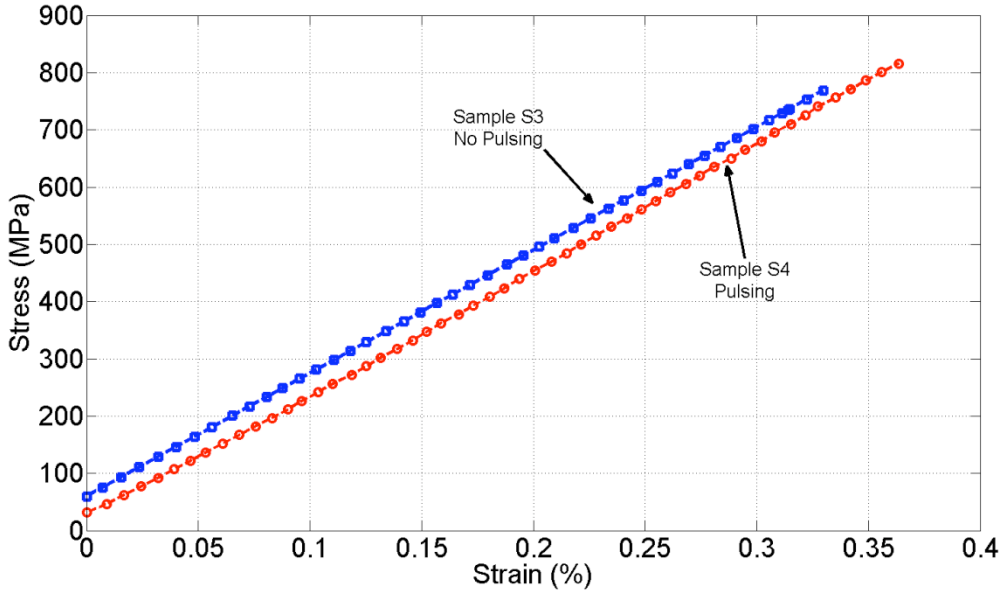

Figure 49: Stress v. strain plot for samples S2 and S3 in four-point Bending

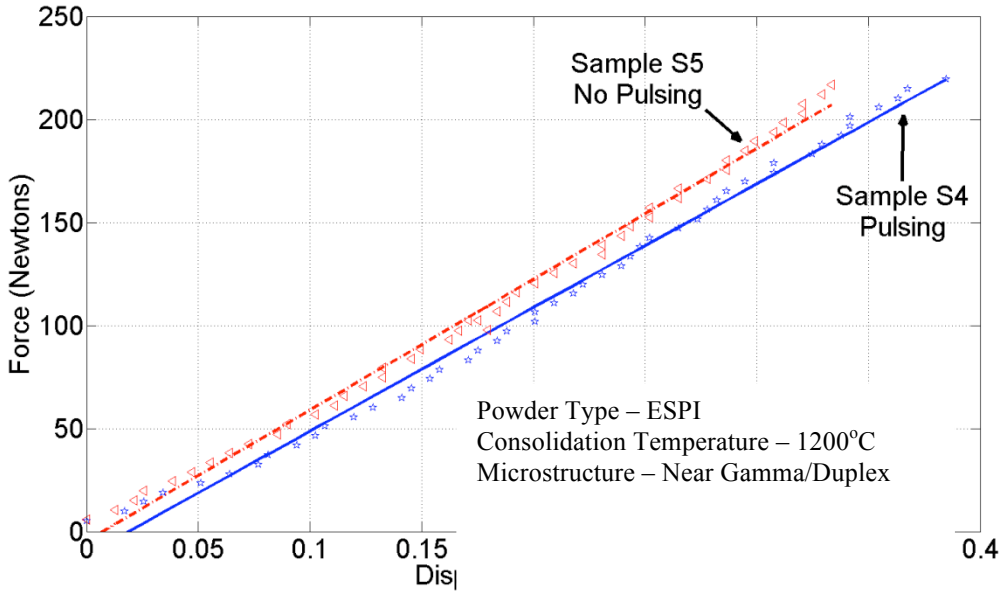

Figure 50: Load v. displacement plo ending

Samples S4 and S5

The four-point bending results for samples S4 and S5 are shown in Figures 50 and 51 in the form of load versus displacement plots and stress versus strain plots, respectively. The test results show similar stiffness and flexure strength values for both the samples. Samples S4 and S5 were consolidated under the same conditions, except that the powder compact for sample S4 was subjected to a pulsing current for 20 minutes before the actual consolidation.

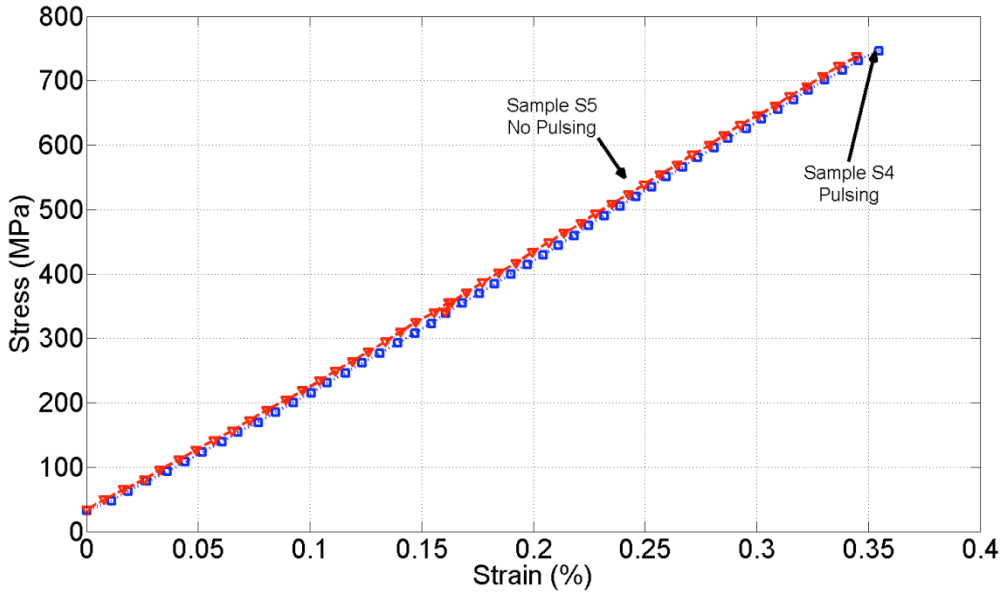

Figure 51: Stress v. strain plot for samples S4 and S5 in four-point bending

Sample S6

Figure 52 shows the load versus displacement plot for sample S6, which was consolidated very close to the α phase field. The flexure strength and elastic modulus in bending for sample S6 was much lower compared to the rest of the samples.

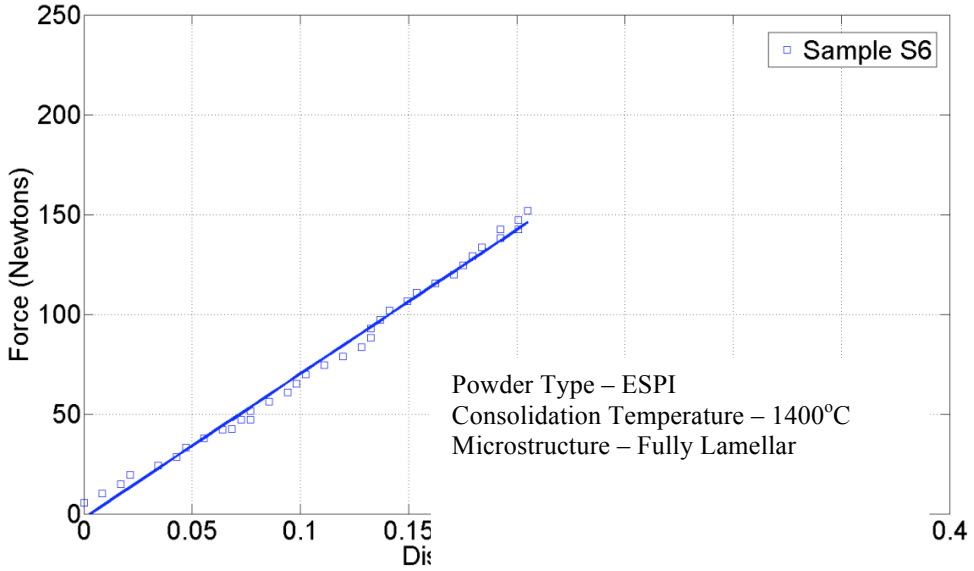

Figure 52: Load v. displacemen ending

Table 8: Room temperature mechanical properties for disc samples

Sample ID	Consolidation Temperature (Celsius)	Microstructure Type	Flexure Strength (MPa)	Elastic Modulus in Bending (GPa)	Elastic Modulus in Tension (GPa)	Micro-Hardness (GPa)
S1	1200*	Near gamma/ Duplex	560.90	130.86	-	2.74
S2	1000*	Near gamma	815.98	149.50	218.98	3.27
S3	1000	Near gamma	691.53	153.94	215.65	3.46
S4	1200*	Near gamma/ Duplex	746.54	122.17	206.24	2.84
S5	1200	Near gamma/ Duplex	737.33	129.28	206.39	2.83
S6	1400*	Fully Lamellar	422.96	108.12	-	2.58

* Indicates pulsing

Table 8 summarizes the micro-structural characteristics and mechanical properties of all the disc samples at room temperature. In general, the mechanical properties were found to be superior to the values reported in literature for gamma titanium aluminides manufactured by ingot metallurgy [113; 114].

2.6.2 Room Temperature Mechanical Properties Characterization of Ti-50%Al Tiles

Two tiles of dimension 2" x 3" x 0.25" were consolidated by P2C. Both the tiles were consolidated at 1000^{o}C at 30 MPa for 20 minutes except that the first tile (T1) was cooled at 200 K/min from the consolidation temperature, while the second tile (T2) was cooled at 60 K/min. Figure 53 shows the load versus displacement plot for both tiles T1 and T2 in four-point bending. As shown, the modulus of bending for tile 2 is greater than that of tile 1.

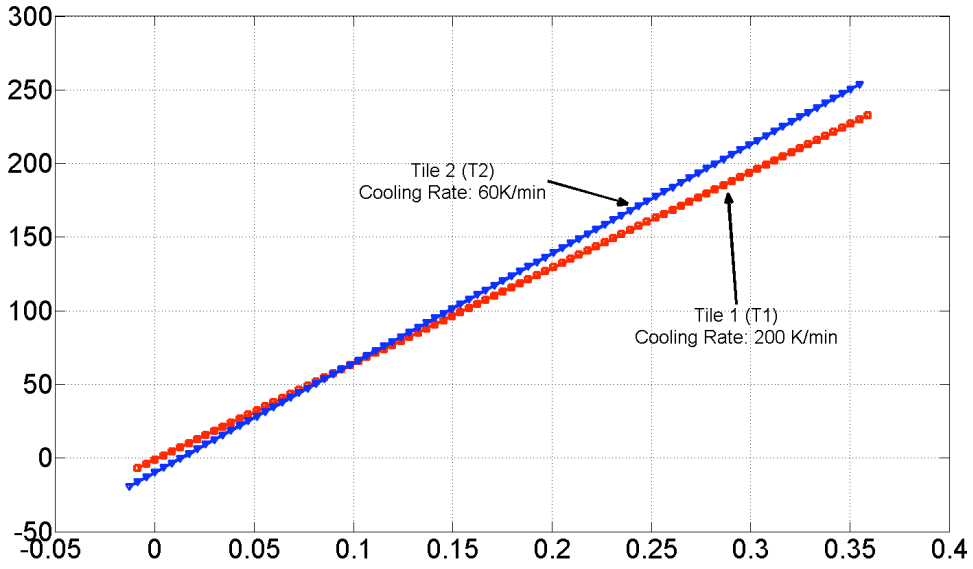

Figure 53: Force v. displacement plot for P2C consolidated tiles in four point bending

The difference in the stiffness of tile 1 and tile 2 is further shown by the stress versus strain plot in Figure 54. Both the tiles exhibit approximately the same flexural strength.

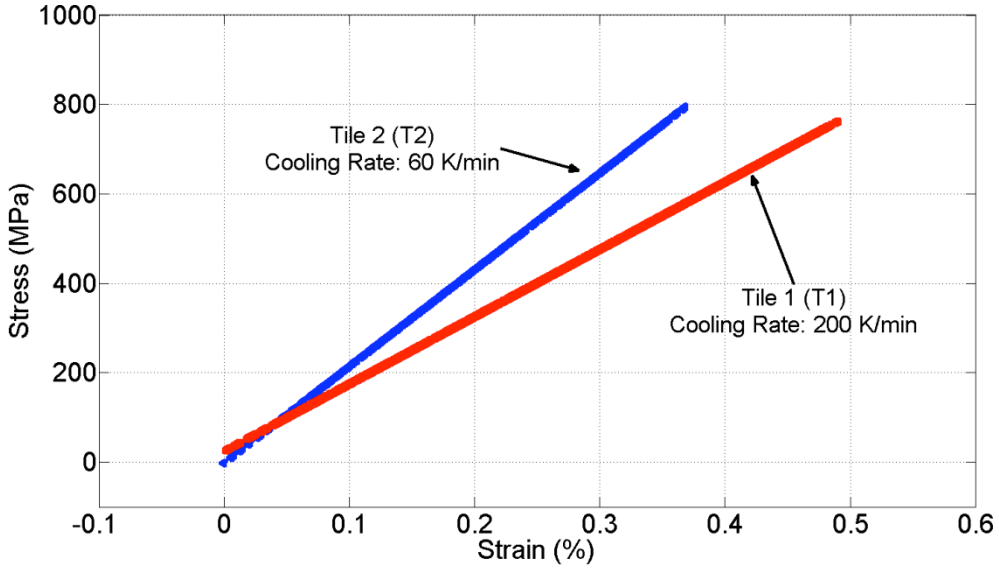

Figure 54: Stress v. strain plot for P2C consolidated tiles in four-point bending

The fracture toughness of the tiles was determined by four-point bending tests performed on chevron notched specimens. Table 9 lists all the mechanical properties of the two tiles.

Table 9: Mechanical properties for Ti-50%Al tiles

Sample	Cooling Rate (K/Min)	Modulus in Bending (GPa)	Modulus in Tension (GPa)	Flexural Strength (MPa)	Fracture Toughness (MPa $m^{1/2}$)	Micro-Hardness (GPa)
Tile 1	200	132.58	148.76	787.60	7.61	2.88
Tile 2	60	151.47	216.23	808.91	9.43	3.23

2.6.3 High Temperature Mechanical Properties of Ti-50% Al Discs

The high temperature mechanical properties of Ti-50%Al discs were characterized by four-point bending tests conducted at high temperatures. These tests were conducted on bend bars machined out of sample S1. These high temperature tests were limited to temperatures up to 500°C due to limited number of bend bars available from sample S1 (One-inch diameter disc). The four-point bending fixture was loaded in a MTS test frame and enclosed with a clamshell oven as shown in Figure 23.

The four-point bending tests were conducted at 15°C, 150°C, 350°C, and 500°C. The plot in Figure 55 shows the force versus displacement curves for all the temperatures.

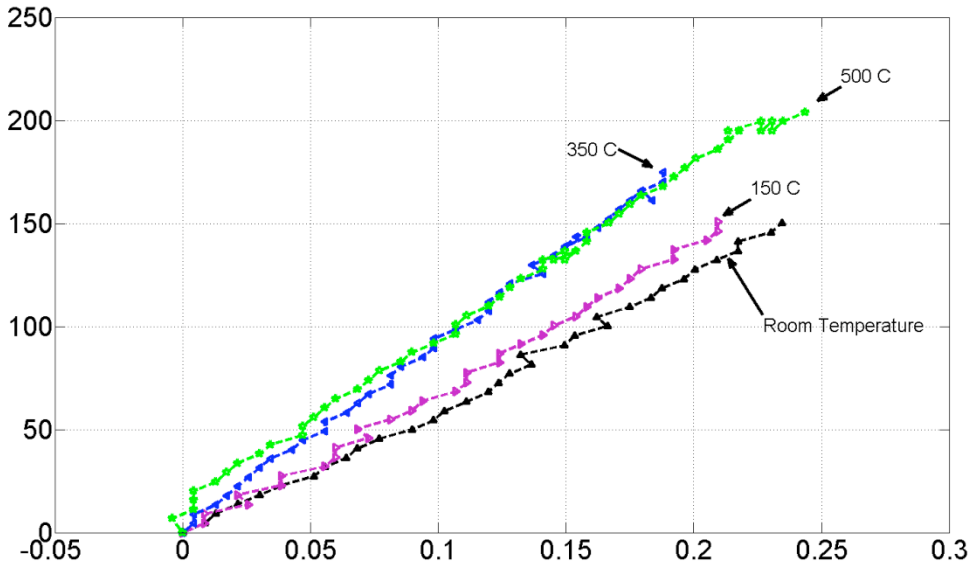

Figure 55: High Temperature force versus displacement plot for sample S1 under four-point bending

The flexure strength and modulus in bending of sample S1 at four different temperatures are tabulated in Table 10. The flexure strength was found to increase with temperature. The modulus in bending also increases with temperature up to 350^{o}C and then starts to decrease.

Table 10: High temperature mechanical properties of Ti-50%Al sample S1

Temperature (Celsius)	Flexure Strength (MPa)	Modulus in Bending (GPa)
15	560.90	131.04
150	593.96	144.10
350	622.10	183.74
500	806.24	170.12

2.6.4 High Temperature Mechanical Properties of Ti-50% Al Tiles

The high temperature mechanical properties for tile 2 were characterized at temperatures up to 950^{o}C both in air and vacuum. This was done by conducting four-point bending tests at high temperatures in air and vacuum as shown in Figure 23 and Figure 24, respectively.

The force versus displacement plots for high temperature four-point bending tests for tile 2 in air and vacuum are shown in Figure 56 and Figure 57 respectively. Table 11 further lists all the high temperature properties for tile 2 in air and vacuum.

The flexure strength of tile 2 samples was found to increase with increase in temperature up to 400°C and then started decreasing. The flexure strength at 950°C was found to be 75% of the flexure strength at room temperature.

Furthermore, the elastic modulus in bending was also found to increase with temperature up to 600°C and then start to decrease. The material exhibited plastic deformation at temperatures of 600°C and higher.

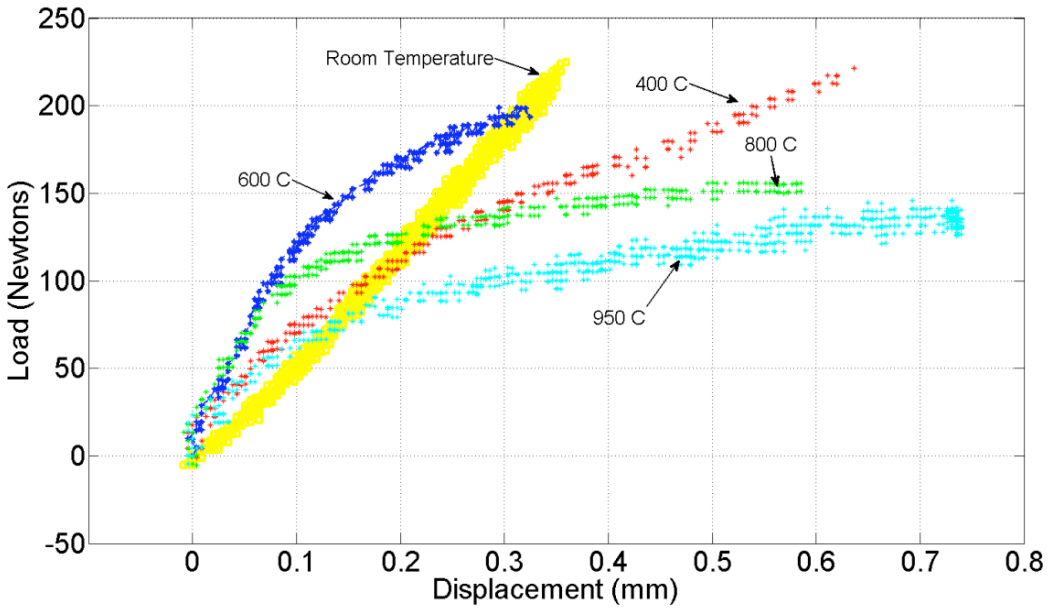

Figure 56: Load v. displacement plots for tile 2 samples in four-point bend tests at high temperature in air

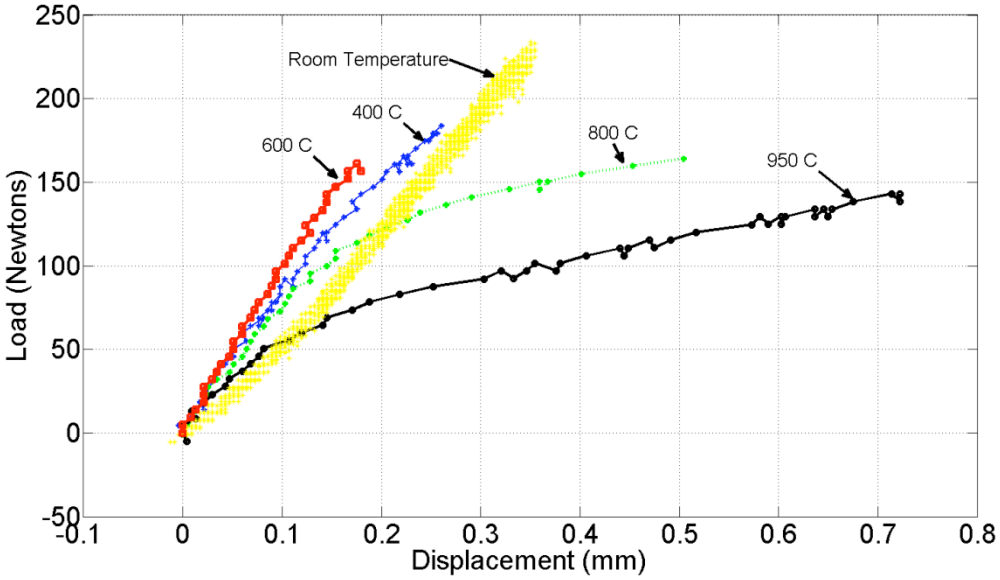

Figure 57: Load v. displacement plots for tile 2 samples in four-point bending tests at high temperature in vacuum

Table 11: High temperature mechanical properties for tile 2 in air and vacuum

Temperature (Celsius)	Modulus in Bending (GPa)		Flexure Strength (MPa)	
	Air	Vacuum	Air	Vacuum
15	151.47	153.58	808.915	787.6078
400	149.17	168.99	921.6191	970.9896
600	199.78	193.45	813.0638	876.3772
800	158.10	151.37	687.0798	780.5198
950	118.42	113.71	612.3857	764.0871

2.7 Discussion

2.7.1 Microstructure Evolution

Disc Samples: Ti-50%Al powders were consolidated in the $\alpha_2+\gamma$, $\alpha+\gamma$, and close to the pure α phase fields as shown in the Ti-Al binary phase diagram in Figure 18. As a result, three characteristic microstructures were produced namely Near gamma, Near gamma/Duplex, and Fully Lamellar.

Near Gamma Microstructure – Samples S2, S3, T1 and T2

Near gamma microstructure was obtained in samples S2 and S3, which were consolidated in the $\alpha_2+\gamma$ phase field at T_α-435^{o}C (1000^{o}C). The Gamma phase is the dominant phase at this composition. Therefore, heat-treatment at these temperatures results in the formation of coarse gamma grains [112]. But due to the reduced consolidation time, grain growth was controlled in both the samples, which led to the formation of fine gamma grains characterized with continuous bands of segregated α_2-Ti_3Al particles at the grain boundaries as shown in Figure 36 and Figure 38.

The microstructure for samples T1 and T2 showed characteristics of near gamma microstructure, except that it consisted of a significant amount of pores segregated at the grain boundaries. This can be attributed to the fact that T1 and T2 were tile samples, which were much larger in size than the disc samples. The consolidation time for the tiles was only 15 to 20 minutes, while that of the discs was 10 minutes. Comparing the ratio of the size of the discs and tiles to that of the consolidation time it is evident that the consolidation of tiles was not fully complete resulting in lower density and higher porosity. This is further apparent in the density values obtained for the tiles. The density

of the tiles was much lower than the density of both α_2 and γ phases. Also the consolidation pressure for the tiles (30 MPa) was much lower than that for discs (54 MPa – 130 MPa).

Near Gamma/Duplex Microstructure – Samples S1, S4 and S5

Samples S1, S4 and S5 were consolidated in the $\alpha+\gamma$ phase fields at T_α-235^{o}C (1200^{o}C). At this composition, the α phase volume fraction starts to increase. In the next chapter it will be shown that the volume fraction of α and γ phase come to an equilibrium at around T_α-145^{o}C, which in turn results in the formation of fine-grained duplex microstructure. The duplex microstructure is comprised of gamma grains and lamellar colonies composed of alternating plates of α_2 and γ plates. But at T_α-235^{o}C, gamma phase is still dominant. α_2 (Ti_3Al) particles start disordering at this temperature, and alpha precipitates begin nucleating to grow into alpha plates resulting in the formation of lamellar colonies. The formation of the lamellar colonies is further characterized by grain growth. At T_α-235^{o}C, the alpha precipitates which do not form lamellar colonies remain segregated at the grain boundaries. This microstructure has been termed as a combination of Near gamma and duplex. The duplex microstructure is usually characterized with fine gamma grains and lamellar colonies. But in this case, the large gamma grains are still present while the lamellar colonies are growing. The growth of gamma grains and lamellar colonies has not reached an equilibrium. Hence, we see a mix of large gamma grains, as well as fine gamma grains along with growing lamellar colonies. The consolidation time for sample S1 was 20 minutes, while that of S4 and S5 was 10 minutes. The effect of higher consolidation time for sample S1 is evident in the increased average grain size, which is 20 μm. The grain size of samples S4 and S5 was 13 μm.

Fully Lamellar Microstructure – Sample S6

Sample S6 was consolidated at T_{α}-45^{o}C. At this temperature, the α phase is the dominant phase. Hence, consolidation at this temperature results in the formation of lamellar colonies. Since, the volume fraction of the gamma phase is small compared to that of alpha phase, the formation of lamellar colonies is very rapid. There are no barriers of gamma grains restricting the growth of lamellar colonies and the resultant colony size is much larger than for the samples consolidated at lower temperatures. The average colony size for sample S6 was found to be in the range of 50 μm.

2.7.2 Factors Affecting Mechanical Properties

Microstructure and Grain Size: As evident from the previous section, each microstructure type is characterized by grain size and grain type. The Near gamma microstructure is mainly composed of gamma grains, which are generally coarse. The Duplex microstructure is characterized by fine gamma grains and lamellar colonies. The Near gamma/Duplex microstructure type falls between Near gamma and Duplex characterization. It has coarse gamma grains and along with it has newly formed lamellar colonies. Finally, the fully lamellar microstructure is characterized with large lamellar colonies.

Near gamma microstructure was produced in samples S2, S3, T1 and T2. The grain size for all these samples was around 10 μm. In general, the Near gamma microstructure would be expected to have large grain size, but due to rapid consolidation the grain growth in this case was controlled significantly.

The Near gamma/Duplex microstructure was produced in samples S1, S4, and S5. The duplex microstructure has the finest grains associated with it. But before evolving into duplex microstructure, there is grain growth of the newly formed lamellar colonies. Hence, the grain size for Near gamma/Duplex microstructure was slightly higher than that of Near-gamma microstructure. The grain size for samples S1, S4 and S5 was in the range of 13 μm to 20 μm. The fully lamellar microstructure has the highest grain growth. The α phase domination leads to rapid growth of lamellar colonies.

Table 12 below lists the microstructure type and grain size of the disc samples along with their flexure strength and micro-hardness. A plot of flexure strength versus grain size in Figure 58 shows the inverse relationship between the grain size and flexure strength. For consistency in comparison, all the samples in Table 12 and Figure 58 are disc samples, which were applied with a pulsed DC voltage before consolidation. The difference between samples with pulsing and without the pulsing process is discussed in the next section.

Table 12: Effect of grain size and microstructure on mechanical properties

Sample ID	Grain Size (μm)	Microstructure Type	Flexure Strength (MPa)	Micro-Hardness (GPa)
S1	20	Near gamma/ Duplex	560.90	2.74
S2	10	Near gamma	815.98	3.27
S4	13	Near gamma/ Duplex	746.54	2.84
S6	50	Fully Lamellar	422.96	2.58

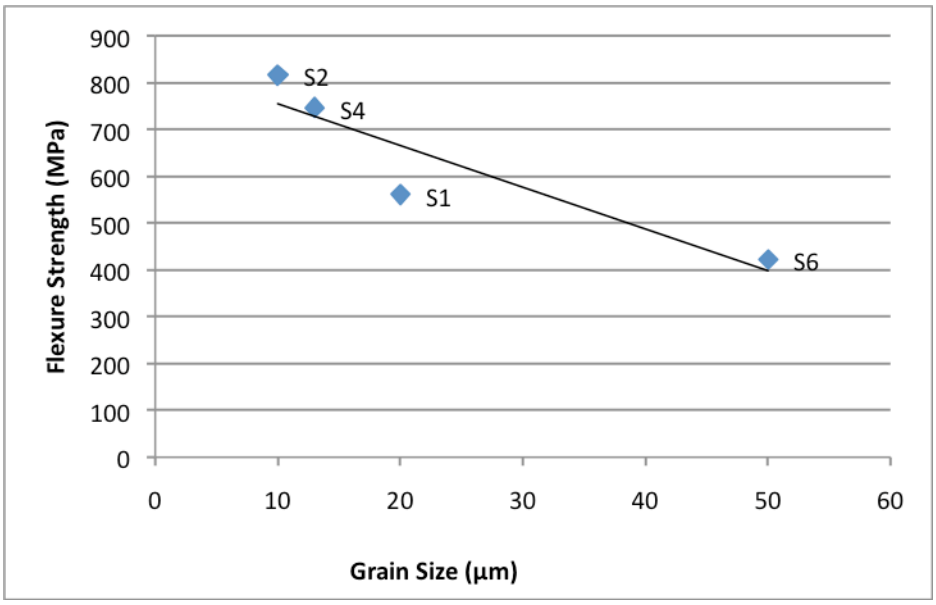

Figure 58: Flexural strength of Ti-50%Al disc samples v. grain size

Further from Table 8, it can be concluded that the elastic modulus in bending is dependent on the microstructural morphology. For microstructure with dominant gamma phase such as Near gamma, the elastic modulus in bending is highest and steadily decreases for Near gamma/Duplex and Fully lamellar as the volume fraction of gamma phase decreases and α_2 phase increases. This can be attributed to the fact that the elastic modulus for α_2 (Ti_3Al) is in the range of 110 GPa, while that of γ (TiAl) is in the range of 180 GPa [9].

The same relationship holds for micro-hardness of the material. As evident from Table 8, for microstructure with dominant Near gamma phase, the micro-hardness is high and steadily decreases for Near gamma/Duplex and Fully lamellar with increasing α_2 (Ti_3Al) phase.

Pulsing: For comparison purposes, two of the disc samples S3 and S5 were not subjected to a pulsed DC voltage before consolidation. As discussed earlier, pulsing removes all oxides and other impurities from the surface of the powders. This in turn enhances particle rearrangement and diffusion.

Pulsing had significant impact on the samples consolidated at temperatures (1000^{o}C) in the $\alpha_2 + \gamma$ phase field. As evident from comparison of microstructures of samples S2 (Figure 36) and S3 (Figure 38), sample S3 (not applied with the pulsing process) showed increased presence of Oxygen and Carbon compared to that of sample S2 (applied with the pulsing process). Furthermore, the flexural strength of S3 (~691 MPa) was significantly lower than that of S2 (~815 MPa). These comparisons show that the pulsing process enhanced diffusion in sample S2 and as a result there were limited amount of impurities present in the sample which in turn enhanced its flexure strength.

On the other hand, pulsing did not play a significant role in enhancing diffusion at higher temperatures. Samples S4 and S5 were consolidated in the $\alpha_2 + \gamma$ phase field at 1200^{o}C. Sample S4 was subjected to the pulsing process, while S5 was not. The microstructures of both the samples S4 (Figure 40), and S5 (Figure 42) were similar except that the microstructure of sample S5 had small traces of Oxygen and Carbon presence at the grain boundaries. The flexure strengths of both the samples were also in the same range (S4: ~746 MPa, and S5: ~737 MPa). This can be attributed to the fact that diffusion is usually enhanced at higher temperatures. Hence, application of the pulsing process for samples consolidated at temperatures in $\alpha + \gamma$ phase field and above did not play a significant role in enhancing diffusion for Ti-50%Al.

Cooling Rate: The rate at which a Ti-50%Al sample is cooled after heat-treatment has been reported to play a role in its microstructure and mechanical properties [112]. Hence, the two tiles consolidated from Ti-50%Al powders were subjected to different cooling rates after the consolidation process. Tile 1 (T1) was cooled at 200 K/min, while Tile 2 (T2) was cooled at 60 K/min. Both the tiles were consolidated at 1000^{o}C in the $\alpha_2 + \gamma$ phase field. Rapid cooling from the consolidation temperature freezes the high temperature phase (α_2 phase) in the consolidated sample. This in turn increases the α_2 volume fraction. One of the effects of the increase in the α_2 volume fraction is decrease in the stiffness of the material. This is due to the fact that α_2 (Ti_3Al) phase has an elastic modulus in the range of 110 GPa, while the γ (TiAl) phase has an elastic modulus in the range of 180 GPa.

As shown in Figure 54 and Table 9, the elastic modulus of T1 is approximately 150 GPa, while that of T2 is approximately 215 GPa. This difference is due to the rapid cooling of T1, which in turn retained a high volume fraction of the α_2 phase.

2.7.3 High Temperature Mechanical Properties

Dependence of Flexure Strength and Elastic Modulus on High Temperature: The mechanical properties of gamma titanium aluminides have been found to exhibit anomalous behavior at high temperatures. The tensile stress of gamma titanium aluminides has been found to increase with temperature up to 500^{o}C. This has been attributed to the fact that heat-treatments at temperatures up to 500^{o}C have found to refine the microstructure of gamma titanium aluminides. This is in turn further increases the strength of the material.

Both the P2C consolidated samples S1 and T2 tested at high temperatures exhibited the anomalous high temperature behavior characteristic to gamma titanium aluminides. This can be seen in flexure strength versus temperature plots for S2 and T2 samples in Figure 59 and Figure 60, respectively. After 500°C, grain growth occurs due to diffusion and hence the flexure strength deteriorates.

The elastic modulus in bending was also found to be increase with temperature up to 600°C. At temperatures below 600°C, any metastable $\alpha_2 + \gamma$ phase present in the material transforms in to pure γ phase. Since, the elastic modulus of γ phase is higher than that of α_2 phase, the elastic modulus is found to increase with temperature up to 600°C. Between 600°C and 700°C, the material goes through its glass transition temperature and hence it shows reduction in its stiffness.

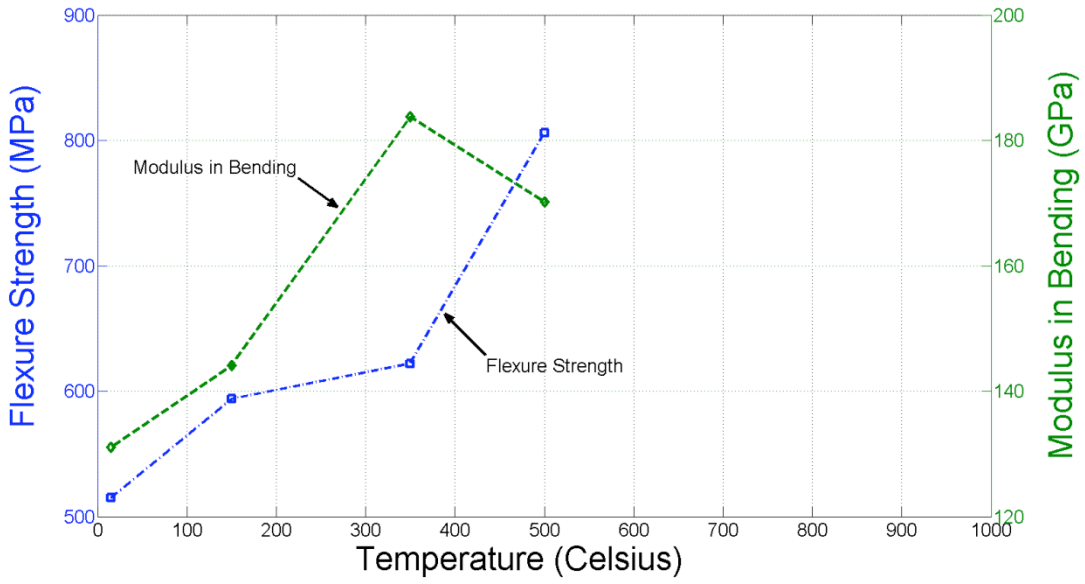

Figure 59: High temperature mechanical behavior of sample S1 in air

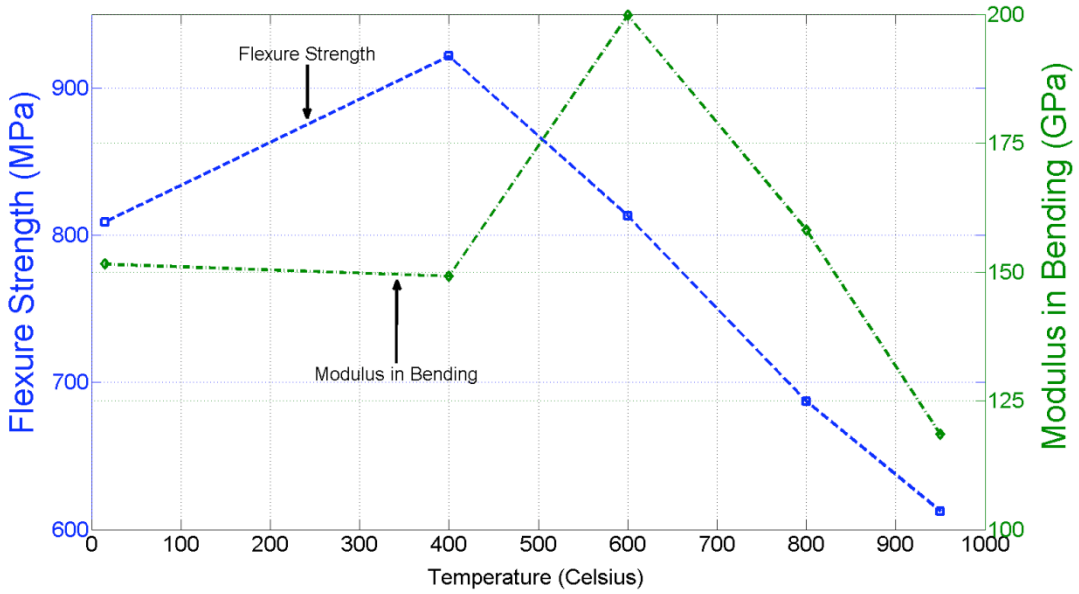

Figure 60: High temperature mechanical behavior of tile 2 in air.

Effect of Atmosphere on Strength at High Temperature: In order to study the effects of high temperature exposure in air to mechanical properties, the mechanical test data from high temperature tests in air and vacuum for tile 2 were compared. As seen in Figure 61, the flexure strength in air at high temperatures was found to be 10% lower than the flexure strength in vacuum. This shows the adverse effect of air at high temperature on the strength of gamma titanium aluminides.

Figure 62 compares the modulus in bending at high temperatures in air and vacuum. It seems that high temperature exposure in air does not have any significant impact on the bending modulus of the material. The bending modulus in vacuum and air at high temperatures are approximately of the same value.

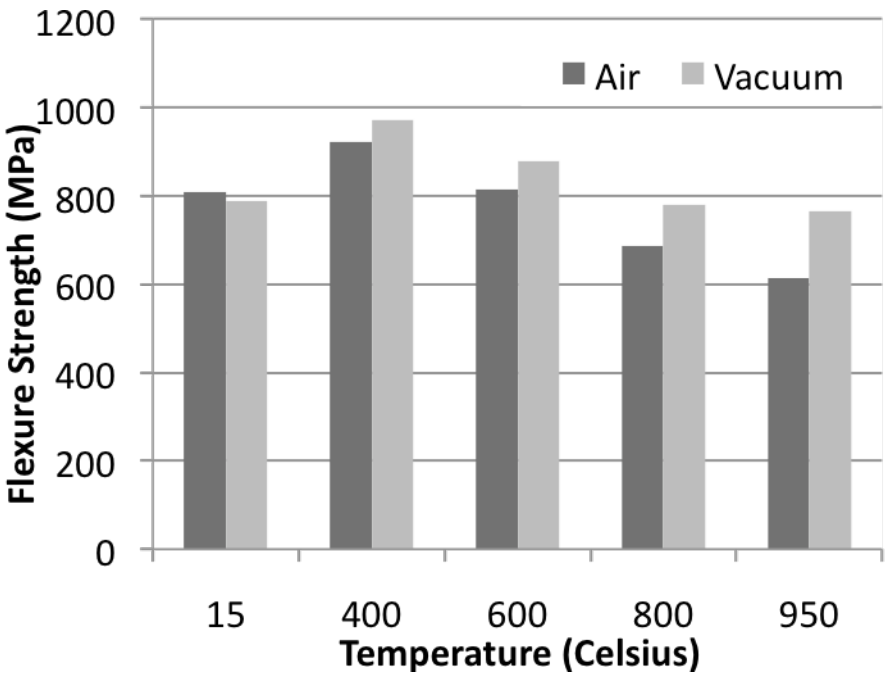

Figure 61: High temperature flexure strength for tile 2 in air and vacuum

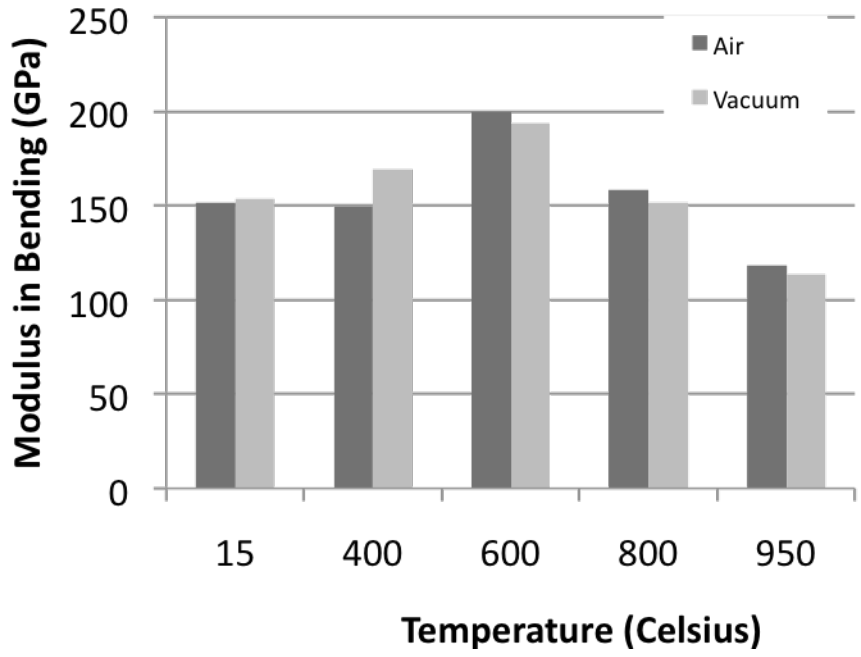

Figure 62: High temperature modulus in bending for tile 2 in air and vacuum

2.8 Summary and Conclusions

1. A rapid consolidation process called plasma pressure compaction was used to consolidate Ti-50%Al samples in form of one-inch diameter discs and 2.5" x 3" x 0.25" dimension tiles from commercially available micron-sized Ti-50%Al powders.

2. Three characteristic microstructures namely Near gamma, Near gamma/Duplex and Fully Lamellar were produced in the P2C consolidated Ti-50%Al samples. This was done by consolidating the samples at different phase field temperatures.

3. The mechanical properties of the consolidated samples were characterized and were found to have strong dependence on microstructure type and grain size. Grain size was found to be inversely proportional to the flexure strength.

4. Grain growth was minimized in all the P2C consolidated samples. Hence, its mechanical properties were found to be superior to the ones reported in the literature.

5. The application of a pulsed DC voltage before consolidation enhanced diffusion for Ti-50%Al samples consolidated in the $\alpha_2+\gamma$ phase fields.

6. The rate at which the Ti-50%Al samples were cooled after consolidation affected the amount of volume fraction of α_2 phase present. Faster cooling rates increased the volume fraction of α_2 phase, which in turn decreased the bending modulus of the consolidated sample.

7. Ti-50%Al samples tested at high temperatures exhibited increase in flexure strength up to 400^{o}C due to microstructure refinement.

8. The bending modulus was found to increase with increase in temperature up to 600^{o}C due to phase transformation of the $\alpha_2+\gamma$ metastable phase in to pure γ phase.

9. Exposure to air at high temperatures resulted in deterioration of the flexure strength of Ti-50%Al samples by 10%

Chapter 3: Characterization of Rapidly Consolidated Ti-48%Al-2%Nb-2%Cr

3.1 Introduction

Gamma titanium aluminides as shown in the previous chapter exhibit very little room temperature ductility and fracture toughness. One of the target applications for the gamma titanium aluminide based material systems is the replacement of Ni-based superalloys for high temperature (600°C - 900°C) aerospace and automobile applications [1; 9; 101].

Due to a long history of high performance and reliability, Ni-based superalloys have been the candidate material of choice for compressor and turbine blades in high-temperature gas turbine engines. Replacing the Ni-based superalloys in gas turbine engines with γ-TiAl, can increase its thrust to weight ratio by a factor of 2 [132-136, 139]. The density of γ-TiAl is in the range of 3.76 gm/cm^3, while that of Ni-based superalloys is in the range of 8 gm/cm^3. Superalloys have tensile strength in the range of 1.2 GPa with a 3-5% elongation before failure. Newly developed γ-MET TiAl alloys [132-133] with small additions of Nb, Cr, and B have matched the strength of Ni-based superalloys. Small additions of Cr have found to improve the room temperature ductility of γ-TiAl, while Nb additions have been reported to improve high temperature strength retention and oxidation resistance. Additions of B have aided in the grain refinement of γ-TiAl, which in turn improves strength.

As mentioned earlier, the microstructure of the dual (α_2 + γ) phase γ-TiAl can be engineered to exhibit a desired set of mechanical properties. In general, γ-TiAl microstructures can be classified into four major types: (1) near gamma, (2) duplex, (3) nearly lamellar, and (4) fully lamellar [141-142]. The duplex and fully lamellar microstructures have the best combination of mechanical properties [143]. Duplex microstructures have good strength and ductility, but lack creep resistance, whereas fully lamellar microstructures exhibit good creep properties, fracture toughness, fatigue resistance and high temperature strength retention, but lack room temperature ductility [144-145]. Therefore, the development of a microstructure with an optimal set of mechanical properties is required.

Several thermo-mechanical treatments have been explored to control the microstructure of γ-TiAl [132-133,145]. These treatments were aimed at producing fully lamellar microstructures with control over grain growth and lamellar spacing. One of the biggest drawbacks of γ-TiAl is that its fracture toughness and ductility are inversely proportional to each other. It has been reported that ductility increases and fracture toughness decreases with decreasing grain size [145]. It has also been shown that fracture toughness is inversely proportional to the lamellar spacing [144]. Therefore, grain size and lamellar spacing are the two most important micro-structural parameters that need to be optimized to obtain a balanced set of mechanical properties.

In order to increase the ductility of γ-TiAl and its high temperature strength retention, γ-TiAl powders with small additions of Nb and Cr were consolidated by plasma pressure compaction (P2C). As mentioned earlier, the P2C process consists of a plasma activation stage, which removes all oxides and other contaminants on the surface

of the powders. The powders are rapidly heated to high temperatures and with synergistic application of pressure, high densities are achieved with consolidation times of 20 minutes or less.

The principal objective of the current investigation was to consolidate γ-TiAl powders with small additions of Nb and Cr via P2C. The P2C consolidation was utilized to refine grain size and lamellar spacing, thereby controlling the mechanical properties of the consolidated samples.

3.2 Experimental Procedure

-325 mesh (< 45 μm) powder (procured from Crucible Research, Pittsburg, PA) with a nominal composition Ti-48%Al-2%Cr-2%Nb (at%) was consolidated via P2C to produce near-net shape parts in the form of tiles. The tiles were 3 inches x 2.25 inches x 0.25 inches (76.2 mm x 57.2 mm x 6.35 mm) in dimension as shown in Figure 63.

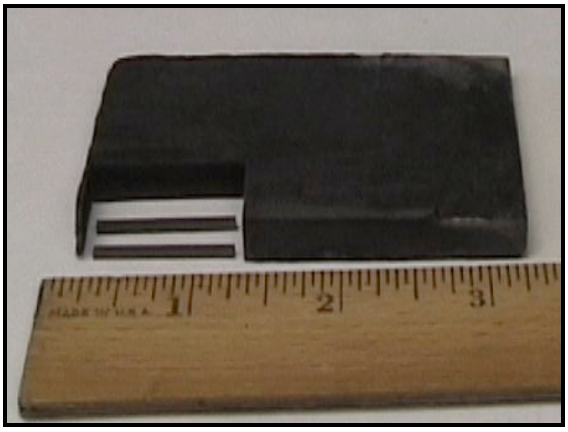

Figure 63: P2C consolidated Ti-48%Al-2%Nb-2%Cr samples of dimensions 3 inches x 2.25 inches x 0.25 inches with bend bars machined for four-point bending tests

3.2.1 Plasma Pressure Compaction

For consolidation using P2C, Ti-48%Al-2%Cr-2%Nb powders were contained in a graphite die with plungers inserted on both sides. This assembly was then placed between water-cooled electrodes. The lower electrode was raised to the bottom graphite plunger using a hydraulic cylinder to hold the entire assembly together in compression and provide a path for current flow. When sufficient inter-particle contact was established by applying uniaxial pressure, pulsed DC voltage was applied through the powder compact using a full-wave-rectified power supply.

Pulsed electrical power was applied with high current at an adequate voltage. This leads to charge build up at inter-particle gaps. This causes one particle to be charged negatively with respect to another particle that is in contact with it. As the charge accumulates, the voltage difference becomes sufficiently large to generate sparks that trigger an ionization process. The ions move towards the negatively charged particles while the electrons move toward the positively charged particles. The ionization process occurs in the form of sparks or plasma generation depending on the energy level at the inter-particle gap. The formation of plasma removes oxides and other contaminants, which form a diffusion barrier in the consolidation process. As a result, particle re-arrangement and diffusion is enhanced.

After pulsing, direct current was applied through the powder compact resulting in Joule heating. The alpha-transus temperature (T_α) of the Ti-48Al-2Cr-2Nb alloy was determined from the binary phase diagram shown in Figure 64 and literature [108]. The T_α of Ti-48Al-2Cr-2Nb was found to be 1345 $^\circ$C. Consolidation was carried out in vacuum at temperatures ranging from T_α - 145 $^\circ$C to T_α + 55 $^\circ$C as marked in Figure 64.

For comparison purposes, the consolidation conditions of two γ-TiAl samples with Ti-50%Al composition are also marked in Figure 64. The properties of these samples will be used for comparison to Ti-48Al-2Nb-2Cr samples throughout this chapter. For convenience, the sample IDs for the γ-TiAl samples is the same as in chapter II. The γ-TiAl samples used for comparison have consolidation parameters similar to that of Ti-48Al-2Nb-2Cr samples. The consolidation conditions for each alloy and their corresponding microstructures and density are listed in Table 13.

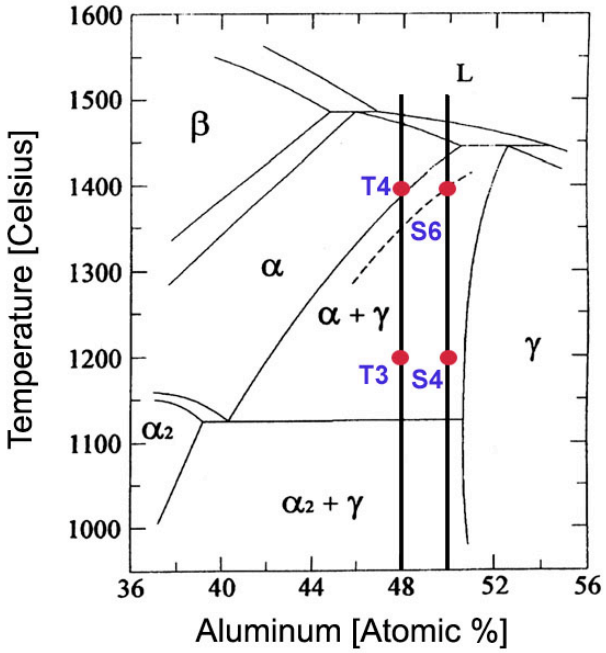

Figure 64: Partial Ti-Al binary phase diagram near the stoichiometric γ-TiAl composition. The marked points show the consolidation temperatures for each alloy composition. The dotted line shows the α-transus temperature for a γ-TiAl alloy containing 2% at. Cr [108].

Table 13: P2C consolidation parameters for TiAl-2Nb-2Cr samples along with measured density and observed microstructure

Sample	Alloy (at%)	Consolidation Pressure (MPa)	Consolidation Temperature (˚C)	Microstructure	Density (gm/cm^3)
T3	Ti-48%Al-2%Cr-2%Nb	30	T_α - 145 (1200)	Duplex	3.89
T4	Ti-48%Al-2%Cr-2%Nb	37	T_α + 55 (1400)	Fully Lamellar	3.97
S4	Ti-50%Al	54	T_α - 235 (1200)	Near-gamma/Duplex	3.91
S6	Ti-50%Al	130	T_α - 35 (1400)	Fully Lamellar	3.99

3.2.2 Microscopy and Mechanical Tests

The consolidated samples were sectioned and metallographically polished to 1 μm diamond finish. They were subsequently etched using Kroll's reagent. Their microstructure was characterized via optical microscopy, Scanning Electron Microscopy (SEM) and Energy Dispersive Spectroscopy (EDS). The SEM and optical micrographs were taken in the orientation perpendicular to the direction of compaction. The mechanical properties of the consolidated specimens were characterized using four-point bending tests. A self-aligning silicon carbide four-point bending fixture was designed according to ASTM standard C 1161 [109] with an outer-span of 20 mm and an inner-span of 10 mm. Consolidated samples were machined with chamfered edges to a dimension of 25 mm x 1.5 mm x 2.0 mm. Samples with dimension of 3 mm x 4 mm x 25

mm with a 60 degree chevron notch were also tested according to ASTM standard C 1421 in the four-point bending set-up to measure fracture toughness. All tests were conducted at a strain rate of 0.75×10^{-4} s^{-1} in a Material Testing Systems (MTS) model 810 machine. The four-point bending tests were conducted at temperatures up to 1000°C. The high temperature tests were conducted in air and vacuum (10^{-5} Pa). The four-point bending test samples were loaded such that the resultant tensile and compressive stresses were in the direction perpendicular to that of the direction of the compaction. Micro-hardness of the consolidated samples was obtained on polished specimens using a diamond Vickers indent under a load of 1000 grams with a dwell time of 15 seconds.

To ensure the accuracy of the four-point bending test data, "control" samples prepared from AD998 aluminum oxide obtained from CoorsTek, Golden CO., were also tested. The strength and fracture toughness of the AD998 samples were in excellent agreement with those reported by CoorsTek as reported in chapter II.

3.3 Results

3.3.1 Density

The consolidated specimens were found to be fully dense as measured using Archimede's technique (Table 13). The density of the consolidated specimens was found to be in the range of 3.89 – 3.97 gm/cm^3. The density [114] of γ-TiAl phase is 3.76 gm cm^3, while that of α_2-Ti_3Al phase is 4.1 gm/cm^3. With both α_2 and γ phases present in the consolidated samples, the density values of the consolidated samples was between the density of the α_2 and γ phases.

3.3.2 Microstructure Characterization

The Scanning Electron Micrographs (SEM) micrographs of γ-TiAl samples with the alloy composition of Ti-48%Al-2%Cr-2%Nb (at%) are shown in Figures 65, 66, and 67. The sample (T3) consolidated at T_α - 145 $^\circ$C showed a duplex microstructure with equiaxed gamma grains and lamellar colonies (Figure 65). The average grain size of the consolidated sample as determined from the line-intercept method was 5 μm. The sample (T4) consolidated at T_α + 55 $^\circ$C showed a fully lamellar microstructure (Figure 64). The microstructure showed significant grain growth with the grain size ranging from 100 to 2000 μm. The lamellar spacing in sample T4 was found to be 0.5 μm (Figure 67). For comparison purposes, the microstructure of samples S4, and S5 (Ti-50Al composition) are shown in Figures 68 to 71.

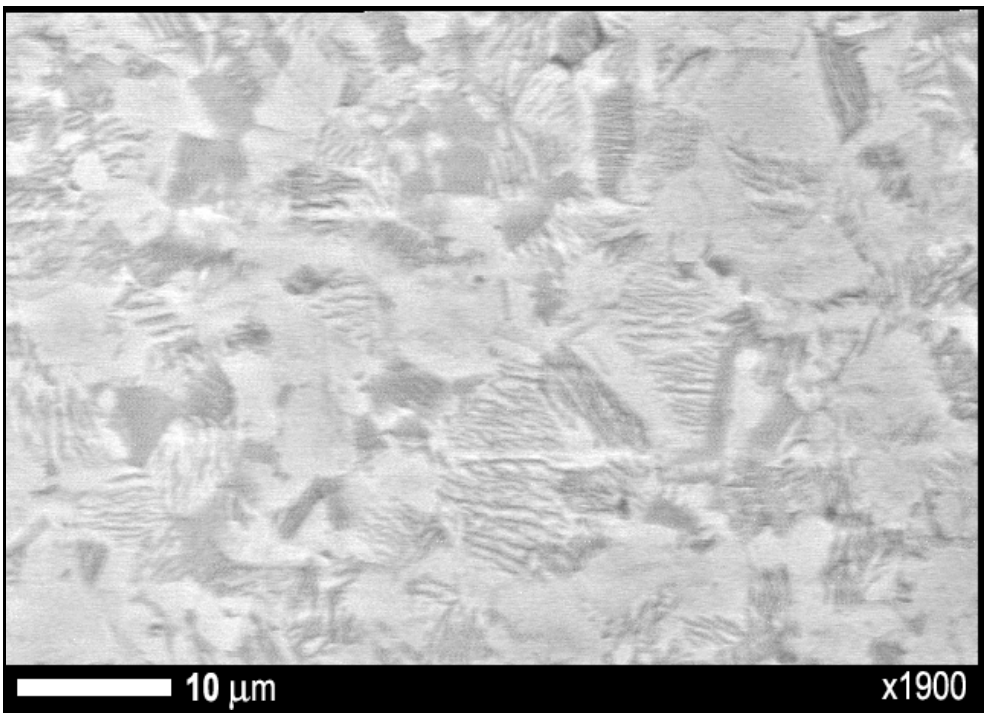

Figure 65: SEM of T3 - Ti-48%Al-2%Cr-2%Nb (at%) consolidated at T_{α} - 145 C showing a duplex microstructure

3.3.3 Mechanical Properties

The room temperature four-point bending tests were performed on bend bars sectioned from the consolidated samples. The flexural stress versus strain plots are shown in Figure 72. Ti-48Al-2Cr-2Nb with duplex microstructure exhibited a total elongation of 2.3% with 0.5% elastic and 1.8% plastic strain. The Ti-48Al-2Cr-2Nb samples with fully lamellar microstructure showed a total elongation of 1.5% with 0.3% elastic and 1.2% plastic strain. For comparison, the flexural stress versus strain plot of γ-TiAl samples S4 and S6 are also plotted in Figure 72. As shown for comparison, the Ti-50Al alloy composition exhibited no ductility.

The flexural strength and elastic modulus of all the samples were calculated from the stress versus strain curve in Figure 72 and are listed in Table 14. The fracture toughness values for all the consolidated samples are also reported in Table 14. The fracture mode of the consolidated Ti-48Al-2Cr-2Nb specimens with duplex and fully lamellar microstructure was determined through microstructural examination of the fractured samples and is shown in Figures 73 and 74. The duplex microstructure in Figure 73 exhibited mostly transgranular cleavage like fracture. The fully lamellar microstructure exhibited a mix of translamellar and interlamellar mode of fracture as shown in Figure 74.

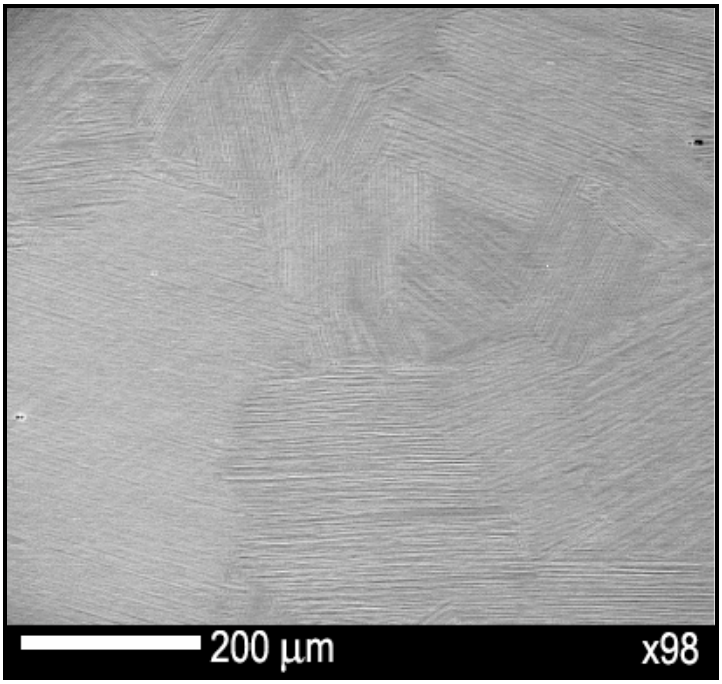

Figure 66: SEM of T4 - Ti-48%Al-2%Cr-2%Nb (at%) sample consolidated at T_{α} + 55 ˚C with a) showing colony size of 200 µm

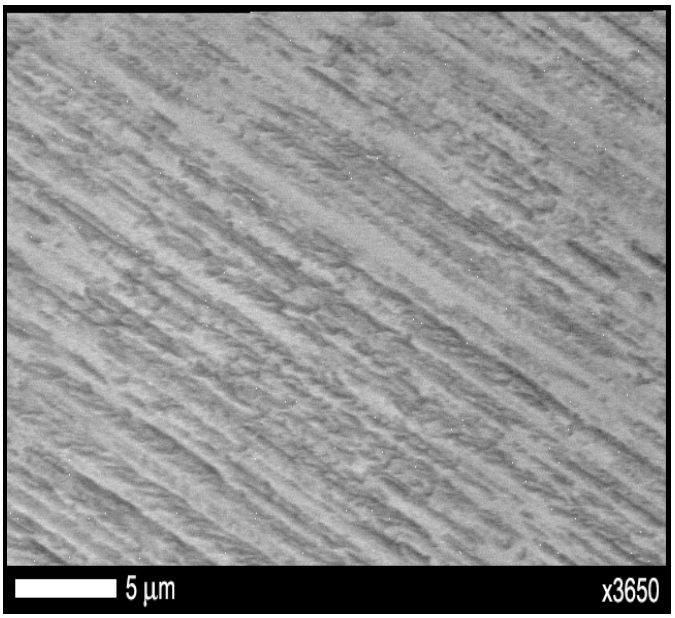

Figure 67: SEM of T4 - Ti-48%Al-2%Cr-2%Nb (at%) sample consolidated at T_{α} + 55 ˚C with showing lamellar spacing of 0.5µm

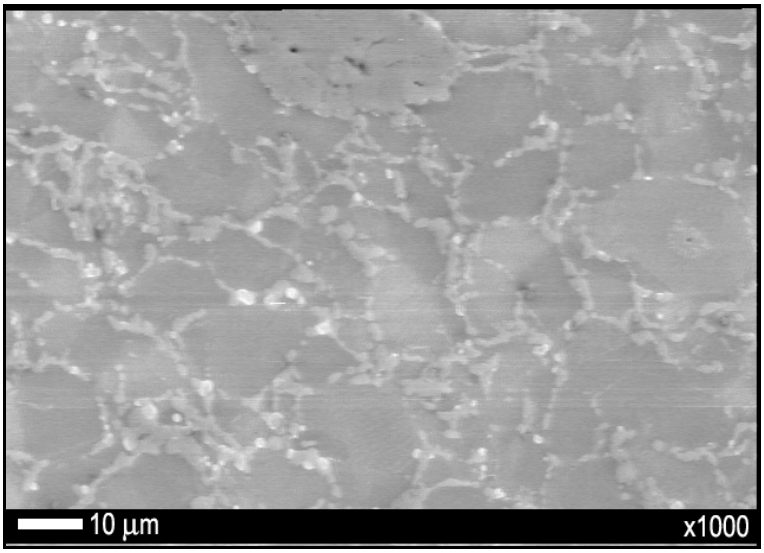

Figure 68: SEM of S4 - Ti-50%Al (at%) consolidated at T_{α} - 235 ˚C showing equiaxed gamma grains with near-gamma to duplex microstructure

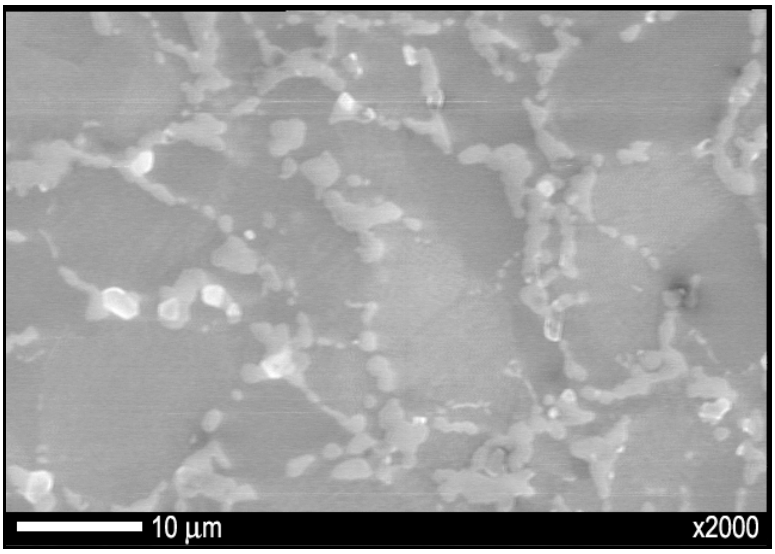

Figure 69: SEM of S4 - Ti-50%Al (at%) consolidated at T_{α} - 235 ˚C showing chopped bands of α_2-Ti_3Al phase segregated at the grain boundaries.

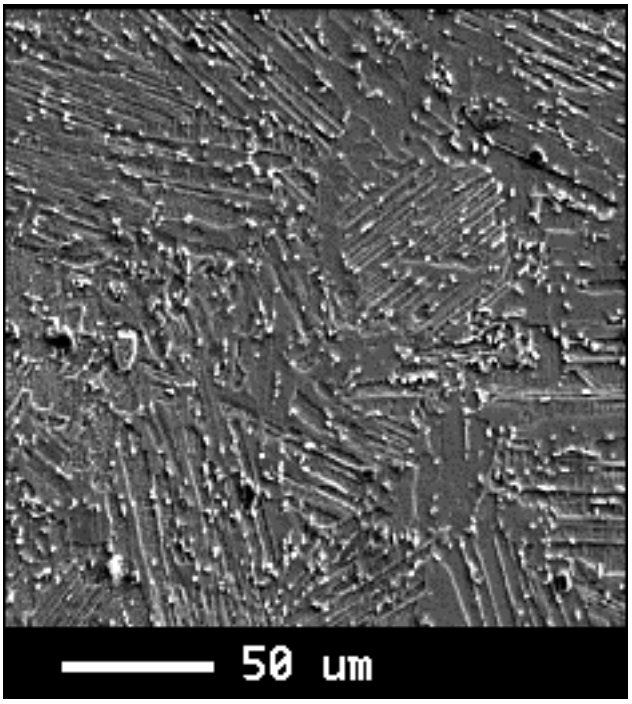

Figure 70: SEM of S6 - Ti-50%Al (at%) consolidated at T_{α} - 35 ˚C showing fully lamellar microstructure

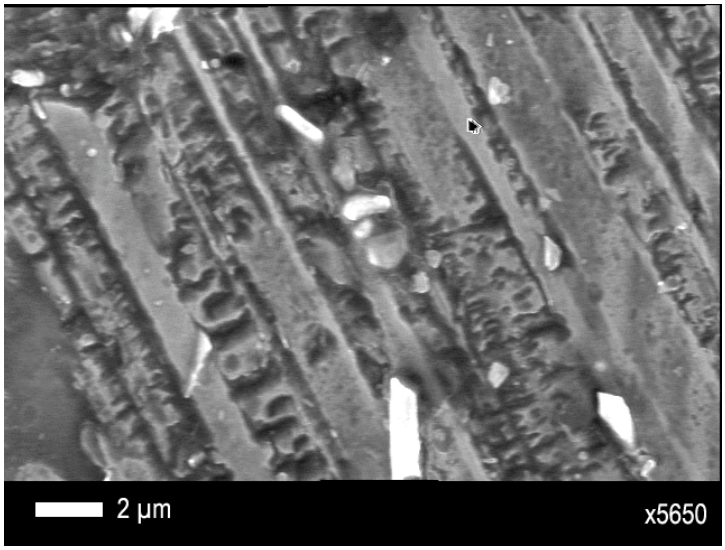

Figure 71: SEM of S6 - Ti-50%Al (at%) consolidated at T_α - 35 $^\circ$C showing lamellar spacing

The reported ultimate tensile strength of γ-TiAl alloys is in the range of 400 – 700 MPa [19; 103; 113; 114], but a direct comparison cannot be made with these values since the values reported in the present work are flexure strengths. The RT flexure strength of T3 samples with duplex microstructure was found to be 30% more superior than that of Ti-50Al alloys consolidated via similar process called pulse discharge sintering [122]. Their ductility was comparable to that of γ-MET TiAl alloys consolidated via HIP [29]. Their fracture toughness of ~18 MPa $m^{1/2}$ was also superior to that of duplex micro-structured TiAl alloys with fracture toughness in the range of 12 - 15 MPa $m^{1/2}$. Similarly sample T4 with fully lamellar microstructure exhibited 40% more ductility than that of fully lamellar TiAl alloys [19; 29, 123]. The microhardness of the consolidated samples is also listed in Table 14. The microhardness values were found to be 20%

lower than the Vickers hardness of γ-MET TiAl alloys consolidated via HIP [29], but were comparable to that of as- cast base Ti-48%Al [160].

The mechanical properties of the consolidated samples were also determined at temperatures up to 1000 ° C. Four-point bending tests were conducted in a high temperature retort system in air and vacuum. Figure 75 shows the comparisons of the flexural strength of sample T3 in air and vacuum.

3.4 Discussion

3.4.1 Microstructure Evolution

Samples T3 and T4 as listed in Table 13 have an alloy composition with small additions of Cr and Nb. Due to these additions, the phase boundaries of these samples were shifted such that the alloy behaved as if it had less Al concentration [108]. As a result the alpha-transus line was shifted to the right as indicated by the dotted line in Figure 64 and the effective alpha-transus temperature was less than that of Ti-50Al alloy in samples S4 and S6. This explains the fact that although samples S4 and T3 were consolidated at the same temperature (1200° C), they have different microstructures as shown in Figure 65 and 68. At 1200 ° C, sample S4 is at T_α - 235 ° C, while that of sample T3 is at T_α - 145 ° C. The consolidation temperature of sample T3 was therefore closer to T_α than that of sample S4. At T_α - 145 ° C, sample T3 was in a phase field where the volume fractions of gamma phase and alpha phase are approximately equal. At this state, the formation of the alpha phase becomes prominent. The initially predominant gamma phase is gradually reduced in volume until equilibrium volume fraction is reached and grain growth occurs. The

growth of grains, however, is limited by the dispersed alpha phase, which also grows. These competitive growth processes result in a fine mixture of two-phase grains with duplex microstructure as shown in Figure 65.

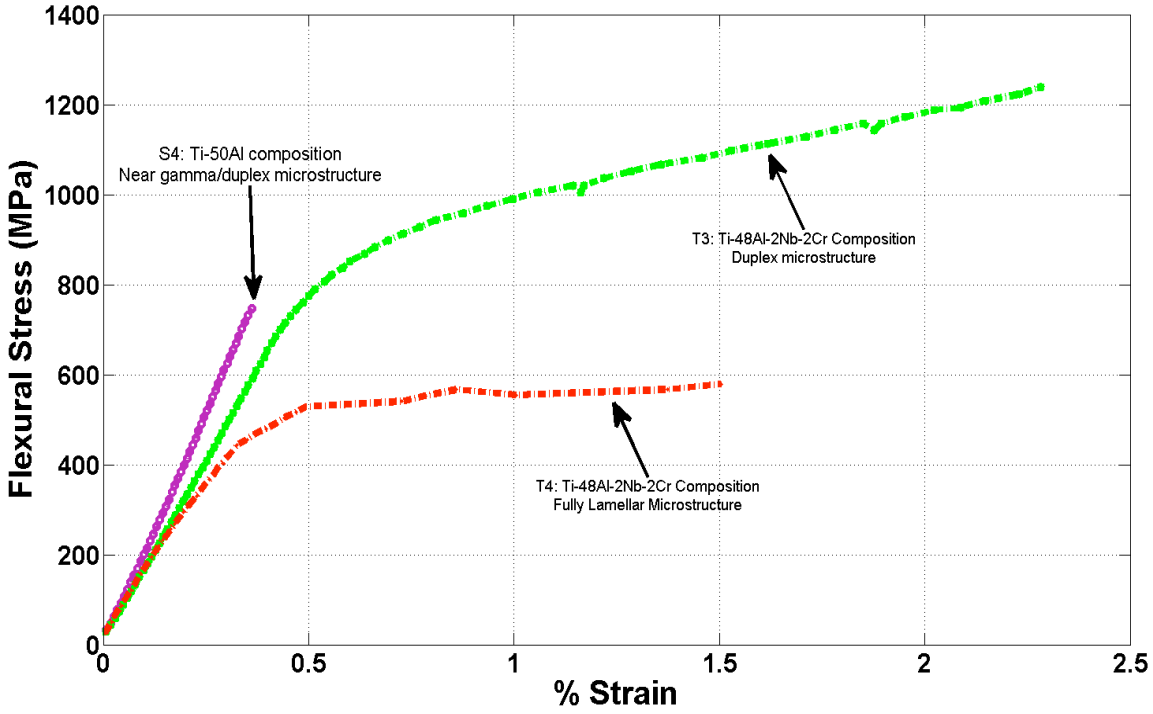

Figure 72: Flexural stress v. tensile strain curves from four-point bending tests of γ-TiAl samples consolidated via P2C.

Sample T4 was consolidated at $T_\alpha + 55^\circ C$ in the pure alpha field, which resulted in the formation of fully lamellar microstructure with large lamellar grains [125] as shown in Figures 66 and 67. The grain growth at temperatures above T_α is high due to the fast diffusivity of the alloy constituents. Therefore, even rapid consolidation at such high temperatures cannot control grain growth in sample T4. Sample S6, which was consolidated at the same temperature as sample T4 did not exhibit rapid grain growth as

sample T4. As shown in Figures 66 and 70, the grain size of sample S6 is between 50μm to 100μm, while that of sample T4 is between 100μm - 2000μm. This is probably due to the addition of Cr in sample T4 which lowered its T_α temperature. Hence, with reference to the T_α temperature, sample T4 was consolidated at $T_\alpha + 55\ ^\circ C$ in pure alpha phase field, while sample S6 was consolidated at $T_\alpha - 35\ ^\circ C$ in the $\alpha + \gamma$ phase field. The presence of the γ phase impeded rapid grain growth in sample S6.

3.4.2 Dependence of Mechanical Properties on Grain Size and Microstructure Type

The mechanical properties of the P2C consolidated samples showed an inverse relationship between grain size and strength as expected from the Hall-Petch relationship. This was shown in chapter II for Ti-50Al samples and is true for the TiAl-2Nb-2Cr samples as well. Sample T3 with a refined duplex microstructure and average grain size of 5μm exhibited flexural strength of 1238 MPa. While the coarse grained fully lamellear microstructure with grain size ranging between 100μm – 2000μm in sample T4 had flexural strength of only 578 MPa.

Table 14: Room temperature mechanical properties of P2C consolidated γ-TiAl samples.

Sample ID	Micro-structure Type	Grain Size (μm)	Elongation (%)	Elastic Modulus (GPa)	Flexural Strength (MPa)	Fracture Toughness (MPa $m^{1/2}$)	Micro-Hardness (GPa)
T3	Duplex	5	2.3	154.48	1238.62	17.95	2.90
T4	Fully Lamellar	100 - 2000	1.5	134.59	578.51	-	2.55
S4	Near-gamma/ Duplex	13	0.3	203.90	746.54	9.43	3.46
S6	Fully Lamelar	50-100	-	-	422.96	-	2.58

3.4.3 Dependence of Mechanical Properties on Alloy Composition

γ-TiAl has been reported to have maximum ductility for Ti-48%Al composition [9; 20; 103]. The decreased ductility with increasing aluminum content is attributed to increased tetragonality ratio or decreased metallic bonding [131]. Additions of Cr increases metallic bonding by decreasing aluminum content in the gamma phase [148]. Therefore, T3 samples with 48%Al and 2%Cr and duplex microstructure exhibited the maximum ductility. For the fully lamellar samples, sample T4 exhibited significantly higher ductility than sample S6. Although, both samples had similar microstructures, the addition of Cr and alloy composition in the Ti-48Al range increased ductility in sample T4.

T3 samples with Ti-48Al-2Cr-2Nb composition and duplex microstructure also exhibited fracture toughness higher than sample S4 with Ti-50Al composition and duplex microstructure as shown in Table 14. The addition of Nb is known to increase strength as well as fracture toughness in gamma titanium aluminides [31] as evidenced here.

3.4.4 High Temperature Mechanical Properties

Figure 75 shows the flexure strength of T3 samples in air and vacuum at high temperatures. As shown in Figure 76 and 77, the T3 samples with (Ti-48Al-2Nb-2Cr composition) perform better than S4 samples (with Ti-50Al composition) at high temperatures.

At test temperatures above 700 $^{\circ}$C, sample T3 was above its brittle-to-ductile transition temperature [105]. With the addition of Cr and temperatures above the brittle-to-ductile transition temperature, the samples exhibited enormous amounts of elongation. As a result, the T3 samples could not be loaded to failure, since the clearance in the four-point bending set-up was not enough to accommodate their deformation to failure. Thus, the flexural stresses shown for T3 samples above 700 $^{\circ}$C in Figures 75, 76 and 77 are the maximum stress values sustained by T3 samples before passing the four-point bending fixture clearance. They do not reflect their failure stress. Nonetheless, the T3 samples fared better than S4 samples at high temperatures.

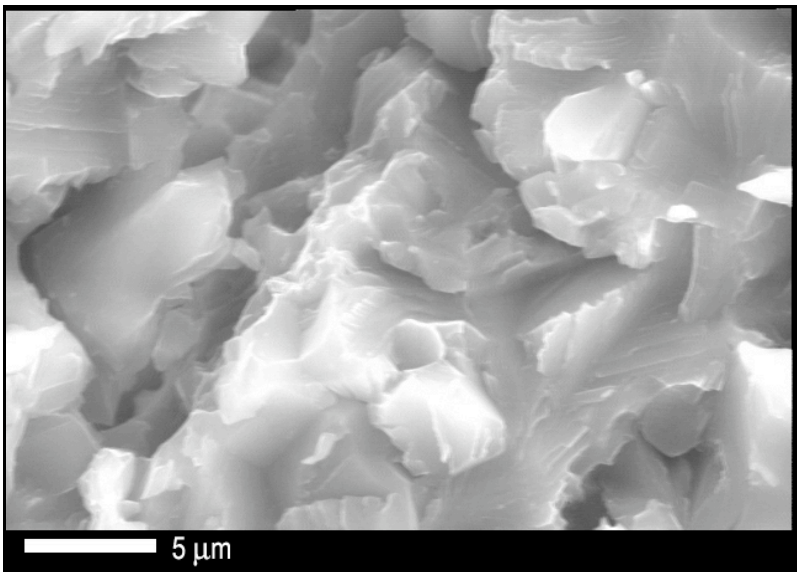

Figure 73: SEM of fractured T3 - Ti-48%Al-2%Cr-2%Nb samples with duplex microstructure

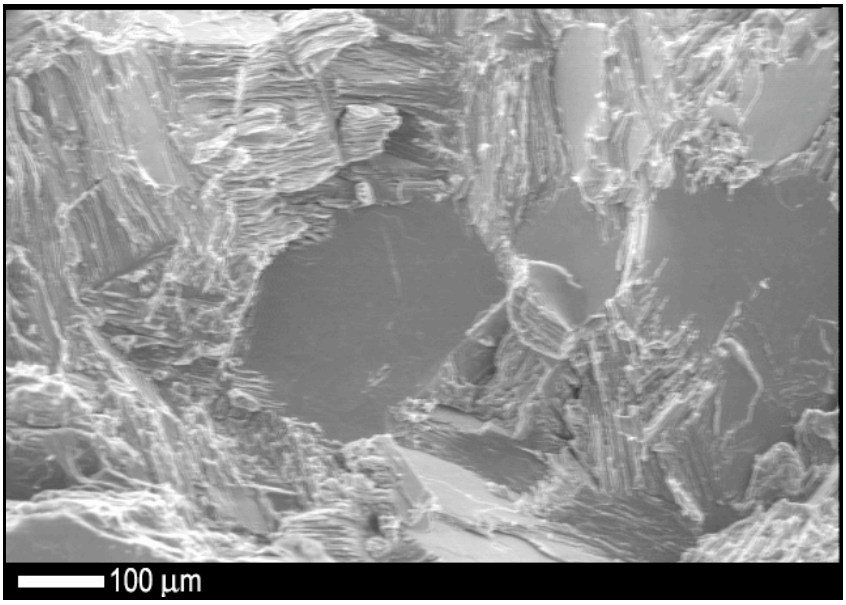

Figure 74: SEM of fractured T4 - Ti-48%Al-2%Cr-2%Nb samples with fully lamellar microstructure

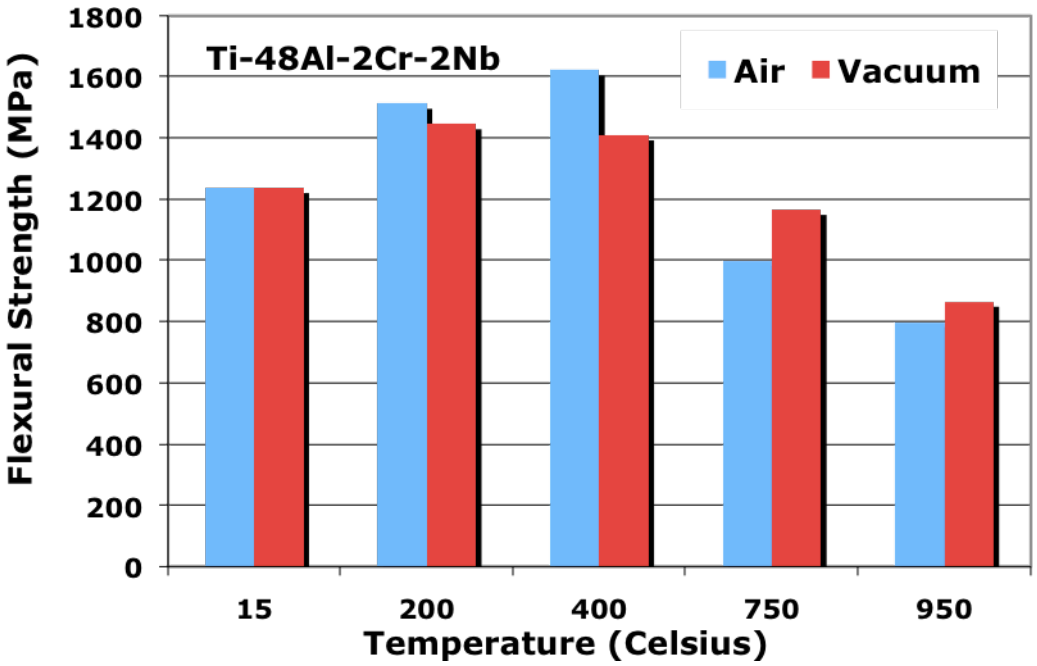

Figure 75: Flexural strength v. temperature for Ti-48Al-2Cr-2Nb (T3)

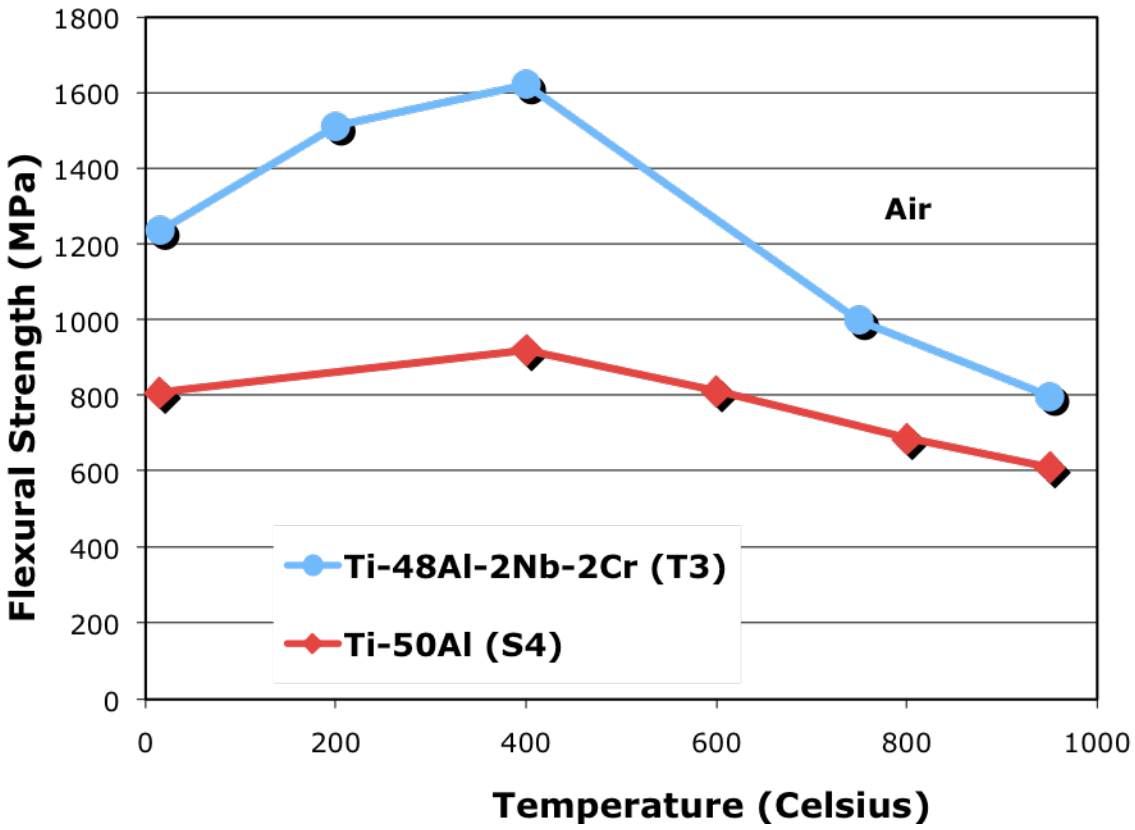

Figure 76: Comparison of flexural strength v. temperature between Ti-48Al-2Cr-2Nb (T3) and Ti-50Al (S4) alloy in air

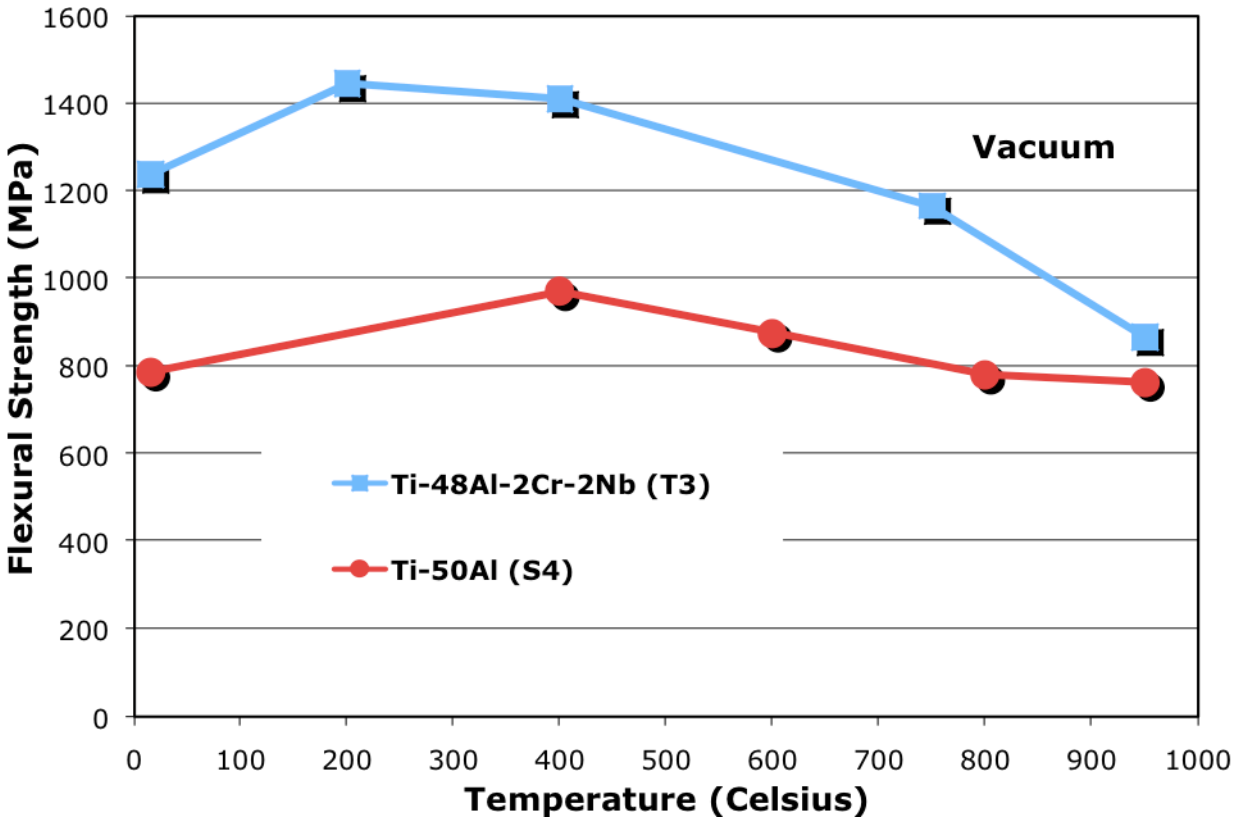

Figure 77: Comparison of flexural strength v. temperature between Ti-48Al-2Cr-2Nb (T3) and Ti-50Al (S4) alloy in vacuum.

3.5 Conclusions

1. γ-TiAl powders of composition Ti-48%Al-2%Cr-2%Nb were rapidly consolidated via Plasma Pressure Compaction at a range of temperatures relative to the alpha-transus temperature to produce samples with duplex and fully lamellar microstructures

2. The grain growth in most microstructures except for the fully lamellar type was controlled to produce microstructures with micron-sized grains.

3. The mechanical properties were found to depend strongly on the microstructure, grain size and alloy composition. γ-TiAl alloy with Ti-48%Al-2%Cr-2%Nb composition and the duplex microstructure was found to exhibit the best set of mechanical properties.

4. The consolidated samples were found to retain good flexural strength up to 1000°C.

Chapter 4: Effect of Attrition Milling on TiAl Powders

4.1 Introduction

The ordered crystal structure of titanium aluminides (TiAl) leads to attractive elevated temperature properties such as high strength and stiffness, and excellent creep and oxidation resistance [76; 92]. These attributes are a result of its limited dislocation motion [41]. In order to preserve the ordered crystallite structure, the dislocations in titanium aluminides have to move in pairs or as superdislocations, which are very sessile. Although these characteristics are very desirable for high temperature applications, but at room temperature these characteristics lead to limited ductility and hence create difficulty in processing and manufacturing of titanium aluminide parts.

The RT ductility and strength of TiAl can be increased by various alloying techniques discussed in chapter III. But along with alloying, decreasing the grain size in the sub-micrometer to nanometer range can lead to significant increase in strength and ductility [20]. Recently, a lot of effort has concentrated on reducing the TiAl grain size by powder metallurgy (PM) routes [68; 76; 77; 78; 85; 89; 91]. In PM techniques, the particle size of the powders can be reduced by attrition milling [85]. This is usually followed by a consolidation technique such as HIP. Along with attrition milling, high energy ball-milling has also been employed to synthesize fine-grained TiAl powders from elemental powders [20; 41; 76; 78; 85]. The advantage of mechanical alloying is that it can be used to synthesize TiAl with different compositions and alloy additions with relative ease. Also, the milling time and milling energy (mill RPM) can be controlled to produce TiAl powders with disordered lattice and reduced particle size. The disordered lattice further

adds to the ductility of the material since the dislocations do not have to move in pairs [88]. But one of the drawbacks of mechanical alloying is contamination of the powders from the milling media and container [85].

As mentioned earlier, several studies have been conducted on the attrition milling or ball-milling of the TiAl powders and its characterization, but few have reported on the consolidation process of the milled powders and the mechanical properties of the consolidated part. Very few researchers have produced consolidated TiAl samples with grain size in the nanometer to sub-micrometer range [76; 92]. Further, there is no data correlating the effects of decreased grain size on the mechanical properties. Some values of micro-hardness, compressive strength and bending strength for TiAl with ultra-fine grain size have been reported but they have not been compared to TiAl parts produced by consolidation of unmilled or as-received powders [68; 127]. Hence, the effect of grain size in the sub-micromenter to nanometer range on the mechanical properties of TiAl has not been fully characterized.

In this study, pre-alloyed TiAl powders produced by gas atomization were milled in an attrition mill. The powders were then rapidly consolidated by plasma pressure compaction (P2C) technique. The microstructure and mechanical properties of the consolidated material was characterized and compared to that of samples consolidated from as-received (un-milled) powders.

The objective of the current effort is to report on γ-TiAl with ultra-fine grain size in the sub-micron range and compare its mechanical properties to that of samples consolidated from as-received/un-milled powders, but under equivalent consolidation conditions.

4.2 Experimental Procedure

-325 mesh (<45 μm) titanium aluminide powders with chemical composition of Ti-50%Al (at%) and Ti-48%Al-2%Cr-2%Nb were procured from ESPI, Inc., Ashland, OR, and Crucible Research, Pittsburgh, PA, respectively. The powders were ball-milled with ¼" Carbon Steel media with a ball-to-powder ratio of 10:1 (by weight) in a 750 ml stainless steel tank with Tungsten arms at 600 RPM in an attrition ball mill. The Ti-50Al composition powders were ball-milled for 5 hours, while the powders with Ti-48Al-2Cr-2Nb composition were ball-milled for 8 hours. For the powders with Ti-50Al composition, the milling was done on two batches of powder. One batch was milled without any process control agents (PCAs), while the other was milled with 2 wt% stearic acid added as a PCA. For powders with Ti-48Al-2Cr-2Nb composition, milling was done with 2 wt% stearic acid acting as a PCA. The milling parameters are listed in Table 15.

Table 15: Milling parameters for TiAl powders

Milling Parameters	**Ti-50Al**	**Ti-48Al-2Cr-2Nb**
Media	¼" Carbon Steel	¼" Carbon Steel
Vial	Stainless Steel	Stainless Steel
Ball-To-Powder Ratio (By Weight)	10:1	10:1
PCA	One Batch Without PCA, Other With 2% (Wt%) Stearic Acid	2% (wt%) Stearic Acid
Milling Time (Hrs)	5	8

Powders milled without a PCA (stearic acid) were found to be cold welded to the vial and could not be scraped off easily. Hence, no further processing or characterization of these powders was performed.

The powders milled with stearic acid did not stick to the vial surface and were easy to remove from the vial. The Ti-50Al composition powder was easy to handle and was characterized by X-ray diffraction, scanning electron microscopy, and surface area measurements. The powders with Ti-48Al-2Cr-2Nb composition were found to be extremely pyrophoric and hence could not be characterized for their particle size and phase. These powders were handled in an Argon filled glove box for loading them in the graphite dies for consolidation.

Powders milled with stearic acid as a PCA were consolidated into a one-inch diameter disc of ¼-inch thickness. Approximately 13 grams of powder was loaded into a graphite die (25 mm ID) with plungers inserted on top and bottom side. The assembly was then placed between two water-cooled electrodes. The upper electrode was lowered on the top graphite plunger using a hydraulic cylinder to hold the entire assembly together in compression and provide a path for current flow. When sufficient inter-particle contact was established by applying uniaxial pressure of 54 MPa, pulsed DC voltage was applied through the powder compact using a full-wave-rectified power.

The pulsed electrical power was applied with high current at an adequate voltage. This leads to charge build up at inter-particle gaps. This causes one particle to be charged negatively with respect to particle in contact with it. As the charge accumulates, the voltage difference becomes sufficiently large to generate sparks that trigger an ionization

process. The ions move towards the negatively charged particles while the electrons move toward the positively charged particles. The ionization process occurs in the form of sparks or plasma generation depending on the energy level at the inter-particle gap. The formation of plasma at the inter-particle boundaries removes oxides and other contaminants, which form a diffusion barrier in the consolidation process. As a result particle re-arrangement and diffusion is enhanced.

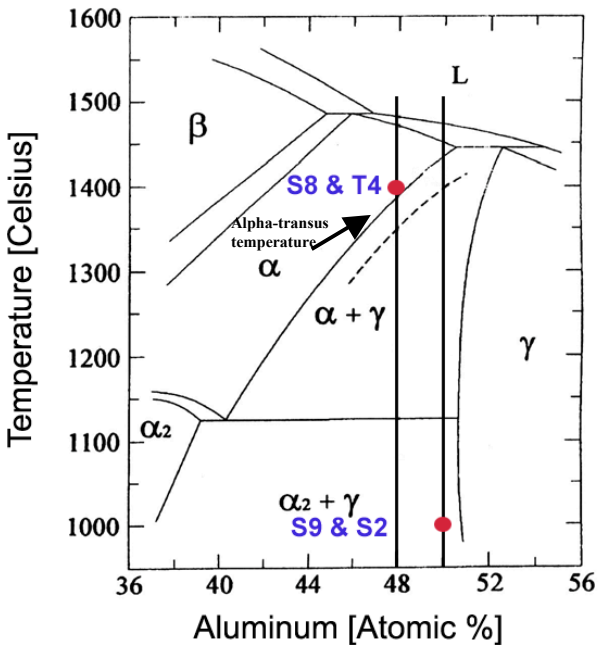

Figure 78: Partial Ti-Al binary phase diagram near the stoichiometric γ-TiAl composition [108].

After pulsing for 20 minutes, direct current was applied through the powder compact resulting in Joule heating. Consolidation was carried in vacuum at 1000^{o}C for powders with Ti-50Al composition and at 1400^{o}C for powders with Ti-48Al-2Cr-2Nb

composition. The consolidation temperatures of 1000°C and 1400°C are equivalent to T_α - 300°C and T_α + 55°C respectively. T_α is the alpha-transus temperature of TiAl above which TiAl exists in pure α field as shown in Figure 78. The T_α was estimated to be in the range of 1425°C to 1450°C from the binary phase diagram of TiAl in Figure 78. For Ti-48Al-2Cr-2Nb, the T_α temperature was approximated to be 1345°C. Addition of Nb contracts the α field and reduces the alpha-transus temperature [19; 25; 30; 61]. The consolidation conditions for both milled and as-received Ti-50Al and Ti-48Al-2Cr-2Nb samples are listed in Table 16. The samples prepared from the as-received powders were also discussed in chapters II and III.

Table 16: Consolidation conditions for milled TiAl powders

TiAl Composition (at%)	Sample ID	Pressure (MPa)	Temperature (Celsius)	Pulsing
Ti-50Al (milled – 5hrs)	S8	54	1000	Yes
Ti-50Al (as-received)	S2	54	1000	Yes
Ti-48Al-2Cr-2Nb (milled – 8hrs)	S9	54	1400	Yes
Ti-48Al-2Cr-2Nb (as-received)	T4	54	1400	Yes

The consolidated samples were sectioned and metallographically polished to 1 μm diamond finish. They were subsequently etched via Kroll's agent. Their microstructure was characterized via Scanning Electron Microscopy (SEM) and Energy Dispersive

Spectroscopy (EDS). The SEM and optical micrographs were taken in the orientation perpendicular to the direction of compaction.

The powder particle size of the milled TiAl was calculated from surface area measurements, X-ray diffraction (XRD), and Transmission Electron Microscopy (TEM). The mechanical properties of the consolidated specimens were characterized using four-point bending tests. A self-aligning silicon carbide four-point bending fixture was designed according to ASTM standard C 1161 [109] with an outer-span of 20 mm and an inner-span of 10 mm. Consolidated samples were machined with chamfered edges to a dimension of 25 mm x 1.5 mm x 2.0 mm according to ASTM standard C 1161. Samples with dimension of 3 mm x 4 mm x 25 mm with a 60 degree chevron notch were also tested according to ASTM standard C 1421 in the four-point bending set-up to measure fracture toughness. All tests were conducted at a strain rate of 0.75×10^{-4} in a Material Testing Systems (MTS) model 810 machine. The four-point bending tests were conducted at temperatures up to 1000^{o}C. The high temperature tests were conducted in air and vacuum (10^{-5} Pa). The four-point bending test samples were loaded such that the resultant tensile and compressive stresses were in the direction perpendicular to that of the direction of the compaction. Micro-hardness of the consolidated samples was obtained on polished specimens using a diamond Vickers indent under a load of 1000 grams with a dwell time of 15 seconds.

For four-point bending tests performed at room temperature, the load and displacement data was used to calculate the elastic modulus of the material, as well as the elongation and flexural strength. More details about the mechanical test procedure and analysis are elaborated in chapter II.

To ensure the accuracy of the four-point bending test data, "control" samples prepared from AD998 aluminum oxide obtained from CoorsTek, Golden CO., were also tested. The strength and fracture toughness of the AD998 samples were in excellent agreement with those reported by CoorsTek as shown in chapter II.

4.3 Results

Coulter SA3100 BET surface area measurement unit was used to calculate the particle size of the as-received Ti-50%Al powders and Ti-50%Al powders milled with a PCA. By assuming spherical shape of the particles, the powder particle size was estimated from the surface area measurements. As shown in Table 17, the milling of the powders led to a reduction in average particle size by 60%.

Table 17: Ti-50%Al (at%) powder particle size measurements

Powder	Average Particle Size (μm)
As-received Ti-50%Al Powders	3.668
Milled Ti-50%Al Powders	1.488

This is further shown in the scanning electron micrographs of the as-received and milled Ti-50%Al powders in Figure 79. The powder particles were highly agglomerated after milling and showed a considerable size reduction.

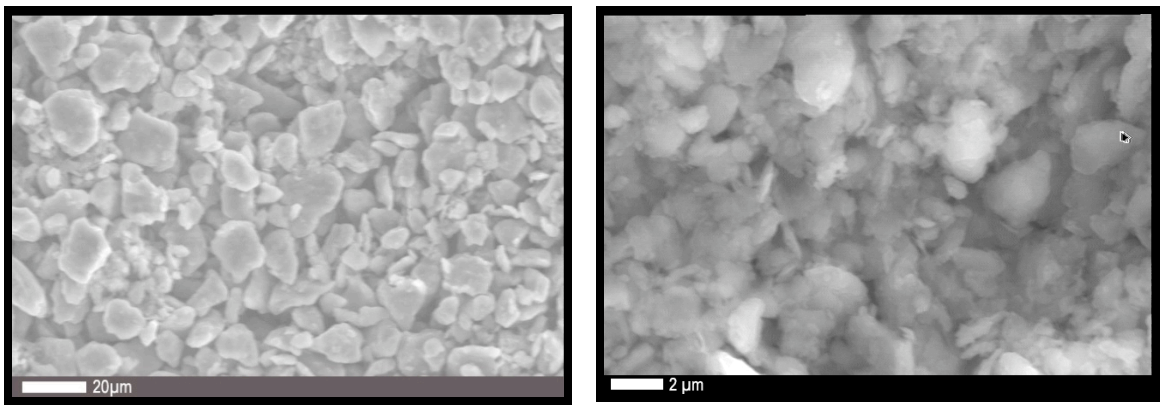

a) **b)**

Figure 79: Scanning electron micrographs of a) as-received Ti-50%Al powders, and b) Ti-50%Al powders milled for 5 hrs with PCA

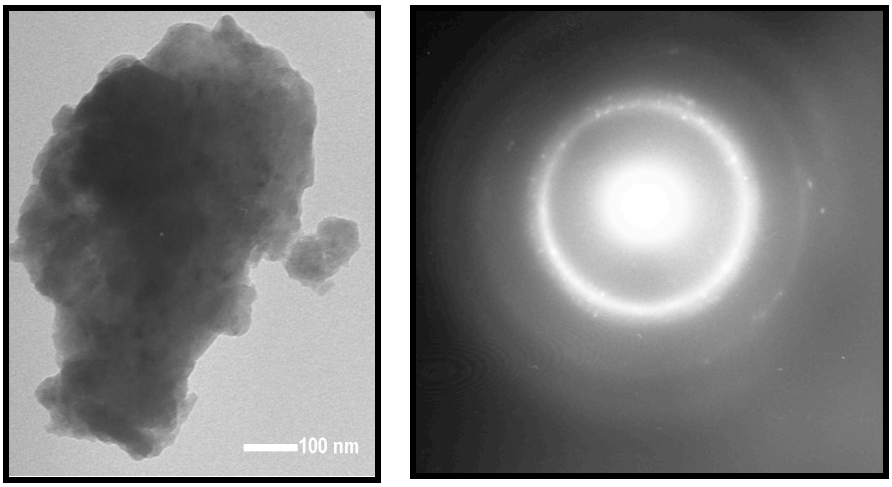

a) **b)**

Figure 80: a) Transmission electron micrograph of milled Ti-50%Al powder with b) selected area diffraction

The TEM image of the milled Ti-50%Al powder is shown in Figure 80. The powder appeared highly agglomerated due to the milling size. The selected area diffraction showed a ring feature with spots, which confirmed a crystalline phase. Figure 81 shows the results of XRD performed on the as-received and milled powder. The as-received powder used for X-ray diffraction was not from the same vendor as milled powder, but was of the same composition (i.e Ti-50%Al) and same mesh size (i.e -325 mesh). The diffraction peaks of the milled powder showed a broadened character, which is characteristic of heavy deformation and formation of small crystallites due to milling. The standard powder diffraction peak positions of the γ-TiAl and α_2-Ti_3Al with relative intensity represented by the height of the vertical lines are also plotted in Figure 83.

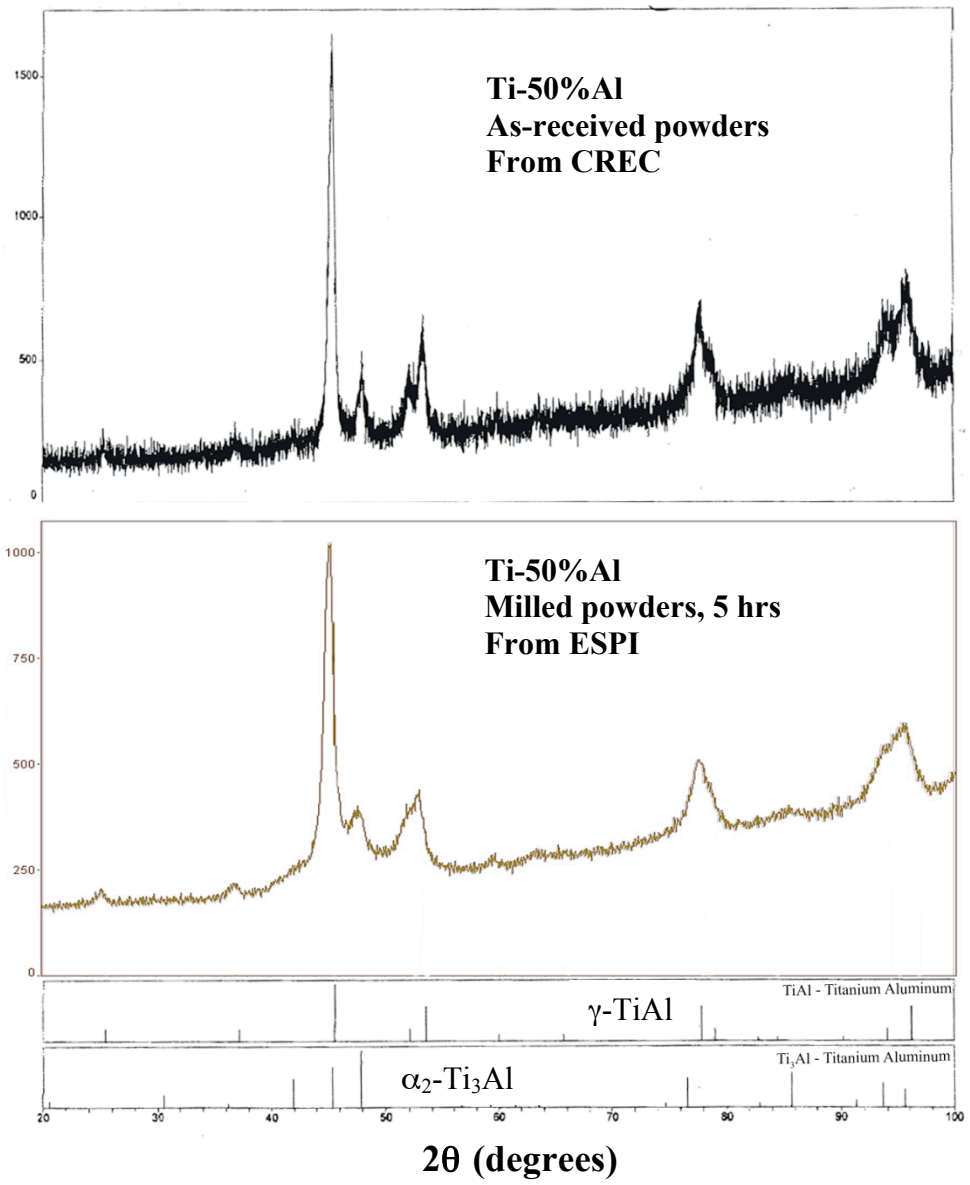

Figure 81: X-ray diffraction of as-received and milled Ti-50%Al powders

The scanning electron micrograph (SEM) of the sample consolidated from as-received Ti-50%Al powders is shown in Figure 82. This sample was consolidated under the same conditions as the milled Ti-50%Al as indicated in Figure 78 and Table 15. The average grain size of sample S2 in Figure 82 was found to be 10μm. The

SEM of sample (S8) consolidated from milled Ti-50%Al powders is shown in Figure 83. The average grain size for this sample was found to be significantly lower than that of sample S2 and was in the range of 1μm.

Ti-48Al-2Cr-2Nb composition powders, which were milled for 8 hours could not be characterized by XRD, SEM, and TEM due to their pyrophoric nature. Hence, these powders were directly consolidated into 1" diameter disc sample (S9). SEM of the consolidated sample from as-received Ti-48Al-2Cr-2Nb without undergoing milling process is shown in Figure 84. In this case, the fully lamellar microstructure was characterized with coarse grains, whose size ranged from 200μm to 1000μm.

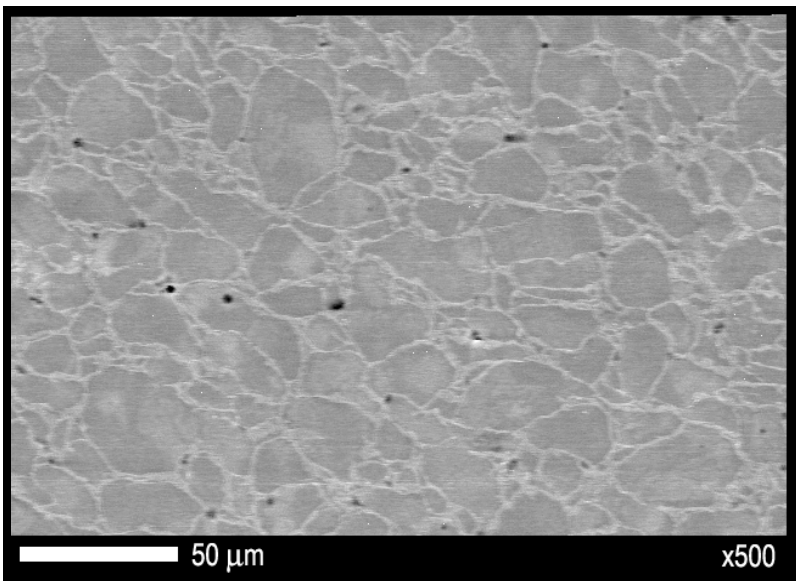

Figure 82: SEM of sample (S2) consolidated from as-received Ti-50%Al powders

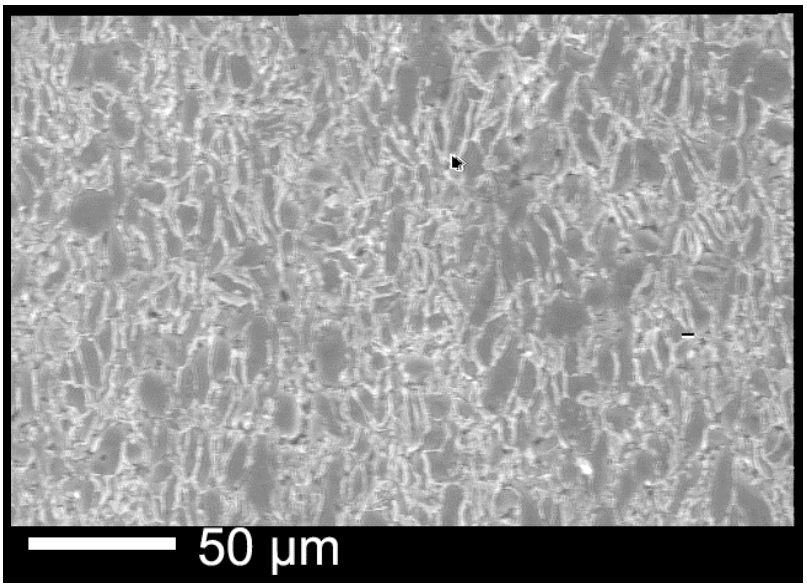

Figure 83: SEM of sample (S8) consolidated from milled Ti-50%Al powders

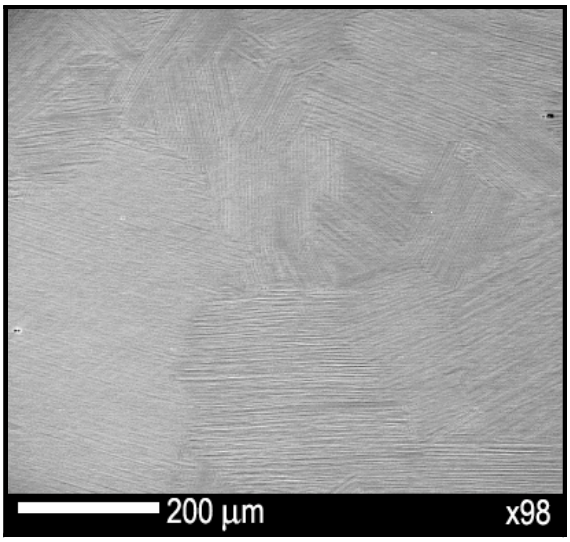

Figure 84: SEM of sample (T4) consolidated from as-received (unmilled) Ti-48Al-2Cr-2Nb powders

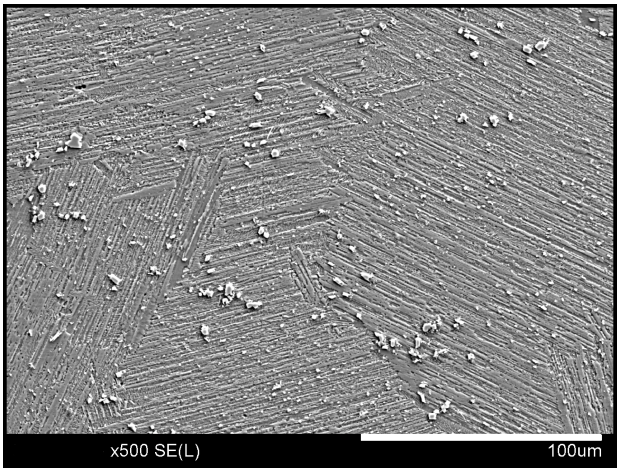

Figure 85: SEM of sample (S9) consolidated from milled (8hrs) Ti-48Al-2Cr-2Nb powders

Figure 85 shows the SEM of the sample (S9) consolidated from the milled Ti-48Al-2Cr-2Nb powders. The microstructure was fully lamellar with an average grain size of 100µm. The microstructure did not show any coarse grains in the size range of 200µm to 1000µm as was seen in sample T4.

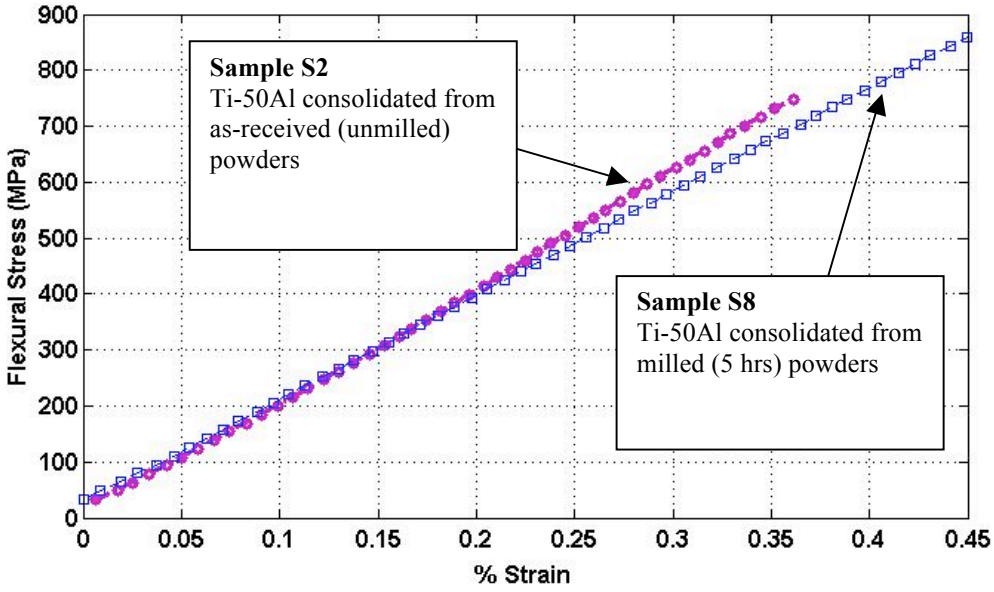

Figure 86: Four-point bending test results for Ti-50Al samples consolidated from milled and un-milled powders

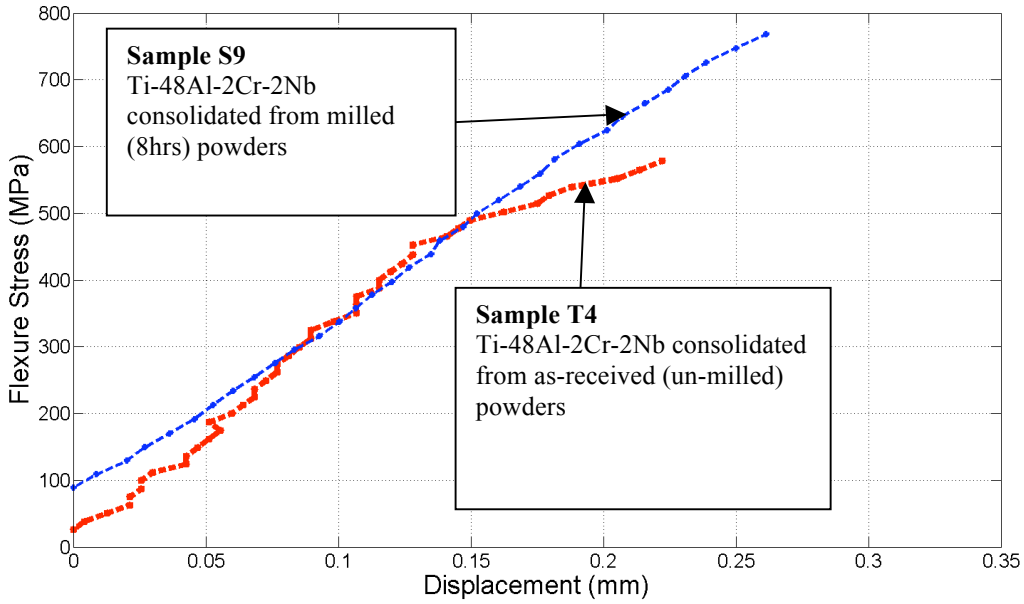

Figure 87: Four-point bending test results for Ti-48Al-2Cr-2Nb samples consolidated from milled and un-milled powders

The mechanical properties of the consolidated samples were characterized by four-point bending tests as mentioned earlier. Figure 86 shows the stress v. strain plot for both Ti-50Al samples consolidated from milled and un-milled powders. As expected, the Ti-50Al sample (S9) consolidated from milled powders had superior strength compared to sample (S2) consolidated from as-received (un-milled) powders. The increase in strength is due to decrease in grain size as demonstrated by the Hall-Petch relationship [36; 37; 39].

Similarly the four-point bend test was performed on samples consolidated from Ti-48Al-2Cr-2Nb powders in both milled and un-milled conditions. The load v. displacement plot is shown in Figure 87. The samples consolidated from milled Ti-48Al-2Cr-2Nb powders showed higher strength due to smaller grain size.

4.4 Discussion

The Ti-50Al powder was milled for 5 hours with a PCA (stearic acid) and its average particle size was reduced by 60%. The powder milled without PCA was cold welded to the surface of the vial and was not available for further characterization or consolidation. The Ti-50%Al powder milled for 5 hours was found to restore the same phases present in the as-received powder as shown in the X-ray diffraction results in Figure 81. Hence, no phase transformation was observed, only powder particle size was reduced.

Sample S8 consolidated from milled Ti-50Al powders (5 hours) had fine γ grains with α_2 bands segregated at the grain boundaries. This was similar to the microstructure of sample S2, which was consolidated from the as-received Ti-50Al powders. Both the samples S2 and S8 were consolidated at T_α-300^{o}C (1000^{o}C) in the $\alpha_2 + \gamma$ phase field. The microstructure was characterized as near-gamma. As expected, due to the smaller particle size of the milled powders before consolidation, the grain growth in S2 was significantly lower than that in S8. Hence, a significant decrease in grain size to the sub-micrometer level was achieved. The benefits of the decreased grain size can be seen in Figure 86, where the flexural stress and elongation of sample S8 (average grain size = 1μm) showed a marked improvement compared to that of sample S2 (average grain size = 10μm).

The samples S9, and T4 consolidated from milled and as-received (un-milled) Ti-48Al-2Cr-2Nb powders, respectively displayed a fully lamellar microstructure. Both the samples were consolidated in the pure α phase field. Diffusion in α phase field is very rapid and therefore grain growth is hard to control. Hence, highly coarse

grains in the range of 200μm to 1000μm were seen in sample T4. The grain growth in sample S9 (average grain size = 100μm) was controlled to a considerable extent by reducing the powder particle size via milling. The difference in grain size in the two samples resulted in enhanced mechanical properties for sample S9 as seen in Figure 87.

4.5 Summary and Conclusions

Micron-sized Ti-50%Al and Ti-48%Al-2%Cr-2%Nb (at%) powders were attrition milled to reduce the powder particle size. The milled powders were rapidly consolidated to produce one inch diameter disc samples. The consolidated samples were characterized for their microstructure and mechanical properties and were compared to that of samples consolidated from as-received (unmilled) powders. The following conclusions were made from the characterization of the consolidated samples and milled powders

1. Ti-50%Al powders were milled for 5 hours with and without a PCA (stearic acid). The Ti-50%Al powders milled without a PCA were cold-welded to the surface of the vial and were unavailable for further characterization or consolidation.

2. Ti-50%Al powders milled with a PCA were characterized for size and phase. The average particle size of the powders was reduced by 60% after milling for 5 hours. No change in the phase of the powders was observed after milling.

3. Ti-48%Al-2%Cr-2%Nb powders milled for 8 hours were found to be extremely pyrophoric and hence could not be characterized prior to consolidation.

4. The Ti-50%Al samples consolidated in the $\alpha_2+\gamma$ phase field from powders milled for 5 hours with stearic acid were found to exhibit near-gamma microstructure composed of fine gamma grains and bands of α_2-Ti_3Al precipitates segregated at the grain boundaries. The average grain size was found to be 1μm.

5. Samples consolidated from Ti-48%Al-2%Cr-2%Nb powders milled for 8 hours were found to exhibit fully lamellar structure with average grain size in the range of 100μm. Since, the sample was consolidated in the pure α phase field, diffusion and grain growth was rapid. The grain size in samples consolidated from as-received (un-milled) Ti-48%Al-2%Cr-2%Nb powders was significantly higher and was in the range of 200μm to 1000μm. Hence, the reduction of powder particle size before consolidation was helpful in producing a more refined fully lamellar structure.

6. As expected, the mechanical properties for both Ti-50%Al and Ti-48%Al-2%Cr-2%Nb samples consolidated from milled powders showed a marked

improvement in terms of flexure stress and elongation as compared to that of samples consolidated from as-received powders.

Chapter 5: Microstructure and Mechanical Properties of TiB-Reinforced Titanium Alumnides

5.1 Introduction

The attractive high temperature mechanical properties of dual phase titanium aluminides (TiAl) have an inverse relationship with its room temperature ductility. Several attempts have been made to increase the RT ductility of TiAl by small additions of metallic elements such as Cr, V, and Mn in the range of 2% (at%) [19; 37]. Although, these elements have been shown to increase the RT ductility, they adversely affect the high temperature creep and oxidation resistance of the material [19]. Additions of Nb in the range of 5% to 10% (at%) has shown an increase in the RT ductility as well as the strength of TiAl along with good retention of creep and oxidation resistance at temperatures up to 800^{o}C [8; 30; 61]. But retention of these properties at temperatures above 900^{o}C, while maintaining acceptable RT ductility has been found to be difficult.

Several interstitial elements such as C, O, N, and B have been added to TiAl alloys to increase their performance over a higher temperature range [74]. Oxygen has been found to increase the high temperature creep and oxidation resistance due to the formation of Al_20_3 precipitates at high temperatures. But oxygen significantly lowers the RT ductility of TiAl [35].

Adding carbon results in the formation of TiC, Ti_3AlC and Ti_2AlC precipitates depending on the heat-treatment and processing of a TiAl-C system [54; 74, 128; 129;

130]. Addition of C has demonstrated an increase in micro-hardness as well as creep resistance [74]. The effect of C additions on the RT ductility has not yet been reported but it is expected to decrease the RT ductility of TiAl due to the brittle nature of TiC and the known fact that dispersion strengthening is the primary strengthening mechanism reported in TiAl-C based composites.

Similarly, the addition of nitrogen leads to the formation of TiN precipitates in the TiAl matrix, which also have led to better strength retention and creep resistance at high temperatures. But the TiAl-N based composite still lacks room temperature ductility.

Composites based on TiAl-B system have been developed over the past several years and has led to the development of the XD^{TM} TiAl composites [66; 98; 131]. These composites contain 5 to 7 vol% of TiB_2 needle-like discontinuous dispersions with the composition of Ti-(45to47)Al-2Mn-2Nb (at%) + 5 to 7 vol% of TiB_2. Boron acts as a grain refiner and provides dispersion strengthening for TiAl alloys. As a result, the ductility, strength as well as oxidation resistance of a TiAl + TiB_2 composite were found to be superior to TiAl alloys.

The XD™ process utilizes an Al–TiB_2 master alloy material, which when added to the base TiAl alloy melt, produces a fine dispersion of TiB_2 particles [66; 67; 131; 132]. The XD^{TM} process has been applied to cast TiAl alloys and has shown enhanced performance at high temperatures. As with any casting process the post-processing of XD^{TM} cast TiAl +TiB_2 composite requires Hot-Isostatic Processing (HIP) to close pores and attain a homogeneous microstructure. After HIP, the cast ingots are usually heat-treated and machined into the desired shapes.

Powder metallurgy (PM) has always been considered as an alternative route to casting especially for obtaining near-net shape parts with minimal post-processing. Mechanical alloying (MA) techniques have been widely investigated to produce TiAl powders of desired composition with small alloying additions [76; 89; 90]. The MA produced powders can be consolidated by relative ease to produce the desired TiAl alloy composite system.

With this approach in mind a TiAl based composite system can be produced by synthesizing the composite powder via MA or by merely blending the pre-alloyed matrix and reinforcement powders followed by consolidation. Several studies have been conducted with this processing route for Ti-alloys, where Ti and TiB_2 powders were mixed and consolidated [133; 134; 135]. The resulting composite system of Ti + TiB is synthesized with this approach. The affinity of B to react with Ti and form TiB, and the thermodynamic equilibrium between Ti and TiB results in the formation of Ti matrix reinforced with discontinuous TiB particulates.

TiB is thermodynamically stable with Ti and does not form any oxide interfaces between the matrix and reinforcement. Also, its coefficient of thermal expansion is very close to that of Ti and TiAl. TiB is also fairly soft and ductile compared to that of TiB_2. Hence, a TiAl+TiB composite system has a potential of being more ductile than TiAl + TiB_2. The thermodynamic equilibrium between Ti and TiB makes the TiAl+TiB system easier to synthesize by a rapid consolidation process. TiB is a line compound and by itself is very unstable. It is not readily available and hence as mentioned above Ti+TiB composite system is synthesized using pre-alloyed Ti and

TiB_2 powders. A similar approach is used in this study, where pre-alloyed TiAl and TiB_2 powders are used to synthesize a TiAl+TiB composite system.

In this study, pre-alloyed gas atomized Ti-48Al-2Cr-2Nb (at%) powders and TiB_2 were mixed in an attrition mill and consolidated by a rapid consolidation process to produce a TiAl + TiB composite system. As shown in Figure 88, TiB and Ti are in thermodynamic equilibrium. Hence, the final composite system was expected to be composed of TiAl matrix reinforced with discontinuous particulates of TiB.

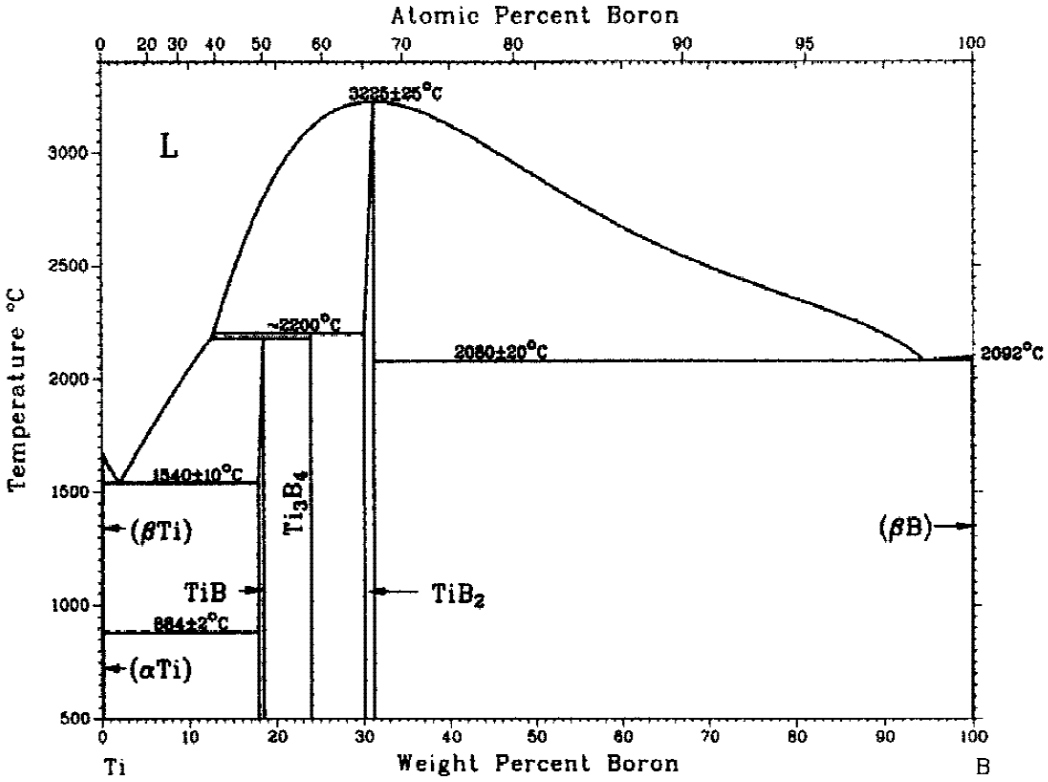

Figure 88: Ti-B phase diagram [133]

5.2 Experimental Procedure

-325 mesh (<45 μm) titanium aluminide powders with chemical composition of Ti-48%Al-2%Cr-2%Nb were procured from Crucible Research, Pittsburgh, PA. TiB_2 powders with average particle size of 2.5μm were procured from H.C. Starck GmbH and Co., Goslar, Germany. The TiAl and TiB_2 powders were blended at 230 RPM in an attrition mill with a 750 ml stainless steel tank with Tungsten arms. The powders were blended till the color of the powder was uniform and did not show any further changes. This was observed after ten minutes of milling. The powders were blended in two batches; the first batch of powder was mixed with 14 wt% of TiB_2, while the second batch was mixed with 24 wt% of TiB_2. These quantities were selected so that the resulting TiB particulates in the TiAl matrix would be 10 vol% and 20 vol%.

The blended powders were consolidated into a one-inch diameter disc of ¼-inch thickness. The powder composition and the consolidation conditions are listed in Table 18. Approximately 13 grams of powder was loaded into a graphite die (25 mm ID) with plungers inserted on top and bottom side. The assembly was then placed between two water-cooled electrodes. The upper electrode was lowered on the top graphite plunger using a hydraulic cylinder to hold the entire assembly together in compression and provide a path for current flow. When sufficient inter-particle contact was established by applying uniaxial pressure of 30 MPa, pulsed DC voltage was applied through the powder compact using a full-wave-rectified power.

Table 18: Powder composition and consolidation conditions for Ti-48Al-2Cr-2Nb (at%), and TiB_2 powder blend.

Sample ID	TiB_2 Powder (wt%)	Expected TiB (vol%)	Consolidation Time (mins)	Consolidation Temperature (Celsius)
M1	14	~10%	20	1250
M2	24	~20%	20	1250

The pulsed electrical power was applied with high current at an adequate voltage. This leads to charge build up at inter-particle gaps. This causes one particle to be charged negatively with respect to particle in contact with it. As the charge accumulates, the voltage difference becomes sufficiently large to generate sparks that trigger an ionization process. The ions move towards the negatively charged particles while the electrons move toward the positively charged particles. The ionization process occurs in the form of sparks or plasma generation depending on the energy level at the inter-particle gap. The plasma removes oxides and other contaminants, which form a diffusion barrier in the consolidation process. As a result particle re-arrangement and diffusion are enhanced.

After pulsing for 20 minutes, direct current was applied through the powder compact resulting in Joule heating. Consolidation was conducted under a vacuum at 1250^{o}C. The consolidation temperature of 1250^{o}C is equivalent to T_{α} - 95^{o}C. T_{α} is the alpha-transus temperature of TiAl above which TiAl exists in pure α field as shown in Figure 91. Addition of Nb contracts the α field and reduces the alpha-

transus temperature [19; 25; 30; 61]. Hence, the T_α for Ti-48Al-2Cr-2Nb was approximated to be 1345^{o}C, slightly lower than the binary Ti-Al alloy.

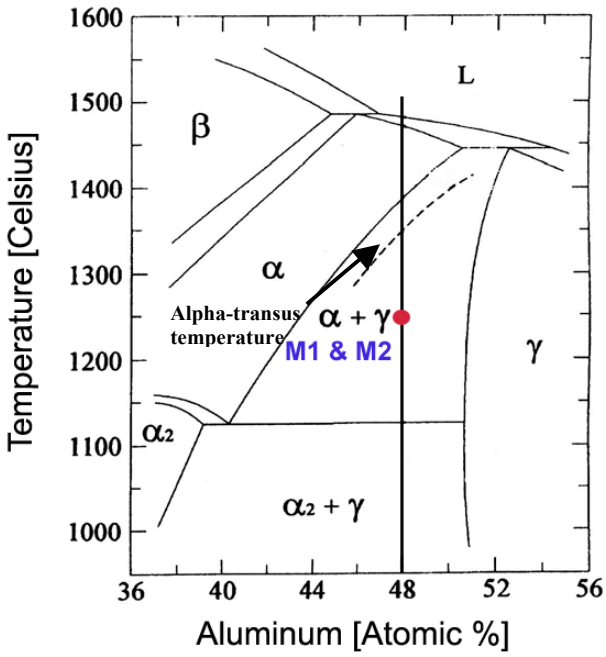

Figure 89: Partial Ti-Al binary phase diagram near the stoichiometric γ-TiAl composition [108]

The consolidated samples were sectioned and metallographically polished to 1 μm diamond finish. They were subsequently etched using Kroll's agent. Their microstructure was characterized usin Scanning Electron Microscopy (SEM) and Energy Dispersive Spectroscopy (EDS). The SEM and optical micrographs were taken in an orientation that was perpendicular to the direction of compaction.

The mechanical properties of the consolidated specimens were characterized using four-point bending testing. A self-aligning silicon carbide four-point bending fixture

was designed according to the ASTM standard C 1161 [109] with an outer-span of 20 mm and an inner-span of 10 mm. Consolidated samples were machined with chamfered edges to a dimension of 25 mm x 1.5 mm x 2.0 mm according to the ASTM standard C 1161. Samples with dimension of 3 mm x 4 mm x 25 mm with a 60 degree chevron notch were also tested according to ASTM standard C 1421 in the four-point bending set-up to measure fracture toughness. All tests were conducted at a strain rate of 0.75×10^{-4} in a Material Testing Systems (MTS) model 810 machine. The four-point bending tests were conducted at temperatures up to 1000^{o}C. The high temperature tests were conducted in air and vacuum (10^{-5} Pa). The four-point bending test samples were loaded such that the resultant tensile and compressive stresses were in the direction perpendicular to that of the direction of the compaction.

The load and displacement data was used to calculate the elastic modulus of the material, as well as the elongation and flexural strength. More details about the mechanical test procedure and analysis are elaborated in chapter II.

To ensure the accuracy of the four-point bending test data, "control" samples prepared from AD998 aluminum oxide obtained from CoorsTek, Golden CO., were also tested. The strength and fracture toughness of the AD998 samples were in excellent agreement with those reported by CoorsTek.

5.3 Results

The scanning electron micrographs (SEM) for the consolidated samples M1 (10 vol% TiB), and M2 (20 vol% TiB) are shown in Figure 90 and Figure 91 respectively. The SEM revealed a fine TiAl matrix reinforced with elongated plate like titanium

boride particles. In order to ascertain the type/composition of the titanium boride, energy dispersive spectroscopy was performed on the titanium boride particles. The titanium boride phase was determined to be TiB based on the EDS results (Figure 92).

The TiB particles were agglomerated in several areas of the TiAl matrix to form equiaxed plate like structures. Voids were found at the interface between the agglomerated TiB structures and the TiAl matrix. The density of the consolidated samples were measured and compared to that of the expected theoretical density of the composite. Based on this, the sample M1 (10 vol% TiB) was found to be 94% dense, while sample M2 (20% vol Tib) was found to be 90% dense.

The TiAl matrix with Ti-48Al-2Cr-2Nb composition in both the samples was characterized with a fine duplex microstructure consisting of equiaxed gamma grains and lamellar structures composed of the gamma and alpha-2 phase. The average grain size was determined to be 3μm. The grain size of Ti-48Al-2Cr-2Nb sample with no TiB reinforcement was 5μm as shown in Figure 93. This sample was consolidated at conditions equivalent to that of the M1, and M2 TiAl + TiB composite samples.

The mechanical properties of the TiB reinforced TiAl matrix were characterized and compared to that of TiAl matrix with no TiB reinforcement. The stress v. displacement plot for the two TiB reinforced TiAl samples M1 and M2 with 10 vol% and 20 vol% of TiB respectively is shown in Figure 94. These plots are compared to that of sample T4 with the same TiAl composition as sample M1 and M2 but with no TiB reinforcement.

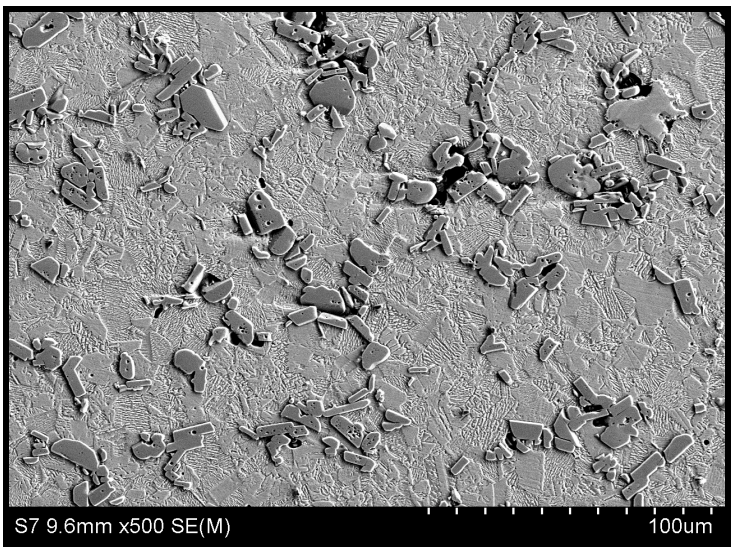

a)

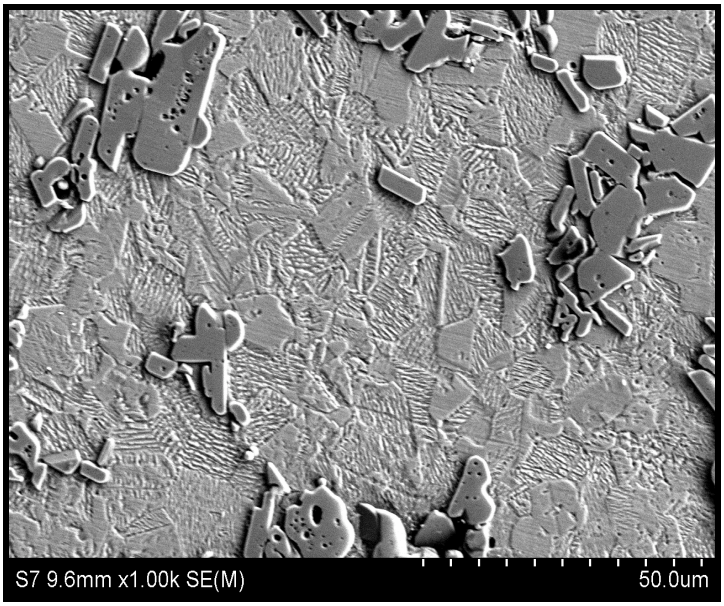

b)

Figure 90: Scanning electron micrographs of sample M1, TiB reinforced TiAl matrix with 10 vol% TiB

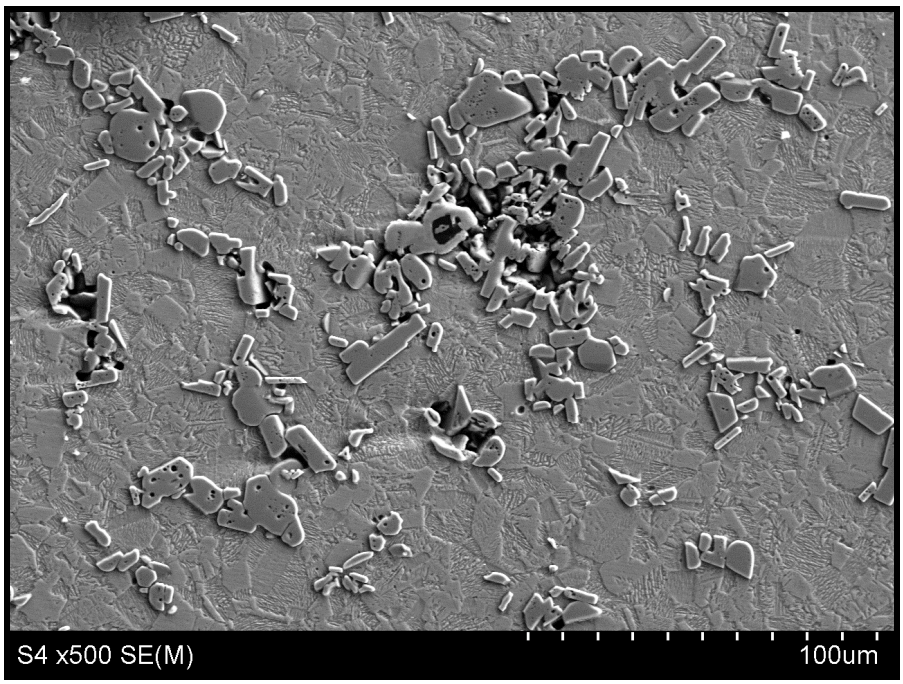

a)

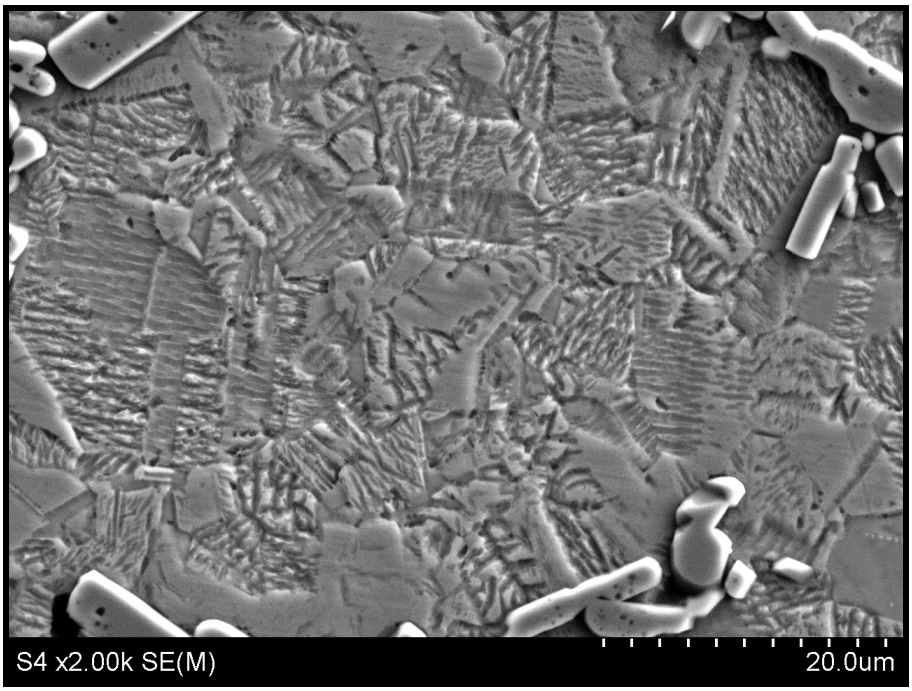

b)

Figure 91: Scanning electron micrographs of sample M2, TiB reinforced TiAl matrix with 20 vol% TiB

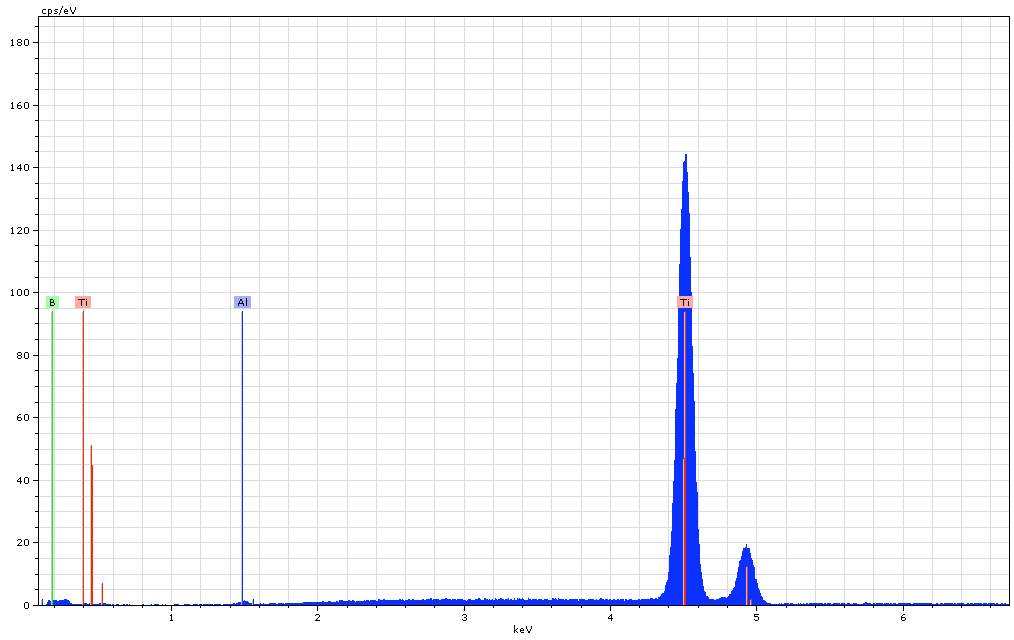

Spectrum: _1 9

El	AN	Series	Net	unn. C [wt.-%]	norm. C [wt.-%]	Atom. C [at.-%]	Error [%]
Ti	22	K-series	129451	78.98	86.38	59.12	2.3
B	5	K-series	5775	12.25	13.40	40.62	1.9
Al	13	K-series	689	0.20	0.22	0.26	0.0
		Total:		91.43	100.00	100.00	

Figure 92: Energy dispersive spectroscopy performed on the titanium boride reinforcement

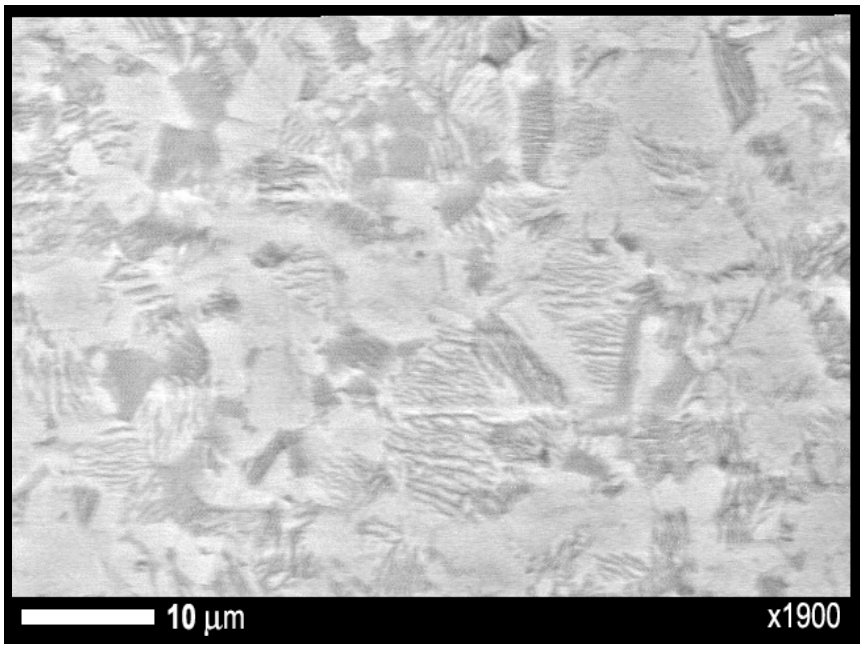

Figure 93: SEM of Ti-48Al-2Cr-2Nb (at%) sample (T3) with no TiB reinforcement

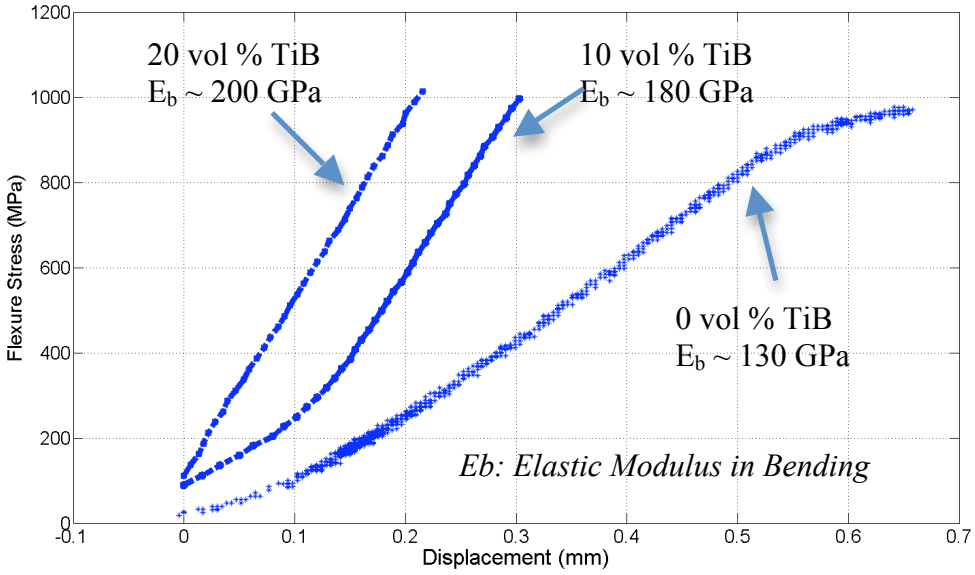

Figure 94: Stress v. displacement plots of TiB reinforced TiAl samples compared to that of TiAl sample (T3) with no reinforcements.

5.4 Discussion

The consolidation of blended TiB_2 and Ti-48Al-2Cr-2Nb powders resulted in a TiAl matrix reinforced with TiB. The TiB was found to be in the form of discontinuous elongated plate structures. These structures were found agglomerated at several locations to form equiaxed plates. It has been determined that in Ti-alloys, TiB_2 reacts with Ti to form TiB. Also, Ti is in thermodynamic equilibrium with TiB as shown in Figure 88. The presence of Nb, which is a boride former also favors the formation of TiB in TiAl matrix. Hence, as expected a TiAl + TiB composite was obtained.

In the development of PM based particulate MMCs, the ratio of the matrix powder particle size to reinforcement powder particle size is very important in achieving a homogeneous distribution of particles in the matrix [136]. Ideally, the powder particle size ratio should be close to one. It has been observed in Al based MMCs reinforced with SiC particulates that larger Al powder particles lead to the agglomeration or clustering of SiC particles between larger Al powder interstices. A similar phenomenon was observed in the TiAl based MMC developed in the present study. The average powder particle size for TiB_2 powders was reported to be 2.5µm, and that of Ti-48Al-2Cr-2Nb powders was reported to be 10µm. Hence, the approximate powder particle size ratio was 5. This high powder particle size ratio led to the agglomeration of the TiB structures at the TiAl matrix interstices.

Due to the large agglomeration of the TiB particles at various TiAl interstices, the diffusion process during consolidation would have been slow. Hence, several voids were observed at the interface between TiB structures and TiAl matrix,

especially where there was large clustering of TiB structures. The resulting density of the two samples M1 and M2 with 10% and 20% (vol%) TiB, respectively was therefore approximately 90% of the theoretical density of the composite system.

Finally, the mechanical properties of the two TiAl based MMC samples M1 and M2 was compared to monolithic TiAl. As expected, it was observed that as the vol% of TiB increased, the bending modulus of the material increased. The tensile modulus of TiB is approximately 440 GPa, and that of TiAl is about 150 GPa. Hence, TiB particulate reinforcements led to significant increase in the bending modulus of the material as shown in Figure 96. There was loss in the ductility of the MMC. This can be attributed to the presence of voids present at the interface between TiB and TiAl.

5.5 Summary and Conclusions

TiAl based metal matrix composite (MMC) with TiB reinforcement was developed by a rapid consolidation technique. TiB_2 and Ti-48Al-2Cr-2Nb powders were blended together and rapidly consolidated to form the MMC. The MMC was found to exhibit the following characteristics:

1. TiAl matrix was reinforced with elongated TiB plates with an average length of 10μm and width of 3μm. At several sites, the TiB plates were agglomerated at the TiAl interstices to form equiaxed TiB plates.

2. The consolidated MMC samples were found to be 90% dense. This was due to the fact that there was a high mismatch between the particle size of the matrix and the reinforcement powders and the consolidation temperature for the composite was relatively low.

3. Reinforcement of TiB in TiAl matrix led to significant increase in the elastic bending modulus of the material.

Chapter 6: Concluding Remarks

6.1 Summary

Dual phase (α_2-Ti_3Al + γ-TiAl) gamma titanium aluminides have been considered as potential replacements for several high temperature alloy systems in both automobile (300^oC - 500^oC) and aerospace (600^oC - 900^oC), propulsion and structural applications. Following almost two decades of research, they are used as intake valves and compressor blades in high performance car engines. Titanium aluminides are also being used in General Electric's GEnex gas turbine engine for the 6^{th} and the 7^{th} stage of the low pressure turbine blades. However, the use of titanium aluminides remains restricted to high performance applications. In order for titanium alumnides to gain wider acceptance, especially in applications replacing Ni-superalloys, further research is required to demonstrate that titanium aluminides match Ni-superalloys in both mechanical performance and manufacturing costs.

As titanium aluminides lack room temperature ductility, it is more expensive to perform traditional manufacturing techniques such as casting, forging and rolling on them. To overcome this, research over the past decade has examined powder metallurgy techniques such as hot-isostatic pressing, sintering and hot-pressing to produce titanium aluminides parts. Enhancements in these powder metallurgy techniques has produced near-net shape parts of titanium aluminides possessing a homogeneous and refined microstructure and thereby exhibiting better mechanical

performance. This dissertation presents a novel powder metallurgy approach to consolidate titanium aluminide powders.

Traditional powder consolidation processes require exposure to high temperatures over a lengthy duration. This exposure leads to grain growth in the consolidated part which adversely affects its mechanical properties. A rapid consolidation process called Plasma Pressure Compaction (P2C) has been introduced and utilized to consolidate titanium aluminide powders to produce titanium aluminide parts with minimal grain growth. The research also explores the role of small alloying additions of Nb and Cr to enhance ductility of the consolidated parts. The grain size of the consolidated part is further reduced in the sub-micrometer range by milling the as-received powders. Finally, a metal matrix composite with TiAl matrix reinforced with TiB was developed by blending the matrix and reinforcement powders followed by its consolidation.

6.2 Limitations of the Current Work

In the current study, the maximum size of the consolidated part was 3" x 2.5" x 0.25". Although, several attempts were made to consolidate parts with higher dimensions (in the order of 4.5" x 4.5" x 0.5") and the parts were found to be fully dense, the microstructure of the parts was not homogeneous. As the size of the consolidated part increased, the temperature profile of the part during consolidation was found to be non-uniform. Hence, the current rapid consolidation process limits the size of the alloy part. This can be solved by carefully designing the plasma pressure compact

assembly such that the current generated (to enable Joule heating) through the powder compact is uniform for the entire dimension of the compact.

6.3 *Future Work*

The current work demonstrates rapid consolidation of dual phase gamma titanium aluminides. It also investigates grain growth suppression and thereby enhancement of mechanical properties (comparable to that of the state of the art titanium aluminide alloys). In order to fully utilize the advantages of rapid consolidation to produce titanium aluminides with significantly superior properties future work in the area may include:

1. Reducing the grain size of titanium aluminides in the nanometer range can result in significant enhancement in its room temperature ductility and strength. Reduction of the grain size in the sub-micrometer range has been demonstrated in the current work by attrition milling of the as-received powders. This path can further be explored to study the impact of milling time on the powder particle size and its effect on the crystallinity of powders. The milling time can be optimized to produce smaller particle size and in turn produce nanometer scale grain size. Although, production of powder particle size in the nanometer range may be difficult by milling processes. Alternate processes of such as solidification of supersaturated vapors may be employed. [147]. Rapid consolidation of nano-sized powders may require more

characterization so that the consolidation parameters can be optimized to produce nanoscale grain size with optimal mechanical properties

2. A metal matrix composite with Ti-48Al-2Nb-2Cr matrix and TiB reinforcement was developed in the current work. This composite was found to be only 90% dense and the reinforcement of TiB was in form of agglomerated plates. This was mainly due to the mismatch in the powder particle size of the matrix and reinforcement. Hence, several consolidation experiments can be conducted where the powder particle size for both the matrix and reinforcement is same. This may solve the problem of agglomeration. Finally, a fully dense MMC can be obtained if the consolidation temperature is increased. Finding an optimal consolidation temperature to produce a fully dense MMC with minimal grain growth is another task which needs further attention.

3. In the current effort the titanium aluminide powders, which were used for consolidation were procured from commercial vendors. These powders were produced by a gas atomization process. The powders obtained using gas atomization are usually very expensive. Also, obtaining powders from commercial vendors with different alloy compositions is usually difficult. Another route for producing titanium aluminide powders is mechanical alloying (MA). In this process the elemental powders (such as Ti and Al for titanium aluminides) are mixed in the required proportion. This process involves repeated fracture and welding of elemental powder particles between

balls that collide with each other at a high energy. The process employs an attrition motion between agitated balls to create an alloyed composite particle. Hence, using MA the desired alloy composition can be easily produced by mixing the right amount of elemental powders. Further, the milling time during MA can be adjusted to obtain the right alloy particle size. This in turn simplifies the process of obtaining powders with particle size in the nanometer range. Several MA experiments starting with Ti and Al elemental powders can be conducted to obtain titanium aluminide alloy powder. A relationship between the milling time and the powder particle size can further be established.

4. In the current study, the effect of impurities on the dislocation modes and thereby the mechanical properties was not characterized. A study to characterize the effects of impurities will be important for further development of the rapid consolidation process. Similarly, the characterization of the effects of crystal orientation, interface boundaries, and grain direction will be very important to further enhance and optimize the rapid consolidation process.

Appendix A: Characterization of Rapidly Consolidated Titanium Diboride

Introduction

Titanium diboride (TiB_2) is a member of the large family of transition metal-metalloid compounds and is well known as a ceramic material with high strength and durability [138]. Its attractive physical and mechanical properties such as melting point, hardness, strength to density ratio, and wear resistance, enable the application of TiB_2 in numerous technological applications. Current use of this material is limited to specialized applications such as impact resistant armor, cutting tools, crucibles, and wear resistant coatings [139]. A recently evolved application is the use of TiB_2 cathodes in the electrochemical reduction (Hall-Heroult Process) of alumina to aluminum metal [138, 139]. Although TiB_2 has great potential, it has found limited applications mainly due to the difficulty in obtaining fully dense bodies [140]. TiB_2 powders typically exhibited low diffusion coefficient and the presence of an oxygen-rich layer on its surface that inhibits densification. Furthermore, the brittle nature and poor ductile properties of TiB_2 at room temperature have restricted its use for structural applications.

Powder metallurgy (PM) is an economical route for producing near net shapes of TiB_2 and minimizes the need for post-machining. One of the problems associated with traditional powder consolidation processes such as sintering, hot pressing and hot isostatic pressing (HIP) is the long processing duration required to achieve full densification. Such extended exposure at high temperatures lead to grain growth and

a resulting deterioration in mechanical properties. In particular, controlling or minimizing grain growth has long been known to increase strength and ductility of materials [141]. Hence, controlling the grain size during any consolidation process is an important processing goal. Rapid consolidation can be a potential solution for the consolidation of TiB_2 because it generally reduces segregation, refines microstructure and thus produces a more homogeneous material.

A novel consolidation process, plasma pressure compaction (P2C) offers the promise of rapid consolidation with minimal or no grain growth. Developed and patented by Materials Modification, Inc. (MMI), the P2C process consists of a plasma activation stage, which removes all oxides and other contaminants on the surface of the powders. Powders are rapidly heated to high temperatures and, with the synergistic application of pressure, high densities are achieved with consolidation times of less than 15 minutes. The P2C process has been successfully utilized to consolidate both nanometer and micron sized powders of metals, ceramics and intermetallics.

Full densification of TiB_2 has been reported to be difficult to achieve due to its low sinterability. The densification of TiB_2 has been shown to improve by the addition of carbon, silicon carbide (SiC), or silicon nitride (Si_3N_4) [138, 142]. The primary role of these additives is the removal of the adsorbed oxide layer (titania, TiO_2) that exists on the surface of the TiB_2 powders. Along with improving densification, the addition of Si_3N_4 as a sintering aid has been shown to improve the strength of TiB_2 [138, 142]. Hence, in the current effort the P2C process was used to rapidly consolidate TiB_2 with Si_3N_4 as a sintering aid.

Commercially available micron-sized powders of titanium diboride with silicon nitride (Si_3N_4) added as a sintering aid, were consolidated and characterized to ascertain their microstructure and mechanical properties. Si_3N_4 was used as a sintering aid to react with titania (TiO_2) to form titanium nitride (TiN), boron nitride (BN) and silica (SiO_2). This eliminates TiO_2, which in turn enhances densification.

Experimental Procedure

Micrometer scale titanium diboride powders were procured from H.C. Starck GmbH and Co., Goslar, Germany. For consolidation using P2C, the powder was mixed with 2.5 wt% of Si_3N_4 as sintering aid. It has been reported that addition of 2.5 wt% of Si_3N_4 as sintering aid leads to maximum densification and improvement in strength [138, 142]. The powder was then contained in a graphite die with plungers inserted on both sides. This assembly was then placed between water-cooled electrodes. The upper electrode was lowered on the top graphite plunger using a hydraulic cylinder to hold the entire assembly together in compression and provide a path for current flow. When sufficient inter-particle contact was established by applying uniaxial pressure, pulsed DC voltage was applied through the powder compact using a full-wave-rectified power supply.

The pulsed electrical power was applied with high current at an adequate voltage. This leads to charge build up within inter-particle gaps. This causes one particle to be charged negatively with respect to the particle in contact with it. As the charge accumulates, the voltage difference becomes sufficiently large to generate sparks that trigger an ionization process. The ions move towards the negatively charged particles

while the electrons move toward the positively charged particles. The ionization process occurs in the form of sparks or plasma generation depending on the energy level at the inter-particle gap. The formation of plasma removes oxides and other contaminants, which form a diffusion barrier in the consolidation process. As a result particle re-arrangement and diffusion is enhanced.

After pulsing, direct current was applied through the powder compact resulting in Joule heating. Consolidation was carried out at in vacuum at temperatures between 1500°C and 1600°C for 20 minutes. The consolidated sample was then cooled gradually to room temperature. A consolidated sample of dimensions 3 inches x 2.25 inches x 0.25 inches was produced as shown in Figure 95.

The microstructure of the consolidated samples was characterized using optical microscopy, scanning electron microscopy (SEM) and wavelength dispersive spectroscopy (WDS). Consolidated samples were sectioned and metallographically polished down to a 1μm diamond finish. Polished samples were subsequently etched 15 to 30 seconds in a fresh solution of 10cm^3 concentrated HF, 3 cm^3 concentrated HNO_3 and 10cm^3 concentrated HCl to reveal microstructural details such as grain size and shape.

The mechanical properties of the consolidated specimens were characterized via four-point bending tests and Vickers hardness tests. A self-aligning four-point bend fixture as shown in Figure 21 was designed according to the ASTM standard C1161 (configuration A) with an outer-span of 20 mm and an inner-span of 10 mm. Consolidated samples were machined with chamfered edges to a dimension of 25 mm x 1.5 mm x 2.0 mm bend bars and 25 mm x 3 mm x 4 mm chevron notch bars

according to the ASTM standards C1161 and C1421 [109] respectively. The chevron notch bars had a 60 degrees notch in the center. They were machined via electro-discharge machining. The machined specimens were mounted with uniaxial strain gages to measure strain on the outer fiber (under tension) of the specimen during four-point bending tests. The four-point bending tests yielded flexure strength, fracture toughness and Young's modulus. All tests were conducted at a strain rate of 0.75×10^{-4} in a Material Testing Systems' (MTS) model 810 machine. To ensure the accuracy of the results obtained by four-point bending, "control" samples prepared from AD998 aluminum oxide obtained from CoorsTek, Golden, CO were also tested. The flexure strength, fracture toughness and Young's modulus of the AD998 samples were in excellent agreement with those reported by CoorsTek.

The density of the consolidated material was determined by measuring the mass and the volume of the precisely machined specimens used for four-point bending tests. Microhardness of the consolidated samples were obtained on polished specimens using a diamond Vickers indent under a load of 1000 grams with a dwell time of 15 seconds.

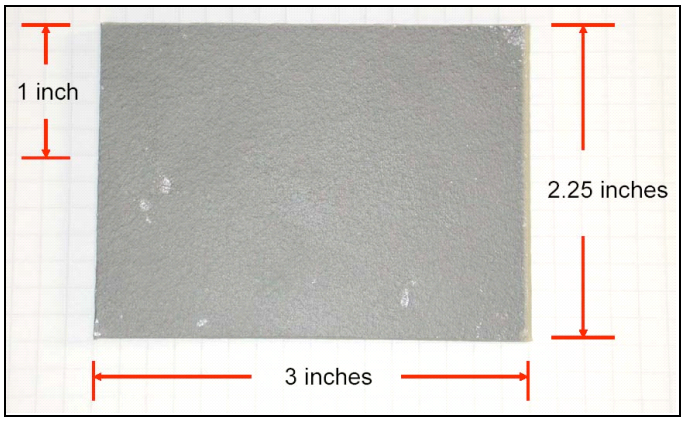

Figure 95: 0.25 inches thick P2C consolidated TiB_2 sample

Results and Discussion

The SEM micrographs of the consolidated samples are shown in Figures 96a and 96b. The density of the consolidated specimen was found to be 4.229 $\pm$ 0.008 g/cm^3. The theoretical density [143] of TiB_2 is 4.52 g/cm^3, indicating that the consolidated sample was 93.5 $\pm$ 0.2% of theoretical density. The SEM micrographs showed the presence of a dark phase, which was determined to be amorphous SiO_2 via wavelength dispersive spectroscopy (WDS). Silicon nitride reacted with the surface titania (TiO_2) to form this amorphous phase of SiO_2. From previous studies it has been determined that a limited presence of SiO_2 inhibits grain growth while promoting densification [138, 142]. This in turn significantly enhances the mechanical properties of titanium diboride. The average grain size of the consolidated sample was found to be 2.3 µm as measured by the line-intercept method.

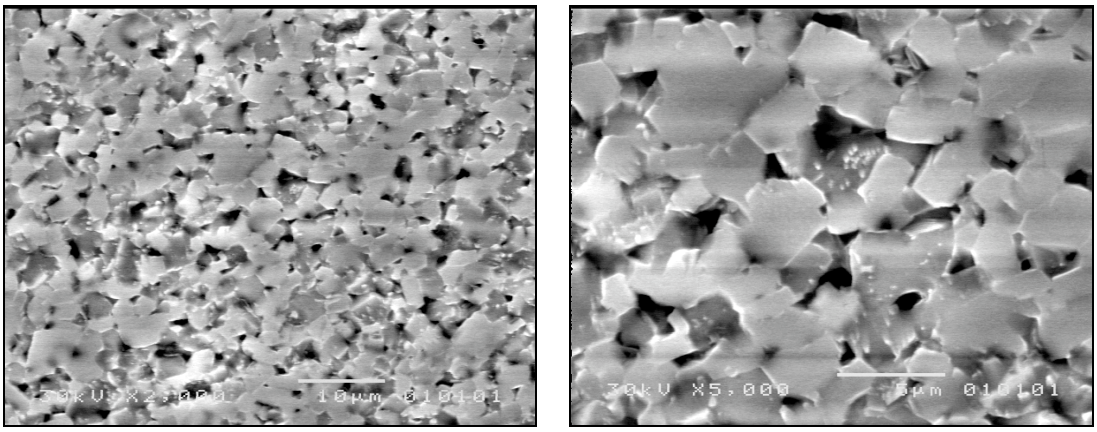

a) b)

Figure 96: SEM micrograph of P2C consolidated TiB_2 specimen at a) 2000x, and b) 5000x

In order to fully understand the role of chemical composition of the starting powders on the composition, microstructure and properties of the consolidated TiB_2 samples, chemical composition of the as-received TiB_2 powder and P2C consolidated TiB_2 specimen were analyzed. The results are shown in Table 19. The presence of oxygen in the order of 2.14 wt% in the as-received powders was a concern because oxygen content greater than 0.5 wt% usually inhibits maximum attainable density and increases grain and pore coarsening [144]. Thus, the addition of Si_3N_4 was necessary to remove TiO_x. As shown in Table 17, the oxygen content of the P^2C consolidated sample was reduced by 13.55% compared to that of the as-received powders. The nitrogen content in the consolidated sample as expected increased due to addition of Si_3N_4. The increase in carbon was suspected to be due contamination from the graphite die, which was used to contain the powders during the consolidation process.

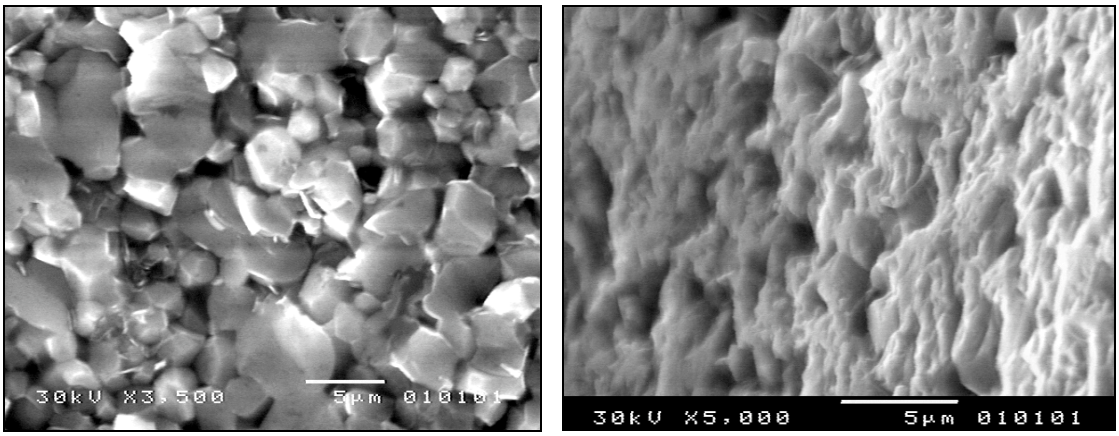

Figure 97: Fracture SEM micrograph of P2C consolidated TiB_2 a) bend bar, and b) chevron notched bar

The consolidated sample was 93.5% dense. Park et al [138, 142], were able to achieve approximately 95% dense samples by hot pressing TiB_2 powders at 1550^{o}C for one hour with 2.5 wt% Si_3N_4 as sintering aid. They were further able to achieve densities close to 100% by hot pressing the powders at temperatures above 1600^{o}C. Hence, the P^2C procedure can further be refined to produce fully dense TiB_2 by increasing the consolidation temperature above 1600^{o}C.

The mechanical properties of the consolidated specimens were determined by four-point bending tests. The SEM images of the fractured bend bars and chevron notched bars are shown in Figures 88a and 88b respectively. The SEM images show both trans-granular and inter-granular fracture. The cleaved structures in Figures 97a and 97b show the evidence of trans-granular fracture while the appearance of defined grains suggest inter-granular fracture. This is further evident by the high

magnification SEM images of the fractured bend bar specimen as shown in Figures 98a and 98b.

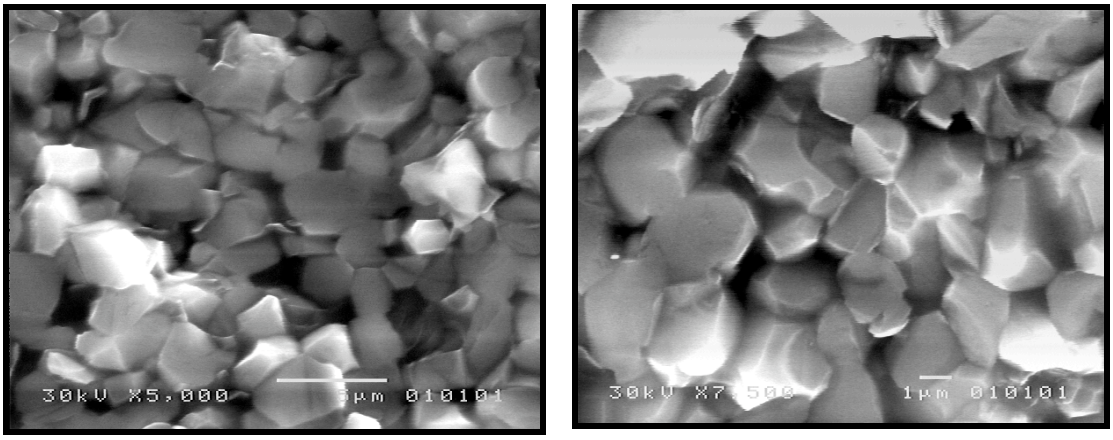

a) b)

Figure 98: Fracture SEM micrograph of P2C consolidated at TiB_2 bend bar at a) 5000X, and b) 7500X

The mechanical properties of the consolidated specimens at room temperature are listed in Table 20. The values listed in Table 20 are averages taken over data for five TiB_2 test specimens. The flexure strength was found to be 517.83 MPa. This is superior to the typical values reported in the literature, which are around 400 MPa [145]. The fracture toughness (K_{IC}) of the consolidated specimen was calculated as 4.48 MPa $m^{1/2}$. The Young's modulus as determined by the stress versus strain curve (obtained from four-point bending tests) shown in Figure 99, was found to be 409.61 GPa. The Vickers hardness was 19.57 GPa. The Young's modulus, the fracture toughness and the Vickers hardness were in the range of the typical values reported in the literature [145].

Table 19: Chemical composition of as-received TiB_2 powder and P2C consolidated TiB_2 specimen

	AS-RECEIVED TIB_2 POWDER	**P2C CONSOLIDATED TIB_2 SPECIMEN**
Element	WEIGHT %	WEIGHT %
Carbon	0.149	0.380
Oxygen	2.14	1.84
Nitrogen	0.15	1.60

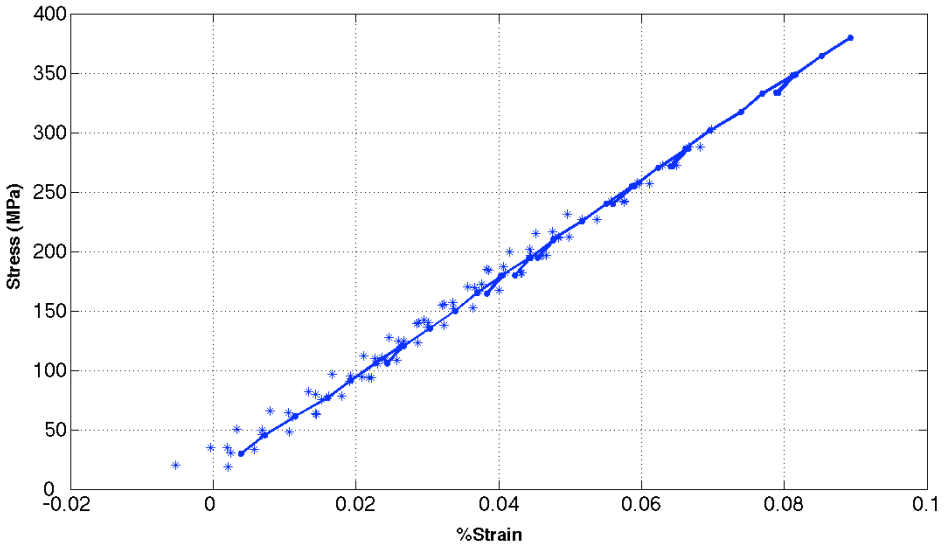

Figure 90: Stress v. strain plot for P2C consolidated TiB_2

Table 20: Chemical composition of as-received TiB_2 powder and P2C consolidated TiB_2 specimen

Mechanical Properties	P2C Consolidated TiB_2	Park et al*, 2000 [138]	Munro**, 2000 [143]
Flexural Strength	517.83 MPa	~500 MPa	320 MPa
Fracture Toughness	4.48 MPa $m^{1/2}$	~5.75 MPa $m^{1/2}$	~5 MPa $m^{1/2}$
Elastic Modulus	420.61 GPa	NR	~440 GPa
Vickers Hardness	19.57 GPa	~20 GPa	~20 GPa

**Properties from Park et al [138] for samples sintered at similar temperatures*

***Properties from Munro [143] are for similar densities*

Summary and Conclusions

This study demonstrated the feasibility of plasma pressure compaction (P2C) as a successful technique for rapid consolidation of titanium diboride powders. The consolidated samples were 93.5% of theoretical density. The mechanical properties of the consolidated samples were superior to that of pure TiB_2 as reported in the literature. This can primarily be attributed to the control of grain size, which was

achieved due to rapid consolidation via P2C and the presence of Si_3N_4 as a sintering aid.

Appendix B: Method for Calculating Modulus in Bending

As shown in Figure 99, a one-point load was induced on the four-point bending test set-up. The loads induced on the specimen can then be further simplified as show in Figure 100.

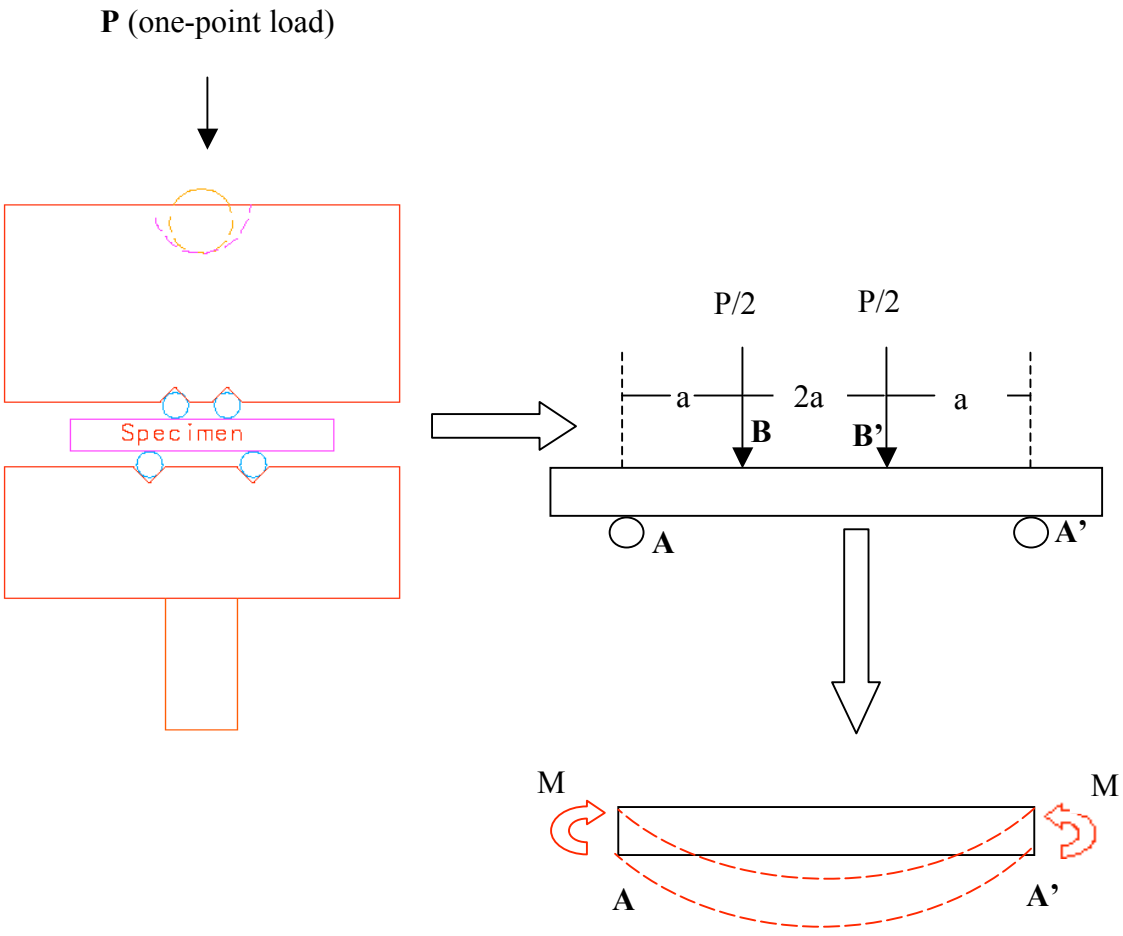

Figure 99: Four-point bending test set-up

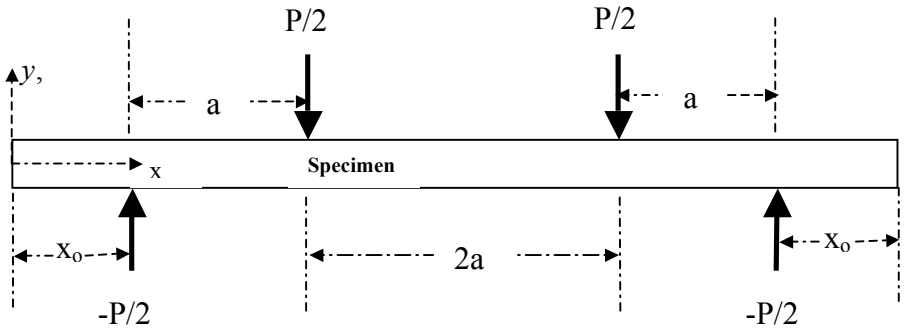

Figure 100: Loads on the specimen

Taking one end of the beam as the origin with the positive x and y directions indicated in Figure 100, we can calculate the moment and shear forces on the beam along its span. The shear and moment diagrams of the beam are shown below.

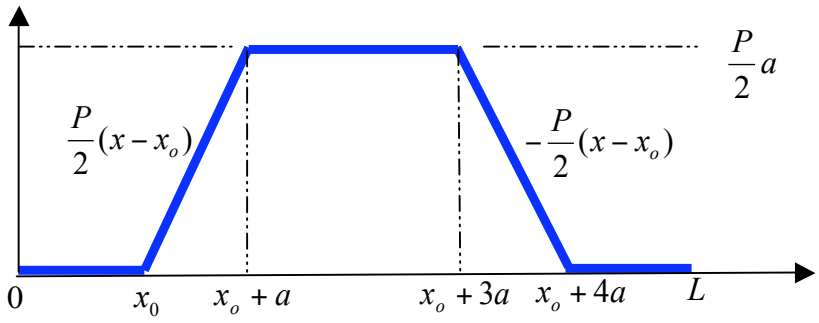

Figure 101: Moment diagram

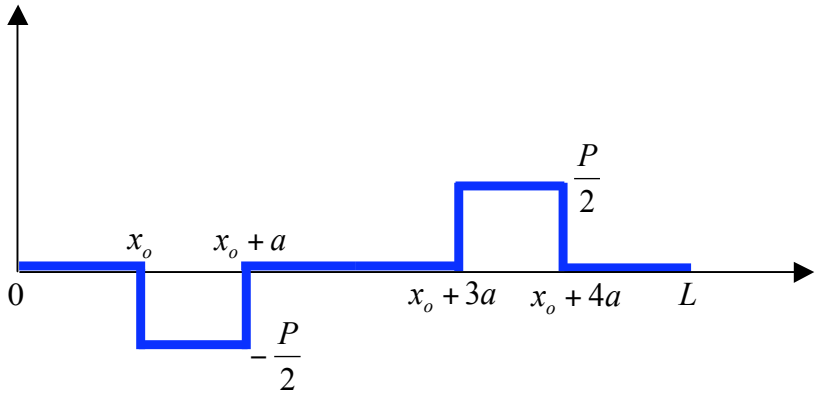

Figure 102: Shear diagram

With the shear and moment diagrams, we can calculate the bending stress on the beam along its span and thickness. Since the maximum moment is at the center of the beam, we are more interested in calculating the bending stress at the center. The bending stress on the beam can be given as

$$\sigma = \frac{Mc}{I} \tag{1}$$

Where σ is the bending stress, M is the moment, c is the distance from the neutral axis of the beam (which is located at the center of the beam along its thickness) and I is the moment of inertia along the z-axis (z-axis comes out of the page). The maximum bending stress can be calculated at $c = h/2$, where h is the thickness of the beam. The moment of inertia of the beam can be calculated as

$$I = \frac{bh^3}{12} \tag{2}$$

Where, b is the width of the beam.

From linear elastic analysis of a beam, we know that

$$\frac{d^2v}{dx^2} = \frac{M}{EI} \tag{3}$$

Where v is the vertical displacement of the specimen. Our boundary conditions for equation (3) are

$$v(x_o) = 0 \tag{4}$$

$$\frac{dv}{dx}(x_o + 2a) = 0 \tag{5}$$

Using the condition of continuity at $x = x_o + a$, and the boundary conditions given by equation (4) and (5), we can integrate equation (3) piecewise for $x_o \le x \le x_o + a$ and $x_o + a \le x \le x_o + 3a$ to find the displacement at $x = x_o+2a$.

$$EIv(x_o + 2a) = -\frac{11}{12}Pa^3 \tag{6}$$

Since we will be measuring $v\,(x_o+2a)$ in our test, we can calculate the elastic modulus of the beam as

$$E = -\frac{11}{12}\frac{Pa^3}{Iv(x_o + 2a)} \tag{7}$$

which can be further written as [146]

$$E = -\frac{11a^3}{bh^3}m \tag{8}$$

where m is the slope of the linear portion of the plot of load (P) versus displacement (v)

Bibliography

1. S. M. Soudani, "High Performance RX2 Ti 6242S Titanium for Re-useable Launch Vehicles Metallic Thermal Protection Systems," *in AIAA Space 2000 Conference & Exposition*, AIAA-2000-5147, 19-21 September, 2000.

2. G. Das, H. Kestler, H. Clemens, and P.A. Bartolotta, "*Sheet Gamma TiAl: Status and Opportunities," Journal of Materials*, pp. 42-45, 2004.

3. S. Djanarthany, J.C. Viala, and J. Bouix, "*An Overview of Monolithic Titanium Aluminides based on Ti_3Al and TiAl," Materials Chemistry and Physics*, vol. 72, pp. 301–319, 2001.

4. J. P. Immarigeon, R. T. Holt, A. K. Koul, L. Zhao, W. Wallace, and J. C. Beddoes, "Lightweight Materials for Aircraft Applications*," Materials Charecterization*, vol. 34, pp. 41-67, 1995.

5. F. H. Froes, C. Suryanarayana, and D. Eliezer*, "Review Synthesis, Properties and Applications of Titanium Aluminides,"* Journal of Materials Science, vol. 27, pp. 5113-5140, 1992.

6. *W. Voice,* "The Future of Gamma-Titanium Alumnides by Rools Royce," *Aircraft Engineering and Aerospace technology*, vol. 71, pp. 337-340, 1999.

7. P. Krause, A. Bartolotta, and L. David, "*Titanium Aluminide Applications in the High Speed Civil Transport," in International Symposium on Gamma Titanium Aluminides,* San Diego, CA, pp. 1-9, 1999.

8. W. Voice, M. Henderson, E. Shelton, X. Wu, "Gamma Titanium Aluminide, TNB," *Intermetallics*, vol. 13, pp. 959–964, 2005.

9. G. Sauthoff, *Intermetallics,* Weinheim, NY, 1995.

10. G. Lütjering, and J. Williams, "Titanium,*" Engineering Materials and Processes,* Springer, NY, 2007.

11. W. O. Soboyejo, F. Ye, and T. S. Srivatsan, "The Fatigue and Fracture Behavior of a Gamma-Titanium Alumnide Intermtallic: Influence of Ductile Phase Reinforcement*," Engineering Fracture Mechanics*, vol. 56, pp. 379-395, 1997.

12. W. O. Soboyejo, W. Shen, J. Lou, C. Mercer, V. Sinha, A. B. O. Soboyejo, "Probabilistic Framework for the Modeling of Fatigue in Cast Lamellar Gamma-based Titanium Aluminides," *Mechanics of Materials*, vol. 36, pp. 177–197, 2004.

13. Al. W. Sommer, and G. C. Keijzers, *Gamma Titanium Aluminides 2003.* [ed.] Y-W. Kim, H. Clemens and A. H. Rosenberger, TMS, PA, 2003.

14. D. Dimiduk, P. L. Martin, and R. Dutton, *Gamma Titanium Aluminides 2003.* [ed.] Y-W. Kim, H. Clemens and A. H. Rosenberger, TMS, PA, 2003.

15. H. Baur, D. B. Wortberg, H. Clemens, *Gamma Titanium Aluminides.* [ed.] Y-W Kim, H. Clemens and A. H. Rosenberger, TMS, PA, pp. 23-31, 2003.

16. GE Aviation, *GE - Aviation: GEnx. GE.* [Online], 2007. http://www.geae.com/engines/commercial/genx/.

17. G. Das, P. A. Bartolotta, H. Kestler, and H. Clemens, *Gamma Titanium Aluminides 2003.* [ed.] Y-W Kim, H. Clemens and A.H. Rosenberger, TMS, PA, pp. 33-45, 2003.

18. NASA Glenn Research Center, "PM Gamma Titanium Aluminide and Fabrication Techniques*," NASA Tech Briefs*, LEW-17173, Cleveland, OH.

19. Y-W. Kim*,* "Intermetallic Alloys Based on Gamma Titanium Aluminides," *Journal of Materials,* pp. 24-30, July 1989.

20. F. H. Froes, and C. Suryanarayana, *Physical Metallurgy of and Processing of Intermetallics Compounds.* Chapman and Hall, NY, 1995.

21. Y. L. Hao, R. Yang, Y. Y. Cui, and D. Li, "The Influence of Alloying on the Alpha/(Alpha + Gamma)/Gamma Phase Boundaries in TiAl based Systems," *Acta Mater*, vol. 48, pp. 1313-1324, 2000.

22. K. Bird, K, and T. A. Wallace, "Development of Protective Coatings for High-Temperature Metallic Materials*," Journal of Spacecrafts and Rockets*, vol. 41, pp. 213-220, 2004.

23. S. Sarkar, S. Datta, S. Das, and D. Basu, "Oxidation Protection of Gamma-Titanium Aluminide using Glass–ceramic Coatings," *Surface & Coatings Technology*, vol. 203, pp. 1797–1805, 2009.

24. Ding, H; Song, D; Wang, D; Zhang, C; Cui, J*, "*Microstructural Evolution in Superplastic Deformation of a Ti_3Al Alloy," *Journal of Material Science Letters*, vol. 19, pp. 1135 – 1137, 2000.

25. F. Appel, M. Oehring, J. D. H. Paula, C. H. Klinkenberg, and T. Carneiro "Physical Aspects of Hot-working Gamma-based Titanium Aluminides," *Intermetallics*, vol. 12, pp. 791–802, 2004.

26. J. Chraponski, W. Szkliniarz, W. Koscielna, and B. Serek, "Microstructure and Chemical Composition of Phases in Ti-48Al-2Cr-2Nb Intermetallic Alloy," *Material Chemistry and Physics*, vol. 81, pp. 438-442, 2003.

27. Y-W. Kim, "Microstructural Evolution and Mechanical Properties of a Forged Gamma Titanium Alloy," *Acta Metallurgica et Materialia*, vol. 40 (6), pp. 1121-1133, 1991.

28. R. V. Ramanujan, "Phase Transformations in Gamma based Titanium Aluminides," *International Materials Reviews*, vol. 45 (6), pp. 218-239, 2000.

29. L. S. Draper, G. Das, I. Locci, J. D. Whittenberger, B. A. Lerch, H. Kestler, *Gamma Titanium Aluminides 2003.* [ed.] Y-W. Kim, C. Helmut and A. H. Rosenberger, TMS, PA, 2003.

30. F. Appel, M. Oehring, and R. Wagner, "Novel Design Concepts for Gamma-Based Titanium Alumnide Alloys*," Intermetallics*, vol. 8, pp. 1283-1312, 2000.

31. Y-W. Kim, "Effects of microstructure on the deformation and fracture of gamma-TiAl alloys," *Materials Science and Engineering*, vol. Al92/193, pp. 519-533, 1995.

32. C. Choi, H. J. Kim, Y.T. Lee, and Y. Kim, "Effects of microstructural parameters on the fatigue crack growth of fully lamellar gamma-TiAl alloys," *Materials Science and Engineering*, vols. A329-331, pp. 545–556, 2002.

33. D. Dimiduk, P. Martin, and Y-W. Kim, "Microstructure Development in Gamma alloy Mill Products by Thermomechanical Processing," *Materials Science and Engineering*, vol. A243, pp. 66 – 76, 1998.

34. M. Fukotomi, H. Hasegawa, "Lamellar Orientation Control in TiAl Base Alloys by a Two-step Compression Process at High Temperature," *Materials Science and Engineering*, vol. 508, pp. 106–113, 2009.

35. Y-W. Kim, and D. Dimiduk, "Progress in the Understanding of Gamma Titanium Aluminides*," Journal of Materials*, pp. 40-47, August 1991.

36. Y-W. Kim, "Strength and Ductility in TiAl Alloys," *Intermetallics*, vol. 6, pp. 623-628, 1998.

37. M. Yamaguchi, and H. Inui, and K. Ito, "High-Temperature Structure Intermetallics," *Acta Mater*, vol. 48, pp. 307-322, 2000.

38. C. Mercer, and W. O. Soboyjo, "Fatigue Crack Growth in Cast Gamma Titanium Alumnides," *Acta Mater*, vol. 45 (10), pp. 4385-4396, 1997.

39. C. Mercer, and W. O. Soboyejo, "Hall-Petch Relationships in Gamma Titanium Alumnides," *Scripta Materialia,* vol. 35 (1), pp. 17-22, 1996.

40. R. Porizek, V. Radoslav, S. Znam, and M. D. Nguyen, "Atomistic Studies of Dislocation Glide in Gamma-TiAl," *in Materials Research Soceity Symposium*

Proceedings, Department of Materials Science & Engineering, University of Pennsylvania, vol. 753, pp. 1-6, 2003.

41. W. T. Marketz, F. D. Fischer, and H. Clemens, "Deformation Mechanisms in TiAl Intermetallics—Experiments and Modeling," *International Journal of Plasticity*, vol. 19, pp. 281–321, 2003.

42. R. Wagner, R and F. Appel, *Gamma Titanium Alumnides*. [ed.] Y-W. Kim, R. Wagner and M. Yamaguchi, TMS, PA, pp. 231-244, 1995.

43. G. Vishwanathan, M. Mills, and V. Vasudevan, "Microstructural Effects on the Tensile Properties and Deformation Behavior of a Ti-48Al Gamma Titanium Aluminide," *Metallurgical and Materials Transactions*, vol. 34A, pp. 2113-2127, 2003.

44. G. Hug, A. Loiseau, P. Veyssière, "Weak-beam Observation of a Slip Transition in TiAl," *Philosophical Magazine A*, vol 57, pp. 499-523, 1988.

45. V. K. Vasudevan, M. A. Stucke, S. A. Court, and H. L. Fraser, "The Influence of Second Phase Ti_3Al on the Deformation Mechanisms in TiAl," *Philosophical Magazien Letters*, vol. 59 (6), pp. 299-307, 1989.

46. I. H. Katzarov, and A. T. Paxton, "Atomic Studies of <101] Screw Dislocation Core Structures and Glide in Gamma-TiAl," *Philosophical Magazine*, vol. 89 (21), pp. 1731-1750, 2009.

47. M. Hishinuma, and H. Yoo, "Deformation Twinning in TiAl: Effects of Defect Clustering," *Metals and Materials*, vol. 3 (2), pp. 65-74, 1997.

48. E. Cerreta, and S. Mahajan, "Formation of Deformation Twins in TiAl," *Acta Materialia*, vol. 49, pp. 3803–3809, 2001.

49. S. Sriram, V. Vasudevan, and D. Dimiduk, "Dislocation Structures and Deformation Behaviorof Ti-50/52Al Alloys between 77 and 1173K," *Materials Science and Engineering A*, vol. 192/193, pp. 217-225, 1995.

50. S. H. Whang, Z. M. Wang, and Z. X. Li, "Deformation in G-TiAl Aluminides - Focused on Anomalous Hardening," *in Gamma Titanium Aluminides* [ed.] Y-W. Kim, R. Wagner and M. Yamaguchi, p. 245, TMS, PA, 1995.

51. C. T. Yang, Y. C. Lu, and C. H. Koo, "The High Temperature Tensile Properties and Microstructural Analysis of Ti–40Al–15Nb Alloy*," Intermetallics*, vol. 10, pp. 161–169, 2002.

52. C. Zhang, and K. Zhang, "Tensile Behaviors of Fine-grained Gamma-TiAl based Alloys Synthesized by Pulse Current Auxiliary Sintering," *Materials Science and Engineering A*, vol. 520, pp. 101-104, 2009.

53. W. T. Marketz, F. D. Fischer, F. Kauffmann, G. Dehm, T. Bidlingmaier, A. Wanner, and H. Clemens, "On the Role of Twinning during Room Temperature Deformation of Gamma-TiAl based Alloys," *Materials Science and Engineering*, vol. A329, pp. 177 – 183, 2002.

54. U. Christop, F. Appel, and R. Wagner, *High-temperature Ordered Intermetallic Alloys VII.* [ed.] C. C. Koch, N. S. Stoloff, C. T. Liu, A. Wanner, *Mater. Res. Sot. Symp. Proc.*, Pittsburgh, vol. 460, pp. 207-212, 1997.

55. R. Gerling, A. Bartels, and H. Clemens, “Structural Charecterization and Tensile Properties of a High Nb containing Gamma TiAl Sheet obtained by Powder Metallurgical Processing,” *Intermetallics*, vol. 12, pp. 275-280, 2004.

56. R. Braun, M. Fruhlich, C. Leyens, and D. Renusch, “Oxidation Behavior of TBC Systems on Gamma-TiAl Based Alloy-45Al-8Nb,” *Oxidation of Metals*, vol. 71 (5-6), pp. 295-318, 2009.

57. E. Hamzah, M. Kanniah, and M. Harun,“Effect of Beta Phase on Room to High Temperature Mechanical Properties of As-Cast Gamma Titanium Alumnides,” *Mechanics of Advanced Materials and Structures*, vol. 16 (5), pp. 384-389, 2009.

58. Z. W. Huang, and T. Cong, “Microstructural Instability and Embrittlement Behaviour of an Al-lean, High-Nb Gamma-TiAl-based Alloy Subjected to a Long-term Thermal Exposure in Air,” *Intermetallics*, vol. 18, pp. 161–172, 2010.

59. Y. Liu, H. Li, S. Wang, and H. Ye, “Nb Effects on the Structural and Mechanical Properties of TiAl alloy: Density-functional theory Study,” *Journal of Materials Research*, vol. 24 (10), pp. 3165-3172, 2009.

60. D. Hu, J. F. Mei, M. Wickins, and R. A. Hardy “Microstructure and Tensile Properties of Investment Cast TiAl-46Al-8Nb-1B Alloy,” *Scripta Materialia*, vol. 47, pp. 273-278, 2002.

61. Y-W. Kim, A. Rosenberger, and D. M. Dimiduk, “Microstructural Changes and Estimated Strengthening Contributions in a Gamma Alloy Ti–45Al–5Nb Pack-rolled Sheet,” *Intermetallics*, vol. 17, pp. 1017–1027, 2009.

62. W. J. Zhang, S. C. Deevi, and G. L. Chen, "On the Origin of Superior High Strength of Ti–45Al–10Nb Alloys," *Intermetallics*, vol. 10, pp. 403–406, 2002.

63. J. C. Woo, S. K. Varma, and R. N. Mahapatra, "Oxidation Behavior and Transmission Electron Microscope Characterization of Ti-44Al-xNb-2(Ta,Zr) Alloys,*" Metallurgical and Materials Transactions*, vol. 34A, pp. 2263-2271, 2003.

64. M. Shazly, V. Prakash, and S. Draper, "Dynamic Fracture Initiation Toughness of a Gamma (Met-PX) Titanium Aluminide at Elevated Temperatures," *Metallurgical and Materials Transactiions A*, vol. 40A, pp. 1400-1412, 2009.

65. W. Schillinger, H. Clemens, G. Dehm, and A. Bartels, "Microstructural Stability and Creep Behavior of a Lamellar Gamma-TiAl Based Alloy with Extremely Fine Lamellar Spacing," *Intermetallics*, vol. 10, pp. 459-466, 2002.

66. J. H. Jeon, A. B. Godfrey, P. A. Blenkinsop, W. Voice, and Y. D. Hahn, "Recrystallization in Cast 45-2-2 XD™ Titanium Aluminide," *Materials Science and Engineering*, vol. 271A, pp. 128–133, 1999.

67. L. Christodoulou, P. A. Parrish, and C. R. Crowe, "High Temperature, High Performance Composites*," in Material Research Society Symposia Proceedings*, Pittsburgh, vol. 120, p. 29, 1988.

68. Y. Y. Chen, H. B. Yua, D. L. Zhang, and L. H. Chaia, "Effect of Spark Plasma Sintering Temperature on Microstructure and Mechanical Properties of an

Ultrafine grained TiAl Intermetallic Alloy," *Materials Science and Engineering*, vol. A525, pp. 166–173, 2009.

69. E. Szewczak, J. Paszula, A. V. Leonov, and H. Matyja, "Explosive Consolidation of Mechanically Alloyed Ti-Al alloys," *Materials Science and Engineering*, vol. A226/228, pp. 115-118, 1997.

70. T. Cheng, and M. McLean, "Characterization of TiAl Intermetallic Rods Produced from Elemental Powders by Hot Extrusion Reaction Synthesis (HERS)," *Journal of Material Science*, vol. 32, pp. 6255-6261, 1997.

71. E. Fu, R. D. Rawlings, and H. B. McShane, "Reaction Synthesis of Titanium Aluminides," *Journal of Materials Science* , vol. 36, pp. 5537 – 5542, 2001.

72. H. Hitoshi, and Z. Sun, "Fabrication of TiAl Alloys by MA-PDS process and the Mechanical Properties*," Intermetallics*, vol. 11, pp. 825-834, 2003.

73. X. Lu, X. B. He, B. Zhang, L. Zhang, X. H. Qu, and Z. X. Guo, "Microstructure and Mechanical Properties of a Spark Plasma Sintered Ti–45Al–8.5Nb–0.2W–0.2B–0.1Y Alloy," *Intermetallics*, vol. 17, pp. 840–846, 2009.

74. L. Cao, H. W. Wang, C. M. Zou, Z. J. Wei, "Microstructural Characterization and Micromechanical Properties of Dual-Phase Carbide in Arc-Melted Titanium Aluminide based Alloy with Carbon Addition," *Journal of Alloys and Compounds*, vol. 484, pp. 816-821, 2009.

75. C. F. Yolton, Y-W. Kim, and U. Habel, *Gamma Titanium Aluminides 2003.* [ed.] Y-W. Kim, C. Helmut and A. H. Rosenberger, TMS, PA, p. 233, 2003.

76. M. Oehring, T. Klassen, and R. Borman, "The Formation of Metastable Ti-Al Solid Solutions by Mechanical Alloying and Ball Milling*," Journal of Material Research,* vol. 8 (11), 1993.

77. V. I. Fadeeva, A. V. Leonov, E. Szewczak, and H. Matyja "Structural Defects and Thermal Stability of Ti(Al) Solid Solution Obtained by Mechanical Alloying," *Materials Science and Engineering*, vol. A242, pp. 230 – 234, 1998.

78. S. Kumaran, T. R. Srinivasa, R. Subramanian R., and Angelo P, "Nanocrystalline and Amorphous Structure Formation in Ti-Al during High Energy Ball Milling," *Powder Metallurgy*, vol. 48 (4), pp. 354-358, 2005.

79. Y. L. Chen, Y. Ming, Y. M. Sun, B. C. Mei, and J. Q. Zhu, "The Phase Transformation and Microstructure of TiAl/Ti_2AlC Composites caused by Hot Pressing," *Ceramics International*, vol. 35, pp. 1807-1812, 2009.

80. U. Habel, and B. J. McTiernan, "HIP Temperature and Properties of a Gas-atomized Gamma-TiAl Alloy," *Intermetallics*, vol. 12, pp. 63-65, 2004.

81. P. R. Smith, A. H. Rosenberger, M. J. Shepard, and R. Wheeler, "A P/M Approach for the Fabrication of an Orthorhombic Titanium Aluminide for MMC Applications," *Journal of Material Science*, vol. 35, pp. 3169 – 3179, 2000.

82. R. Gerling, F. P. Schimansky, and H. Clemens, *Gamma Titanium Aluminides 2003.* [ed.] Y-W Kim, H. Clemens and A. H. Rosenberger, TMS, PA, p. 249, 2003.

83. F. P. Schimansky, K. W. Liu, and R. Gerling, "Spray Forming of Gamma Titanium Alumnides," *Intermetallics*, vol. 7, pp. 1275-1282, 1999.

84. C. E. Weeks, "Evaluation of a Gamma Titanium Alumnide for Hypersonic Structural Applications," *M.S. Thesis,* Georgia Institute of Technology, 2005.

85. P. Bhattacharya, P. Bellon, R. S. Averback, and S. Hales, "Nanocrystalline TiAl Powders Syntehsized by High-Energy Ball Milling: Effects of Milling Parameters on Yield and Contamination," *Journal of Alloys and Compounds*, vol. 368, pp. 187-196, 2004.

86. Bohn R., Klassen T., and Bormann R, "Mechanical Behavior of Submicron-grained Gamma-TiAl-based Alloys at Elevated Temperatures," *Intermetallics*, vol. 9, pp. 559–569, 2001.

87. K. T. Kashyap, and T. Chandrahsekha, "Effects and Mechanisms of Grain Refinement in Aluminium Alloys," *Bulletin of Material Science* , vol. 24 (4), pp. 345–353, 2001.

88. C. Suryanarayana, "Mechanical Alloying and Milling," *in Progress in Material Science*, [ed.] M. Ashby, B. Cantor, J. W. Christian, T. B. Massalski, Pergamon, vol. 46, pp. 1-184, 2001.

89. N. Forouzanmehr, F. Karimzadeh, and M. H. Enayati, "Study on Solid-state Reactions of Nanocrystalline TiAl Synthesized by Mechanical Alloying," *Journal of Alloys and Compounds*, vol. 471, pp. 93-97, 2009.

90. N. Forouzanmehr, F. Karimzadeh, and M. H. Enayati, "Synthesis and Characterization of TiAl/Al_2O_3 Nanocomposite by Mechanical Alloying," *Journal of Alloys and Compounds*, vol. 478, pp. 257–259, 2009.

91. G. Gonzalez, A. Sagarzazu, D. Bonyuet, L. D. Angelo, and R. Villalba, "Solid State Amorphisation in Binary Systems prepared by Mechanical Alloying," *Journal of Alloys and Compounds*, vol. 483, pp. 289-297, 2009.

92. O, N. Senkov, N. Srisukhumbowornchai, M. L. Ovecoglu, and F. H. Froes, "Microstructural Evolution of a Nanocrystalline Ti-47Al-3Cr Alloy on Annealing at 1200°C," *Scripta Materialia* , vol. 39 (6), pp. 691– 698, 1998.

93. E. Szewczak, and J. W. Wyrzykowski, "Influence of the Mechanical Alloying Parameters on Crystallite Size of Ti-AI Powders," *Nano-Structured Materials*, vol. 12, pp. 171-174, 1999.

94. *D. Gu, Z. Wang, Y. Shen, Q. Li, and Y. Li, "*In-situ TiC Particle Reinforced Ti–Al Matrix Composites: Powder Preparation by Mechanical Alloying and Selective Laser Melting Behavior," *Applied Surface Science*, vol. 255, pp. 9230-9240, 2009.

95. C. L. Chen, W. Lu, L. Hea, and H. Q. Ye, "Orientation relationships between TiB (B27), B2, and Ti_3Al Phases," *Journal of Materials Research*, vol. 24 (5), 2009.

96. T. Dobbins, M. Abrecht, Y. Uprety, and K. Moore, "An X-ray Photoemission Electron Microscopy Study of the Formation of Ti–Al Phases in 4 mol% $TiCl_3$

Catalyzed $NaAlH_4$ during High Energy Ball Milling,*" Nanotechnology*, vol. 20, pp. 1-9, 2009.

97. J. A. Hooker, and P. J. Doorbar, "Metal Matrix Composites for Aeroengines," *Materials Science and Technology*, vol. 16, pp. 725-731, 2000.

98. S. L. Kampe, P. Sadler, L. Christodoulou, and D. E. Larsen, "Room-Temperature Strength and Deformation of TiB_2-Reinforced Near-gamma Titanium Aluminides," *Metallurgical and Materials Transactions A,* vol. 25A, p. 2181, 1994.

99. T. S. Srivatsan, S. Givens, M. Al-Hajri, M. Petraroli, R. Radhakrishnan, and T. Sudarshan, "The Quasi Static Fracture Behavior of a Bulk Al-Cr-Fe Alloy made by Consolidating Micron- and Nano-sized Powders," *Journal of Metastable and Nanocrystalline Materials*, vol. 23, pp. 255-258, 2005.

100. K. Kothari, R. Radhakrishnan, N. M. Wereley, and T. S. Sudarshan, "Microstructure and Mechanical Properties of Consolidated Gamma Titanium Aluminides," *Powder Metallurgy*, vol. 50 (1), pp. 21-27, 2007.

101. R. K. Bird, , T. A. Wallace, and S. N. Sankaran, "Development of Protective Coatings for High-Temperature Metallic Materials," *Journal of Spacecrafts and Rockets*, vol. 41 (2), pp. 213-220, 2004.

102. M. Yamaguchi, H. Inui, K. Kishida, M. Matsumuro, and Y. Shirai, "Gamma Titanium Alloys," *in Proceedings of Material Research Society Symposium*, vol. 364, pp. 3-15, 1995.

103. Y-W. Kim, and D. Dimiduk, "*Progress in the Understanding of Gamma Titanium Aluminides,"* JOM, vol. 43, pp. 40-47, 1991.

104. R. Le Holm, H. Clemens, and H. Kestler, *Gamma Titanium Aluminides*. [ed.] Y-W. Kim, pp. 25-33, TMS, PA, 1991.

105. P. A. Bartolotta, and D. L. Krause, *Gamma Titanium Aluminides*. [ed.] Y-W. Kim, pp. 3-10, TMS, PA, 1999.

106. Y-W. Kim, "Microstructural Evolution and Mechanical Properties of a Forged Gamma Titanium Alloy," *Acta Metallurgica et Materialia*, vol. 40 (6), pp. 1121-1133, 1991.

107. Y-W. Kim, and D.M. Dimiduk, *US Patent 5,226,985.* July 13, 1993.

108. J. Rivard, "Development of a Finite Volume Model for the High-Density Infrared Processing of Gamma-TiAl Thin-Gage Sheet," *PhD Thesis*, University of Cincinnati, Cincinnati, OH, 2005.

109. ASTM, "Annual Book of ASTM Standards," C 1161, *American Society for Testing and Materials*, West Conshohocken, PA, 1997.

110. R. C. Hibbeler, *Mechanics of Materials*. 3rd edn, p. 292, Prentice Hall, Upper Saddle River, NJ, 1997.

111. CoorsTek, Golden, CO., Alumina AD-998. http://www.coorstek.com/materials/ceramics/alumina/ad998.asp

112. Y. Q. Sun, *Gamma Titanium Aluminides*. [ed.] Y-W. Kim, pp. 105-110, TMS, PA, 1999.

113. R. E. Schafrik, "Dynamic Elastic Moduli of Titanium Aluminides," *Metallurgical Transactions A,* vol. 8A, 1003-1006, 1977.

114. H. A. Lipsitt, "The Deformation and Fracture of TiAl at Elevated Temperatures," *Metallurgical Transactions A*, vol. 6A, 1991-1996, 1975.

115. T. Tetsui, *Gamma Titanium Aluminides*. [ed.] Y-W. Kim, pp. 15-24, TMS, PA, 1999.

116. L. Langston, *Mechanical Engineering Magazine*. vol. 128, pp. 31-33, 2006.

117. 149. F. Appel, H. Clemens, and M. Oehring, *Proceedings of Material Research Society Symposium*, vol. 646, 2001.

118. H. Clemens, W. Glatz, N. Eberhardt, H.-P. Martinz, and W. Knabl, *Proceedings of Material Research Society Symposium*, vol. 460, 29-41, 1997.

119. J. Moll, C. Yolton, and B. McTiernan, *The International Journal of Powder Metallurgy*, vol. 26, 149-155, 1990.

120. N.M. Wereley, T.F. Zahrah, and F.H. Charron, *Journal of Materials Engineering and Performance*, vol. 2, pp. 671-682, 1993.

121. T. S. Srivatsan, G. Guruprasad, D. Black, R. Radhakrishnan and T. S. Sudarshan, *Powder Technology*, vol. 159, pp. 161-167, 2005.

122. Z. Sun, and H. Hashimoto, *Intermetallics*, vol. 11, pp. 823-834, 2003.

123. T. S. Srivatsan, W. O. Soboyejo, and M. Strangwood, *Engineering Fracture Mechanics*, vol. 52, pp. 107-120, 1995.

124. L. Adams, S. Kampe, and L. Christodoulou: *The International Journal of Powder Metallurgy*, vol. 26, pp. 105-114, 1990.

125. U. Prasad and M. C. Chaturvedi: *Materials Science and Technology*, vol. 20, pp. 87-92, 2004.

126. G. Wegmann, R. Gerling, F-P. Schimansky, H. Clemens, and A. Bartels, *Intermetallics*, vol. 10, pp. 511-517, 2002.

127. Q. Shengguan, L. Xiaoqiang, L. Yuanyuan, H. Lianxi, and W. Erde, "Manufacturing a TiAl Alloy by High-energy Ball Milling and Subsequent Reactive Sintering," *Rare Metals*, vol. 25, pp. 21-26, 2006.

128. A. Vyas, K. P. Rao, and Y. V. Prasad, "Mechanical Alloying Characteristics and Thermal Stability of Ti–Al–Si and Ti–Al–Si–C Powders," *Journal of Alloys and Compounds*, vol. 475, pp. 252–260, 2009.

129. D. Gu, Z. Wang, Y. Shen, Q. Li, and Y. Li, "In-situ TiC Particle Reinforced Ti–Al Matrix Composites: Powder Preparation by Mechanical Alloying and Selective Laser Melting Behavior*," Applied Surface Science*, vol. 255, pp. 9230-9240, 2009.

130. Y. L. Chen, Y. Ming, Y. M. Sun, B. C. Mei, and J. Q. Zhu, "The Phase Transformation and Microstructure of TiAl/Ti_2AlC Composites caused by Hot Pressing," *Ceramics International*, vol. 35, pp. 1807-1812, 2009.

131. R. Simpkins, M. Rourke, T. Bieler, and P. A. McQuay, *"*The Effects of HIP Pore Closure and Age Hardening on Primary Creep and Tensile Property Variations in a TiAl XD^{TM} Alloy with 0.1 wt.% Carbon*," Materials Science and Engineering*, vol. 463A, pp. 208–215, 2007.

132. S. L. Kampe, G. Swope, and L. Christodoulou, "Intermetallic Matrix Composites*," Material Research Society Symposia Proceedings*, Pittsburgh, vol. 194, p. 97, 1990.

133. S. S. Sahay, K. S. Ravichandran, R. Atri, B. Chen, and J. Rubin, "Evolution of Microstructure and Phases in in-situ Processed Ti-TiB Composites Containing High Volume Fractions of TiB Whiskers," *Journal of Materials Research*, vol. 14 (11), pp. 4214-4221, November 1999.

134. T. Saito, "The Automotive Application of Discontinuously Reinforced TiB-Ti Composites,*" JOM*, pp. 33-36, May 2004.

135. K. S. Ravichandran, K. B. Panda, and S. Sahay, "TiBw- Reinforced Ti Composites: Processing, Properties, Application Prospects, and Research Needs," *JOM*, pp. 42-48, May 2004.

136. N. Chawla, and K. K. Chawla, *Metal Matrix Composites*. Springer, New York, NY, 2006.

137. W. Jiang, and K. Yatsui, "Pulsed Wire Discharge for Nanosize Powder Synthesis," *IEEE Transactions on Plasma Science,* vol. 25 (5), October 1998.

138. J. Park, Y. Lee, Y. Koh, and H. Kim, "Effect of Hot-Pressing Temperature on Densification and Mechanical Properties of Titanium Diboride with Silicon Nitride as a Sintering Aid," *Journal of American Ceramic Society*, vol. 83 (3), pp. 1542-1544, 2000.

139. C. Mroz, "Titanium Diboride," *American Ceramic Society Bulletin,* vol. 74 (6), pp. 158-159, 1995.

140. H. R. Baumgartner, and R. A. Steiger, "Sintering and Properties of Titanium Diboride Made from Powder Synthesized in a Plasma-Arc Heater," *Journal of American Ceramic Society*, vol. 67 (3), pp. 207-212, 1984.

141. G. Dieter, *Mechanical Metallurgy*. McGraw Hill, New York, NY, 1976.

142. J. Park, Y. Koh, H. Kim, and C. S. Hwang, "Densification and Mechanical Properties of Titanium Diboride with Silicon Nitride as a Sintering Aid," *Journal of American Ceramic Society*, vol. 82 (11), pp. 3037-3042, 1999.

143. R. G. Munro, "Mechanical Properties of Titanium Diboride," *Journal of Research of the National Institute of Standards and Technology*, vol. 105 (5), pp. 709-720, 2000.

144. S. Baik, and P. Becher, "Effect of Oxygen Contamination on Densification of TiB_2," *Journal of American Ceramic Society*, vol. 70 (8), pp. 527-530, 1987.

145. V. Milman, and M. C. Wareen, "Elastic Properties of TiB_2 and MgB_2," *Journal of Physics-Condensed Matter,* vol. 13 (24), No. 24, pp. 5585-5595, 2001.

146. N. Dowling, *Mechanical Behavior of Materials*. Prentice Hall, Upper Saddle River, New Jersey, 1998.